CALIFORNIA INSTITUTE OF TECHNOLOGY

A BALLOON MEASUREMENT OF

THE ISOTOPIC COMPOSITION

OF GALACTIC COSMIC RAY

BORON, CARBON, AND NITROGEN

Thesis by

James Frederick Zumberge

In Partial Fulfillment of the Requirements

for the Degree of

Doctor of Philosophy

California Institute of Technology

Pasadena, California

1981

(Submitted 25 February 1981)

A BALLOON MEASUREMENT OF THE ISOTOPIC COMPOSITION OF
GALACTIC COSMIC RAY BORON, CARBON, AND NITROGEN

James Frederick Zumberge

California Institute of Technology
Pasadena, California 91125

Ph.D. Thesis

Submitted 25 February 1981

SRL 81-5

Acknowledgments

I wish to thank my advisor Professor Edward Stone for his support throughout my years at Caltech. I have benefited greatly from his insights into many specific problems concerning the work described in this thesis. The opportunity to have been associated with Ed is sincerely appreciated.

I also thank Professor Rochus Vogt who, on many occasions, has provided well-timed relief from purely technical matters, by way of discussions concerning administration in academia.

I am indebted to Dr. Mark Wiedenbeck for his dedication to the task of building and calibrating the HEIST instrument, and acknowledge his important contributions to my education as a physicist.

I am grateful to Don Skelton, both for his contributions to the development and support of the project in general, and for the opportunity of working with him in teaching the undergraduate physics laboratory.

Dr. Andrew Buffington provided a needed impetus toward the final stages of the data analysis. Conversations with Andy have been both illuminating and enjoyable.

Excellent design and support engineering were provided by Bill Blodgett and Daryl Dzioba. Dr. Frank Hagen contributed extensively to the progress of the experiment during its middle stages. The efforts of undergraduates Peter Goodwin and Chris Wendt were much appreciated.

Abstract

The isotopic compositions of galactic cosmic ray boron, carbon, and nitrogen have been measured at energies near 300 MeV amu^{-1}, using a balloon-borne instrument at an atmospheric depth of ~ 5 g cm^{-2}. The calibrations of the detectors comprising the instrument are described. The saturation properties of the cesium iodide scintillators used for measurement of particle energy are studied in the context of analyzing the data for mass. The achieved rms mass resolution varies from ~ 0.3 amu at boron to ~ 0.5 amu at nitrogen, consistent with a theoretical analysis of the contributing factors. Corrected for detector interactions and the effects of the residual atmosphere, the results are $^{10}\text{B}/\text{B} = 0.33 ^{+0.17}_{-0.11}$, $^{13}\text{C}/\text{C} = 0.06 ^{+0.13}_{-0.01}$, and $^{15}\text{N}/\text{N} = 0.42 ^{+0.19}_{-0.17}$. A model of galactic propagation and solar modulation is described. Assuming a cosmic ray source composition of solar-like isotopic abundances, the model predicts abundances near earth consistent with the measurements.

Table of Contents

Chapter 1

Introduction

Within the last decade, increasing emphasis in cosmic ray astrophysics has been placed on the measurement of the isotopic composition of nuclear species with atomic number $Z \gtrsim 3$, for several reasons (e.g. Stone 1973). Because the cosmic rays are extremely young ($\sim 10^7$ yr) in comparison with the solar system and constitute the only material from outside which is directly observable, it is of interest to know whether the astrophysical conditions under which they were synthesized is similar to that of solar system material. Measurements of the cosmic ray elemental composition (e.g. Garcia-Munoz and Simpson 1979, Lezniak and Webber 1978), although experimentally more tractable, do not always bear directly on the question of source composition because of possible Z-dependent selection effects (Casse' and Goret 1978) on the acceleration of the particles subsequent to their synthesis and injection into the interstellar medium. Also, because the cosmic ray abundances observed near earth are contaminated by the products of nuclear interactions suffered in the interstellar medium en route to the solar system, and the cross sections for such interactions are mass-dependent, only by measuring the isotopic composition can one adequately deconvolve observed abundances into source abundances and at the same time understand the nature of the galactic propagation process. Finally, precise measurements of the cosmic ray age are possible if radioactive nuclides with half-lives of the order of that age (e.g. ^{10}Be, ^{26}Al) can be resolved from the more abundant neighboring isotopes.

The elements boron, carbon, and nitrogen, and the isotopes of each, have different histories regarding their mode of origin. Boron has only a transient existence in stars as it is extremely unstable at temperatures required for the synthesis of elements heavier than helium. That its abundance relative to carbon in the cosmic rays (as well as that of lithium and beryllium) is orders of magnitude above the solar system value, is evidence that cosmic rays traverse several g cm^{-2} of interstellar matter before they are observed near earth. A measurement of the quantity $^{10}B/B$ in the cosmic rays depends to first-order only on the ratios of the relevant cross sections for producing ^{10}B and ^{11}B from the spallation of heavier species, primarily carbon and oxygen.

The most abundant isotope of carbon (^{12}C), on the other hand, is copiously produced in stars via helium burning. The rarer isotope ^{13}C is produced as one of the products of the CNO bi-cycle in hydrogen burning. Its abundance, when the cycle is operating in equilibrium, is a function of the temperature of the star. The solar system value of $^{13}C/C \approx 0.011$ contrasts somewhat with radio observations of molecular clouds where $^{13}C/C$ is a factor of ~ 1.5 higher (Wannier 1980). At temperatures $> 10^8$ °K one can expect a value as high as $^{13}C/C \approx 0.2$, which, in fact, has been observed in some carbon stars. It should be noted, however, that using cosmic ray measurements of $^{13}C/C$ to infer a source abundance is difficult because a large portion of the observed ^{13}C is secondary (results from the spallation of N, O, etc.).

The production in stars of the isotope ^{14}N is also associated with the CNO bi-cycle. In fact, if the cycle reaches equilibrium, essentially all

of the seed C and O nuclei are converted into ^{14}N. The isotope ^{15}N is also produced, but its abundance is predicted to be ^{15}N/N $\approx 4 \times 10^{-5}$, approximately two orders of magnitude below what is observed in the solar system. Larger amounts of ^{15}N might be produced in explosive CNO burning (Truran 1977). Like carbon, inferring a source abundance from cosmic ray measurements of ^{15}N/N requires reasonably precise values of the cross sections to produce ^{14}N and ^{15}N from abundant heavier species (predominantly ^{16}O) so as to accurately account for the secondary component of the observed flux.

Recent cosmic ray measurements of ^{10}B/B, ^{13}C/C, and ^{15}N/N can be divided into two categories, essentially on the basis of energy. In the first category are relatively low energy (~ 100 MeV amu^{-1}) satellite measurements (e.g. Garcia-Munoz et al. 1977a, Guzig 1980, Wiedenbeck et al. 1979). Although the satellite instruments typically have reasonable-to-excellent mass resolution capabilities, the interpretation of the measurements is complicated by the fact that the relevant cross sections at the corresponding energies in interstellar space vary considerably with energy, and measurements of some of the more important ones (e.g. ^{16}O+p→ ^{15}N,^{14}N) do not exist. In the second category are balloon measurements at energies of ~ 300–400 MeV amu^{-1} (e.g. Hagen et al. 1977, Buffington et al. 1978, Webber and Kish 1979, Webber et al. 1979). Disagreements among the results of these experiments, which are apparently statistically significant, suggest instead that systematic effects in the measurements may not have been properly accounted for. An advantage of the higher energy measurements is that the cross sections vary less with energy, and that

the use of semi-empirical formulae (Silberberg and Tsao 1973a, 1973b, 1977a, 1977b), which are based in part on high energy measurements (Lindstrom et al. 1975) is likely to be more reliable.

We present in this thesis the results of new measurements, using a balloon-borne detector array of position-sensitive proportional counters and energy-sensitive cesium iodide (CsI) scintillators, of the isotopic compositions of the elements boron, carbon, and nitrogen in the cosmic rays. In Chapter 2 we describe the technique and the instrument used in making the measurements, and discuss quantitatively the calibrations of the detectors. We go on in Chapter 3 to show in detail the steps involved in calculating masses, and in doing so deduce a light-energy relationship for CsI. The resulting mass distributions are analyzed for fractional abundances using a maximum-likelihood technique. We present a detailed analysis of the factors which contribute to the mass resolution and compare the calculation with the performance of the instrument. In Chapter 4 we correct the measurements for the contamination due to the residual atmosphere above the detector. We then describe a model of galactic propagation and solar modulation which allows one to predict abundances observed at earth given a set of source abundances. Finally, we compare our results and those of other recent measurements with the predictions of the model.

Chapter 2

Instrumentation and Calibrations

2.1 The Instrument

The Caltech High Energy Isotope Spectrometer Telescope (HEIST) is a balloon-borne cosmic ray detector array designed to measure charge, mass, and energy of individual cosmic ray nuclei with nuclear charge $Z \gtrsim 4$. The instrument has been described in detail by Wiedenbeck (1978). We review here the major features.

In Figure 2.1 we depict the basic technique employed by HEIST. A cosmic ray nucleus of mass M [proton mass units (pmu); 1 pmu $=$ 1.0073 amu], atomic number Z, and total kinetic energy E traverses a detector of thickness t at an angle ϑ in which it loses an energy ΔE, and stops in a subsequent detector where it loses its remaining energy $E' = E - \Delta E$. Since the range R in a given material is a function of energy, mass, and charge we have

$$R(E' + \Delta E, M, Z) = t \sec \vartheta + R(E', M, Z) \qquad (2.1).$$

To understand how R varies with E, M, and Z, we consider the energy loss per unit pathlength (Rossi 1952, Jackson 1975, Janni 1966)

$$\frac{dE}{\rho dx} = 0.307 \, \text{MeV cm}^2 \, \text{g}^{-1} \frac{Z_m Z^2}{A_m \beta^2} [\ln(\frac{2 m_e c^2 \gamma^2 \beta^2}{I}) - \beta^2 - C - \frac{\Delta}{2}] \qquad (2.2)$$

where

β = particle velocity (in units of the speed of light c),
$\gamma = (1 - \beta^2)^{-0.5}$,
Z_m, A_m = mean atomic number, weight of detector material,
ρ = density of material (g cm^{-3}),
$m_e c^2$ = electron rest mass, 0.511 MeV,
I = mean ionization potential of material,
C = correction for atomic shell structure,
$\frac{\Delta}{2}$ = correction for density effect.

Figure 2.1

The $\Delta E-E'$ technique of isotope identification. As the particle enters the ΔE-detector it has a total kinetic energy E. As it enters the E'-detector it has an energy E'. Since the pathlength in the ΔE-detector is $t\sec\vartheta$, we have $R(E'+\Delta E,M,Z) = R(E',M,Z) + t\sec\vartheta$ from which we can extract M.

(M,Z)

θ

trajectory of heavy ion

energy $E = E' + \Delta E$

ΔE dectector

t sec θ

t

energy $E' = E - \Delta E$

E' detector

end of range of heavy ion
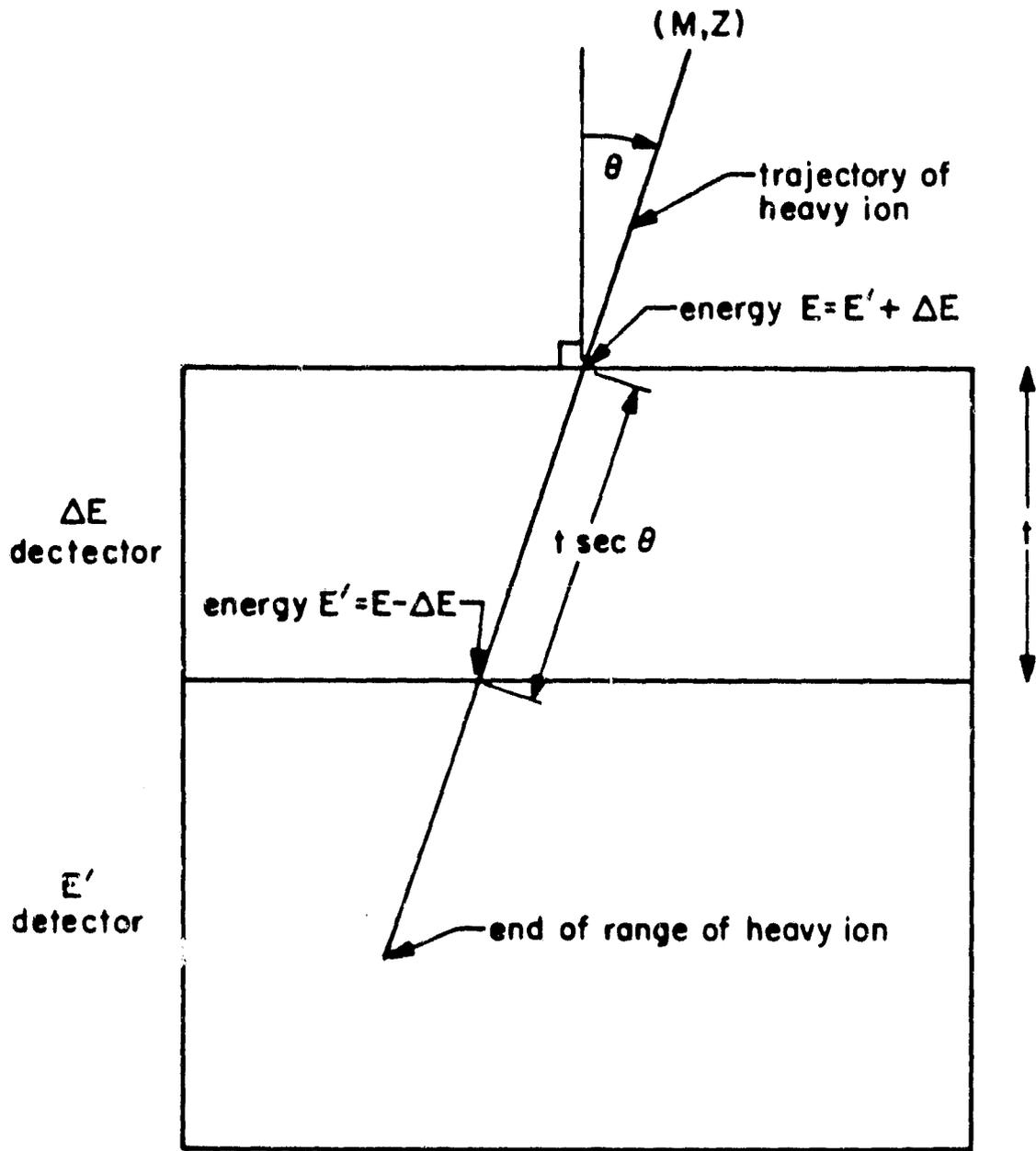
Since velocity β depends only on the kinetic energy per unit mass E/M, we thus have for a given material $\frac{dE}{dx} = Z^2 S(\frac{E}{M})$, where $S(\varepsilon)$ is the specific ionization of a proton of kinetic energy ε. The range is

$$R(E,M,Z) = \int_0^E \frac{dE}{dE/dx} = M \int_0^{E/M} d\varepsilon \frac{1}{Z^2 S(\varepsilon)} = \frac{M}{Z^2} R_p(\frac{E}{M}) \tag{2.3}$$

where $R_p(\varepsilon) = \int_0^\varepsilon d\varepsilon \frac{1}{S(\varepsilon)}$ is the range of a proton of kinetic energy ε. Although the $\frac{M}{Z^2}$ scaling of range begins to break down for $\beta \lesssim \frac{2Z}{137}$ corresponding to $\frac{E}{M} \lesssim 4$ MeV amu^{-1} for Z=6, it is valid for energies and charges of interest in this experiment.

For illustrative purposes we use a power law approximation $R_p(\varepsilon) = k\varepsilon^a$ (accurate to $\pm 15\%$ for $1 < \varepsilon < 1000$ MeV; depending on the material, a is typically 1.7) so that $R(E,M,Z) = \frac{kM}{Z^2}(\frac{E}{M})^a$. With this approximation, Equation 2.1 can be solved for M explicitly:

$$M = [\frac{k(E^a - E'^a)}{Z^2 t \sec\vartheta}]^{\frac{1}{a-1}} \tag{2.4}$$

Thus knowledge of Z and t together with measurements of ΔE, $E' = E - \Delta E$, and ϑ suffice to determine M. We defer a more detailed discussion of the technique to Chapter 3.

Our instrument consists of two major components (Figure 2.2). First is a hodoscope consisting of eight multiwire proportional counters (MWPC's) X1–X4 and Y1–Y4 for measurement of particle trajectory. Anode wire spacing is 4 mm, cathode wire spacing is 2 mm. A mixture of 70% Ar and 30% CO_2 at a pressure of 1 atmosphere is used for counter gas. Readout of individual counters is by means of an electromagnetic delay line (~ 14 nsec mm^{-1} delay) to which the cathode wires are

Figure 2.2

Elements of the HEIST detector (from Wiedenbeck 1978).

a) Cross sectional view of the instrument. The cross section is taken along a diagonal of the proportional counter hodoscope. The light pipes and attached photomultipliers lie off of this plane and are shown projected onto it.

b) View from above.

c) View taken through section A—A indicated in b). Note that this view is at 45° to that shown in a). Each of the detectors D0 through D7 has discriminators corresponding to whether the output from PMT dynode 3 (H for high level) or dynode 7 (L for low level) is used. D0 and D1 each have in addition a "medium level" discriminator (M). The stopping equation has been designed to eliminate $Z \leq 2$ particles when possible but to accept nuclei with $Z \geq 4$.

a

MULTI-WIRE
PROPORTIONAL
COUNTER
HODOSCOPE

CsI (Tℓ) CRYSTAL
SCINTILLATOR STACK

NE 102 PLASTIC
ANTICOINCIDENCE
SCINTILLATORS

PM TUBES
(RCA 4439)

ADIABATIC LUCITE
LIGHT PIPES

PM TUBES
(EMI 9530R)

10cm

b

HODOSCOPE SECTOR
BOUNDARIES

BOUNDARY OF
HODOSCOPE ACTIVE
AREA

CsI(Tℓ)
SCINTILLATOR
STACK

A
A

PLASTIC
ANTICOINCIDENCE
SCINTILLATORS

10 cm

C

X1
Y1
X2
Y2

X3
Y3
X4
Y4

D0 (3mm)
D1 (3mm)
D2 (3mm)
D3 (4mm)
D4 (6mm)
D5 (8mm)
D6 (12mm)
D7 (17mm)
D8 (3mm)

ANTICOINCIDENCE SCINTILLATOR

10cm

Coincidence equations:

Stopping = $(X1+X2) \cdot (Y1+Y2) \cdot (X3+X4) \cdot (Y3+Y4) \cdot$
$\left[(D0L \cdot D1L + D0L \cdot D2L + D1L \cdot D2L) \cdot (D4L+D5L) + D0M \cdot D1M \right] \cdot \overline{D8M} \cdot \overline{A}$

Penetrating = $(X1+X2) \cdot (Y1+Y2) \cdot (X3+X4) \cdot (Y3+Y4) \cdot$
$(D0L \cdot D1L + D0L \cdot D2L + D1L \cdot D2L) \cdot (D4L+D5L) \cdot D8M$

where L = low level, M = medium level

capacitively coupled. Each coordinate is divided into three sectors of 178 mm width. Comparisons of the signal amplitudes among sectors determine the gross position of a particle, while timing of delay line pulses determines the position of a particle within a sector (fast electronics capable of 1 nsec resolution are used for delay line timing). The active area of each MWPC is $\sim 50\,cm \times 50\,cm$.

For measurement of particle energy we use a stack of eight cylindrical CsI(Tl) scintillation crystals, D0 through D7, each nominally 11 inches (27.9 cm) in diameter, ranging in thickness from 3 mm to 17 mm. Each crystal is sandwiched between two sheets of $3.3\,mg\,cm^{-2}$ millipore to minimize absorption of scintillation light at the crystal faces. Scintillators are optically separated from each other by $6.4\,\mu m$ aluminized Mylar. One–half of the circumferential edge of each of the crystals is optically coupled to a Lucite light pipe, by which scintillation light from the crystal is transported to its own 5" photomultiplier tube (PMT). Associated with each PMT are analog and digital circuits for pulse height analysis of PMT output. To maximize the dynamic range the outputs from both the third ("high level" or "low gain") and seventh ("low level" or "high gain") dynodes of each PMT are amplified and shaped independently, and discriminators direct one of these signals to an analog–to–digital converter for readout. D8, a ninth CsI crystal used to tag particles which penetrate D7, has only discriminators (is not pulse height analyzed). Finally, two NE 102 plastic scintillators are mounted below the CsI stack and used in an anticoincidence mode to tag wide angle penetrating events which enter and leave the CsI before encountering D8.

The instrument is designed to operate in either of two modes called "stopping" and "penetrating". The detailed coincidence equations are given in Figure 2.2c. Stopping events are simply those for which the particle stops somewhere between the top of D1 and the bottom of D7, and are suitable for our $\Delta E-E'$ mass analysis technique described above. We confine ourselves in this thesis to mass analysis of particles which stop in D7 (Chapter 3). Penetrating events are those for which the particle penetrates beyond the bottom of D7. Because we cannot analyze these events for mass, they are accumulated in flight with a lower priority than stopping events and are useful mainly for in-flight calibrations. Both stopping and penetrating events require that the particle trigger a sufficient number of MWPC's to adequately deduce particle trajectory.

The payload was launched from Yorkton, Saskatchewan, Canada at 0303 CST on 30 August 1978. The magnetic rigidity cutoff at this location is $\sim 700\,MV/c$, corresponding to $\varepsilon \sim 65\,MeV\,pmu^{-1}$. Prior to flight, the electronics associated with MWPC X2 failed and were turned off. Approximately twenty hours of data were taken at an atmospheric depth of $4-6\,g\,cm^{-2}$. The flight was terminated at 0710 CST on 31 August and the payload recovered approximately 400 km west of Yorkton.

2.2 Calibrations

Both pre-flight and in-flight calibrations were carried out for the HEIST instrument. Most prominent in the pre-flight category was a run at the Lawrence Berkeley Laboratory heavy ion facility (Bevalac), from

which data were collected for the construction of two-dimensional light collection efficiency maps for D0 through D7. Also included in the pre-flight category were detailed electronic calibrations of the pulse height analyzers (PHA's) used to convert PMT signals to digital form. In-flight calibrations have included cross-calibrations of the MWPC's, residual light collection maps, PMT temperature-dependent nonlinearity corrections, and inter-detector normalizations.

2.2.1 MWPC Calibrations

The difference in arrival times of the delay line pulses, $\delta\tau$, is linearly related to the position x: $x = \dfrac{\delta\tau}{\alpha} + \beta$. The parameters α and β vary from counter to counter and from sector to sector within a counter (pre-flight diagnostic tests indicated, for example, that α, whose nominal value is $14\,\text{nsec mm}^{-1}$, could vary by as much as 10% among the various counters). For a given MWPC our parametrization of response is

$$x(\delta\tau) = \begin{cases} \dfrac{\delta\tau - \tau_-}{\alpha_-} - r & \text{for the left sector} \\[2mm] \dfrac{\delta\tau - \tau_0}{\alpha_0} & \text{for the center sector} \\[2mm] \dfrac{\delta\tau - \tau_+}{\alpha_+} + r & \text{for the right sector,} \end{cases}$$

where $\tau_{-(+)}$ = response of MWPC corresponding to the left (right) edge of the CsI stack, given a beam of normally incident particles; r = radius of CsI stack; τ_0 = response of MWPC to particle at center of MWPC; and $\alpha_-, \alpha_0, \alpha_+$ = delay of left, center, right sector, respectively. The quantities τ_- and τ_+ were determined for each MWPC from a Bevalac run (§2.2.3) of normally incident ^{40}Ar nuclei. The first-order estimate of the other parameters is $\alpha_- = \alpha_0 = \alpha_+ = 14\,\text{nsec mm}^{-1}$ and $\tau_0 = 0$, for all

MWPC's.

We have used this first-order estimate of MWPC response to determine, for each event, a particle trajectory $x = m_x z + b_x$, $y = m_y z + b_y$, by minimizing the quantities $\chi_x^2 = \sum_{2 \neq i=1}^{4} (x_i - m_x z_{xi} - b_x)^2$, and $\chi_y^2 = \sum_{i=1}^{4} (y_i - m_y z_{yi} - b_y)^2$, where $z_{x(y)i} =$ z-coordinate of MWPC X(Y)i. We show in Figure 2.3a the distribution of the minimized χ_y for the flight data. The long tail for $\chi_y > 7$ mm is due to a contamination of the trajectory data by knock-on electrons, produced most likely in the $0.69 \mathrm{g\,cm^{-2}}$ aluminum shell which encloses the experiment, which confuse a delay line with more than one pulse. This background is discussed in detail in Appendix A. The peak at $\chi_y \approx 2.7$ mm indicates that the resolution for an individual uncontaminated y-measurement is $\sigma_y \approx 2.7$ mm (Bevington 1969). By adjusting the αs and $\tau_{-,0,+}$'s individually for each sector of each MWPC within the constraints imposed by counter fabrication (typical adjustments were a few percent, all were < 5%) we have improved this distribution to that shown in Figure 2.3b, so that $\sigma_y \approx 1$ mm. Shown in Figure 2.3c is the distribution of the minimized χ_x, after adjustment of the parameters, for the x-trajectory measurement (the shape of the χ_x distribution differs from that of χ_y because we use only three measurements X1,3,4 in determining the x-trajectory). The quantities χ_x and χ_y will be used later to reject events for which our determination of trajectory is inadequate for mass resolution.

Figure 2.3

MWPC resolution.

a) χ_y distribution, first—order parametrization of MWPC response.

b) χ_y distribution, optimized parametrization.

c) χ_x distribution, optimized parametrization.
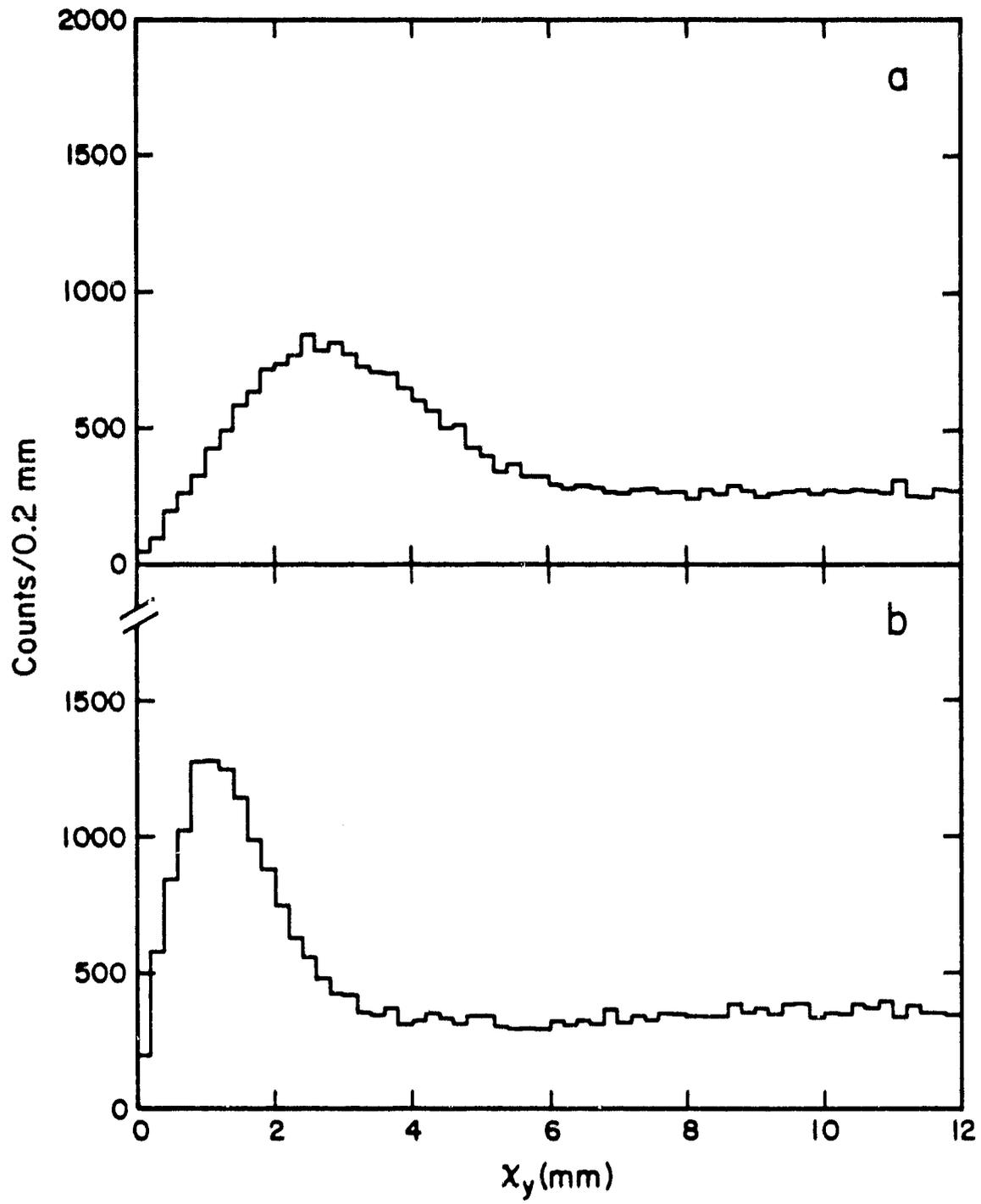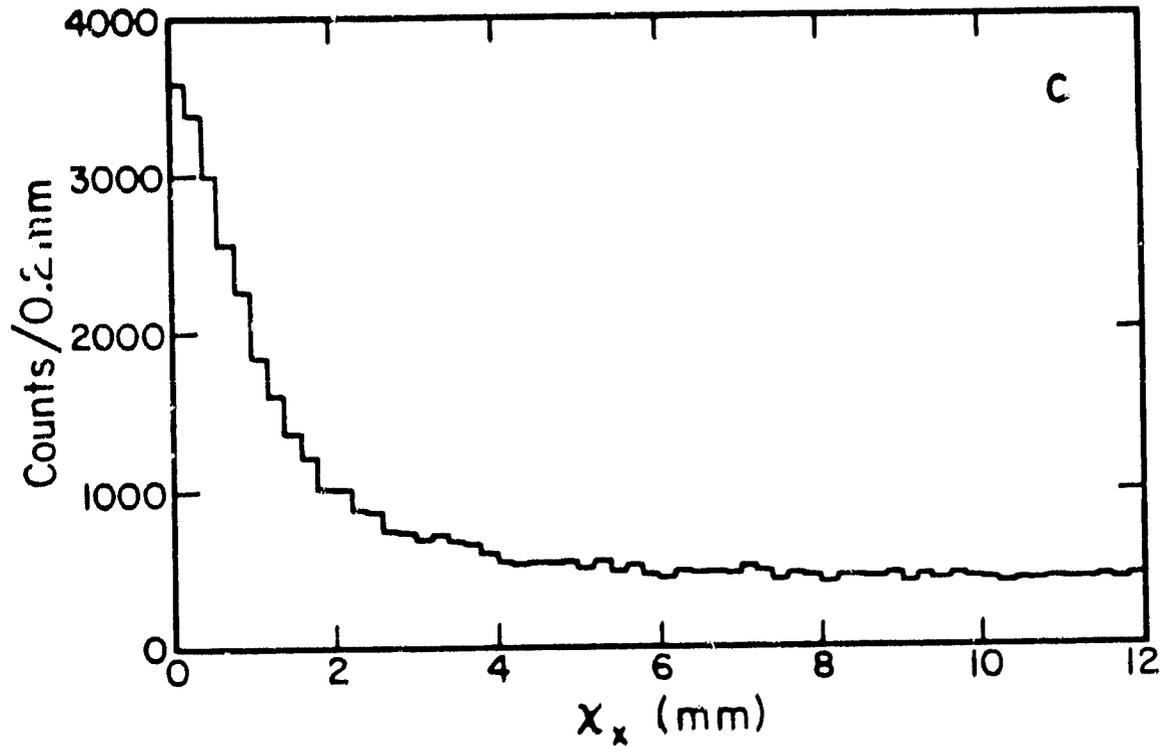
2.2.2 PHA Calibrations

Prior to flight, electronic calibrations were made for the pulse height analyzers which are designed to logarithmically compress the PMT output. Diagnostic tests indicated a non–negligible temperature coefficient to PHA response, so calibrations were made at several temperatures and each PHA was assigned its own thermistor for recording of temperature in flight. Figure 2.4 shows typical variation in PHA output with respect to temperature given a fixed input voltage. A number of runs at different input voltages and temperatures provides us with a two–dimensional table of PHA response. For each event we have used linear interpolation in temperature and raw pulse height to convert PHA output for D0–D7 to a form which is proportional to the log of the PHA input, independent of temperature.

2.2.3 Spatial Variations in Scintillator Response

HEIST was taken to the Bevalac in February 1977. A defocused monoenergetic $900\,MeVamu^{-1}$ penetrating ^{40}Ar beam illuminated the instrument, allowing the construction of two–dimensional light collection efficiency maps for D0 through D7. Based on the trajectory information supplied by the MWPC hodoscope, events were assigned to $5\,mm \times 5\,mm$ bins in x and y position at each scintillator. For each bin the mean of the pulse height distribution was calculated, and compared with the average pulse height over the entire crystal. The maps were then smoothed by performing a moving average over $25\,mm \times 25\,mm$ areas to decrease the statistical error in the mean to 0.1–0.2%. We show in Figure 2.5 the percentage deviation from average signal size as a

Figure 2.4

Output of the D6 PHA vs. temperature for a fixed input signal (0.251333 volts). A 1 channel change in "Pulse Height" corresponds approximately to a 0.128% change in input voltage. The figure indicates a temperature-dependent response of $\sim -0.15\%/^\circ$C.
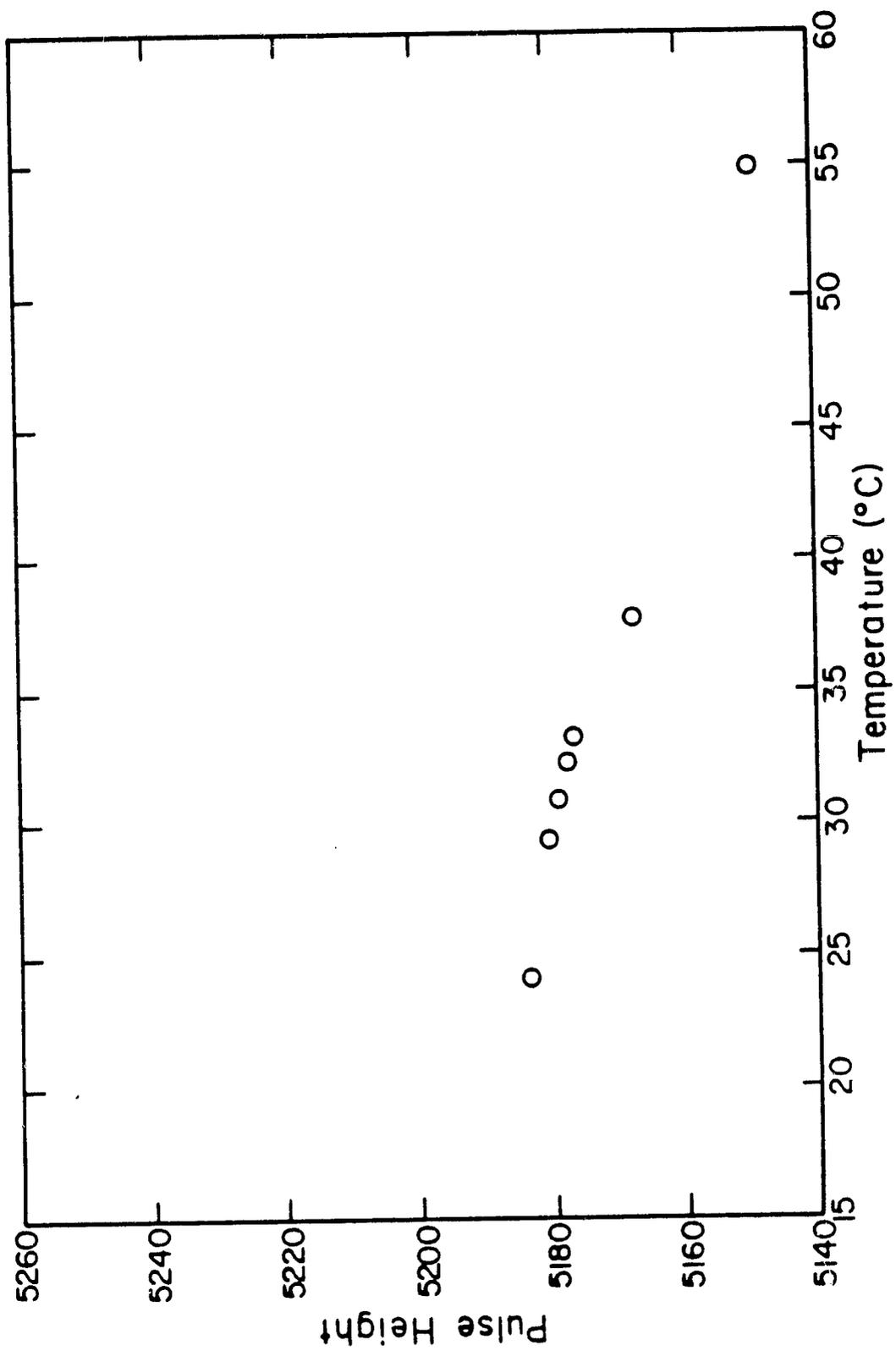
function of position on the crystal face for D6. As expected, light collection is most efficient near the edge of the crystal to which the light pipe is attached. If $r(x,y)$ is the response at position (x,y), then the fractional rms variation in response over the face of the crystal is

$[\frac{1}{A} \int dx\, dy\, [\frac{r(x,y)}{r_0} - 1]^2\ ]^{\frac{1}{2}}$ where $r_0 = \frac{1}{A} \int dx\, dy\, r(x,y)$ and $A =$ crystal area.

The mean fractional gradient is $\frac{1}{A} \int dx\, dy\, \frac{1}{r(x,y)} [(\frac{\partial r}{\partial x})^2 + (\frac{\partial r}{\partial y})^2]^{\frac{1}{2}}$. Both of these quantities are tabulated for D0–D7 in Table 2.1. Typical gradients are 0.1–0.2% mm^{-1} for the thick scintillators and 0.2–0.3% mm^{-1} for the thin ones.

A portion of this spatial variation in detector response is due to thickness variations over the face of the crystal and not to light collection variations. This rms variation (Table 2.1), however, is small compared to light collection variation, although it could in principle be deduced independently. While it is true that thickness variations ought to be handled differently from variations in light collection efficiency (the former should not be treated as a correction on measured scintillation light, but rather as an adjustment in thickness t in, e.g., Equation 2.4), the error we make in lumping the two together is small (see § 3.5).

Because the Bevalac calibration took place 1.5 years prior to the Yorkton flight, it might be expected that the response map measured there would be inadequate for application to flight data. Unlike the Bevalac calibration, however, there is of course no subset of flight data which consists of a particular nuclear species at a fixed energy and incident angle. The first step in using flight data for calibration

Figure 2.5

Bevalac light collection efficiency map for D6. Numbers represent the percentage deviation from the nominal response of the detector to relativistic ^{40}Ar nuclei. Units are 2% (i.e. a "0" means between 0 and 2% deviation, a "1" between 2 and 4%, etc.). The light pipe is attached to the crystal in the −x, +y quadrant.
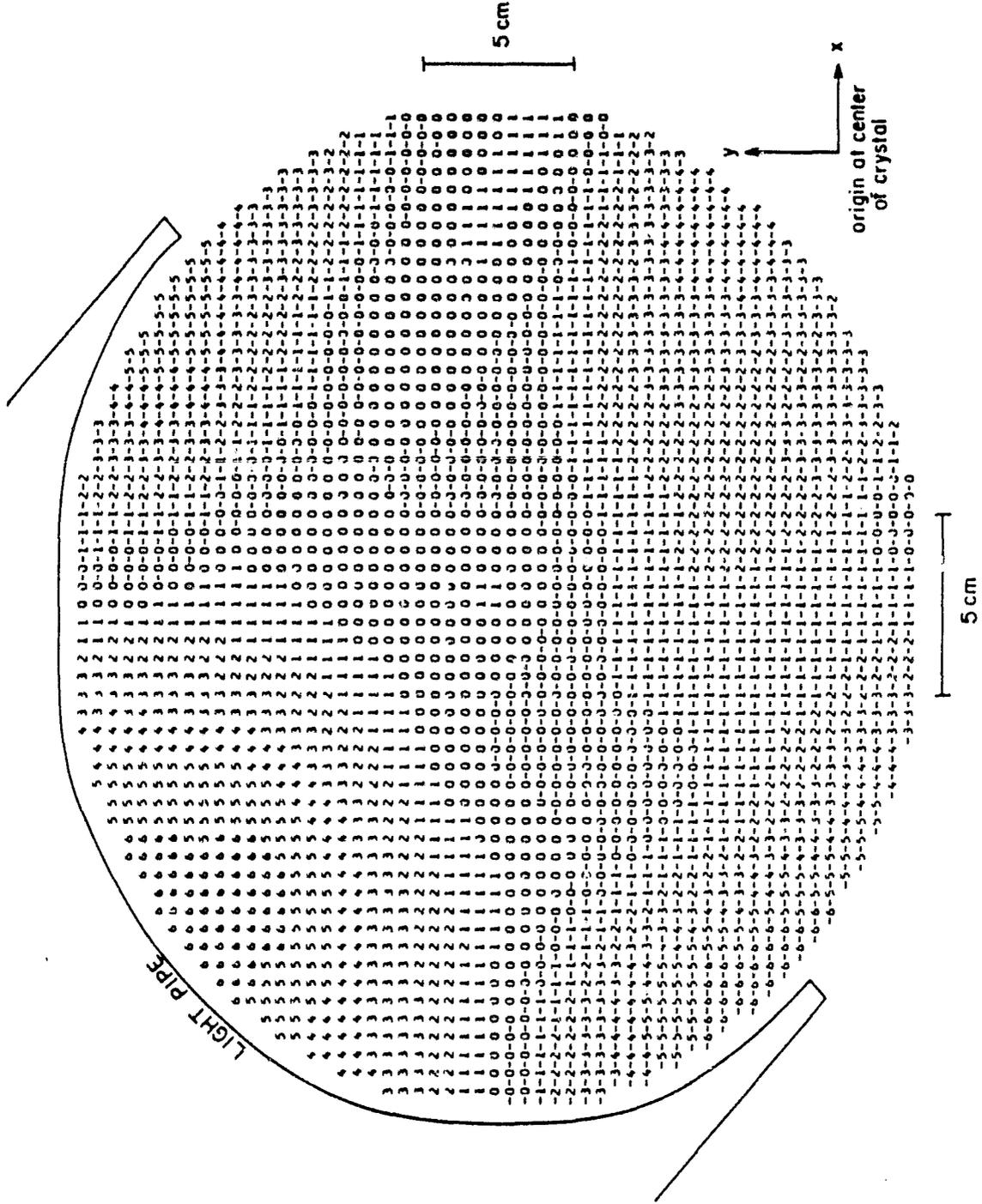
Table 2.1 Scintillator Spatial Nonuniformity Characteristics

		Bevalac(1)		residual(2)		Total(3)	
Detector	Thickness	RMS Variation	Mean Gradient	RMS Variation	Mean Gradient	RMS Variation	Mean Gradient
D0	3 mm ± 2.4%	14.1%	0.31%/mm	7.4%	0.14%/mm	19.3%	0.36%/mm
D1	3 mm ± 2.4%	10.0	0.23	8.8	0.14	16.3	0.27
D2	3 mm ± 2.4%	7.0	0.20	10.0	0.19	14.9	0.30
D3	4 mm ± 1.8%	11.8	0.25	8.3	0.12	17.8	0.32
D4	6 mm ± 1.2%	8.2	0.20	5.8	0.09	9.6	0.22
D5	8 mm ± 0.9%	5.1	0.13	1.9	0.04	4.9	0.14
D6	12 mm ± 0.8%	5.7	0.14	1.9	0.05	5.4	0.15
D7	17 mm ± 0.4%	4.2	0.10			4.2	0.10

Notes:
(1) From a calibration run at the LBL heavy ion accelerator.
(2) From flight data.
(3) Superposition of Bevalac and residual maps.

purposes isolates a subset of that data consisting of a single charge (by methods described in Chapter 3). The data set consists of either particles which stop in a particular detector Dm, or penetrate all detectors D0–D7. In the former case, signal D_m (denotes the PHA–calibrated output of detector Dm, corrected for spatial variation in response as measured at the Bevalac, equal to the log of the light output L_m) is a good measure of particle energy. In the latter case we have no measurement of the particle's total energy, only its energy loss in D0,D1,...D7. One can take Equation 2.1 with the scaling in Equation 2.3 to define the energy loss ΔE for a given M and Z in a particular detector as a function of the incident energy E. Differentiation gives

$$\frac{\partial \Delta E}{\partial E})_{M,Z,\sec\vartheta} = 1 - \frac{S(\frac{E'}{M})}{S(\frac{E}{M})}$$ [recall that $S(\varepsilon)$ is the specific ionization of a

proton of energy ε]. Thus ΔE is a measure of particle energy only to the extent that $S(E'/M)$ is different from $S(E/M)$. For penetrating events detector D7 best satisfies this criterion since, as the thickest detector, it gives the largest $\Delta E = E-E'$. Hence for penetrating calibration data sets we take signal D_7 to be the best available measurement of particle energy.

Given some calibration data set, then, we can remove variations in signal D_n correlated with energy and angle by fitting a function $f_n(\sec\vartheta, D_m)$ which predicts, for a given $\sec\vartheta$ and D_m, the "nominal response" of detector Dn. We have used the form

$$f_n(\sec\vartheta, D_m) = \sum_{i=1}^{4}\sum_{j=1}^{4} a_{ij}\ (\sec\vartheta)^{i-1} D_m^{j-1}\ ;$$

the coefficients a_{ij} are determined by minimizing the quantity

$\sum_{events} [D_n - f_n(\sec \vartheta, D_m)]^2$ (the sum is over all events of the selected data set). Once we have determined the functions f_n, we can scatter plot $D_n - f_n(\sec \vartheta, D_m)$ versus quantities such as position and temperature to look for correlations.

As a specific example we show in Figure 2.6 a scatter plot of the deviation of signal D_1 from nominal response, $D_1 - f_1(\sec \vartheta, D_4)$, for α-particles which stop in detector D4, versus the x' coordinate at detector D1. (The $x'-y'$ axes are rotated $45°$ from the $x-y$ axes; they correspond to the light collection symmetry axes of the scintillators. See Figure 2.2b.) The data have been corrected for light collection variation as measured at the Bevalac, yet a considerable spatial variation remains. This residual light collection variation is due most likely to a degradation in the surface polish of the scintillators over the ~ 1.5 years between the Bevalac calibration and flight.

To remove such an effect for a given detector Dn, we fit another function

$$\delta_n(x',y') = \sum_{i=1}^{4} \sum_{j=1}^{4} b_{ij} \ (x')^{i-1}(y')^{j-1}$$

whose coefficients b_{ij} are determined by minimizing the quantity $\sum_{events} [D_n - f_n(\sec \vartheta, D_m) - \delta_n(x',y')]^2$, where f_n has already been determined. The quantity $e^{-\delta_n(x',y')}$ is then the multiplicative correction factor which, when applied to $L_n = e^{D_n}$ for an event at (x',y') on detector Dn, will remove the residual spatial dependence of output L_n.

We have used this technique to look for residual spatial variations in the response of detectors D0–D6. For D4–D6 we have used

Figure 2.6

Deviation from nominal response of detector D1 vs. x' for α-particles stopping in detector D4. The D4 light pipe is in the +x' direction. Since "D_1" is a logarithmic measure of the output of D1, full scale on the ordinate corresponds to a factor of $e^{0.6} \approx 1.8$.
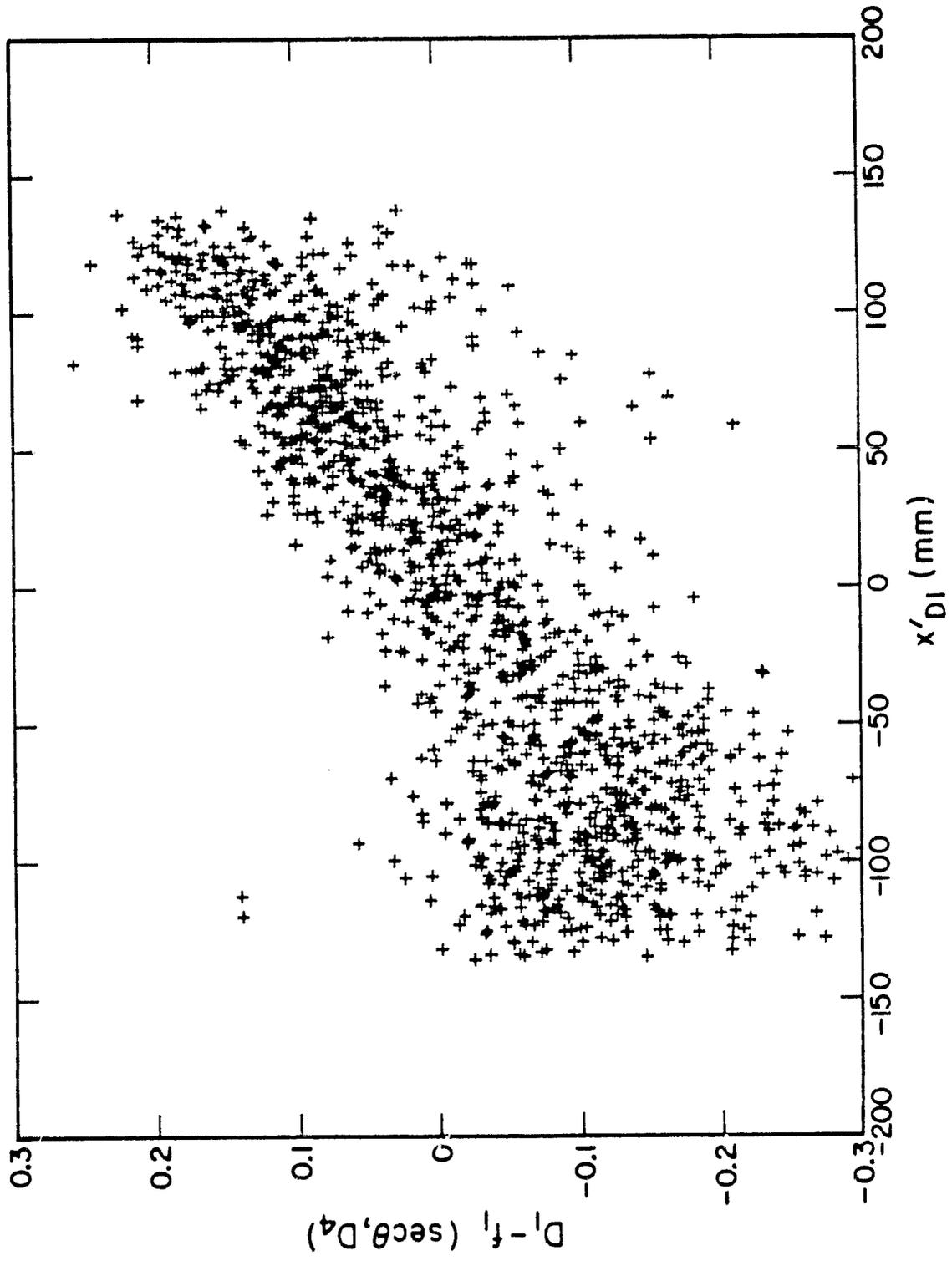
penetrating oxygen data for the calibration (n=4,5,6; m=7) under the assumption that the residual variation in D7 is negligible (the consequences of this assumption are discussed in §3.5). For DO-D3 we have used α-particles stopping in detector D4 (n=0,1,2,3; m=4), having corrected D_4 for residual variation with the oxygen data set. We list under "residual" in Table 2.1 the fractional rms variation s_n in residual response for DO-D6, where $s_n^2 = \frac{1}{A}\int dx'\,dy'\,[\frac{r'(x',y')}{r'_0} - 1]^2$ with $r'(x',y') = e^{\delta_n(x',y')}$, and $r'_0 = \frac{1}{A}\int dx'\,dy'\,r'(x',y')$. Also tabulated are the mean residual gradients $\frac{1}{A}\int dx'\,dy'\,\frac{1}{r'(x',y')}[(\frac{\partial r'}{\partial x'})^2 + (\frac{\partial r'}{\partial y'})^2]^{\frac{1}{2}}$. Finally, these same quantities corresponding to the superposition of the Bevalac and residual response maps are tabulated under the column in Table 2.1 labeled "Total". Table 2.1 thus summarizes the spatial nonuniformity characteristics of our scintillators.

The precision with which we can make the residual correction depends on the statistical accuracy in the determination of the coefficients b_{ij} for a particular δ_n. That is, the quantity $\sum[\,D_n - f_n - \delta_n\,]^2$ is not precisely zero, because other effects (for example, Landau fluctuations; see §3.5) cause scatter in signal D_n. Although the exact value varies with (x',y'), typically the correction is known to $\pm\, s_n\,(\frac{N}{2})^{-\frac{1}{2}}$, where N is the number of events used in determining δ_n. This value ranges from 0.2-0.3% for DO-D6.

2.2.4 Temperature-Dependent PMT Output

There are two effects which can cause PMT output to change with respect to temperature given a fixed amount of energy deposited in the associated scintillator. One is the temperature dependence of the scintillation efficiency of CsI which is approximately $-0.4\%/°C$ (Birks 1964). The other is the temperature-dependent gain of a PMT which is expected to be of the same order (Wiedenbeck 1978). PMT temperatures were monitored in flight and ranged from 30 to 40 °C. The CsI temperature was not measured directly, but nearby measurements indicate that its total variation in temperature was similar to that of the PMT's. Based on carbon stopping in D7 we have derived temperature coefficients for D0 through D6 (Table 2.2), typically $\sim -1\%/°C$, under the assumption that the temperature coefficient for D7 is the average of those for D0-D6 (an iterative approach is thus required). The technique was identical to that used in determining the residual spatial variations in scintillator response, with temperature replacing position as the independent variable. The variances of the fits and number of events used in the calibration have limited the precision with which we can correct PMT output for temperature variations to $\pm 0.4\%$.

2.2.5 Inter-Detector Normalization

Because we add signals from different detectors together for analysis of mass (e.g. as in Equation 2.4 where we add the separate measurements E' and ΔE to get E), it is necessary that the detectors be normalized among themselves. We show in Figure 2.7 a histogram of signal D_5, normalized to vertical incidence, for penetrating particles.

Table 2.2 PMT Temperature Coefficients and Detector Normalizations

Detector	Temperature Coefficient	Normalization ($\pm$ 0.01)
D0	-0.56 %/°C	1.53
D1	-1.23	0.91
D2	-0.76	0.75
D3	-0.65	1.03
D4	-1.05	0.93
D5	-1.18	1.16
D6	-0.94	0.87
D7	-0.91	1.28

Figure 2.7

Penetrating distribution of signal $D_5 = \ln L_5$ (the units of L are defined in the text). The cutoff at $D_5 \approx 2.7$ corresponds to the selection for this plot that the high level discriminator not fire.
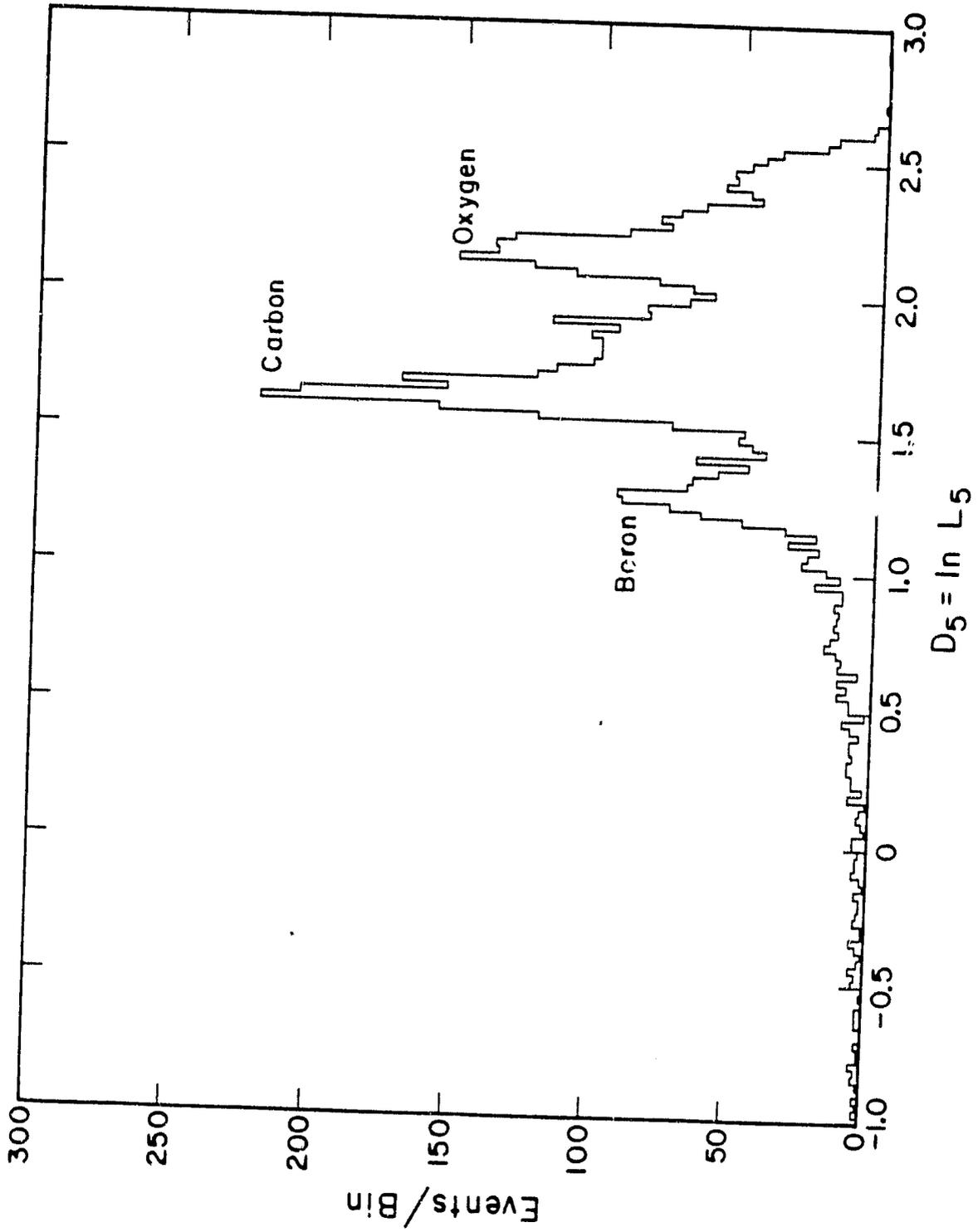
[$D_n = \ln L_n$; the units of L, which we call "normalized light units" or nlu, are such that 1 nlu corresponds to a charge signal at PMT dynode 7 of nominal magnitude 11 pC (1 pC $= 10^{-12}$ Coulomb)]. The peaks correspond to boron, carbon, and oxygen (nitrogen, about one-quarter as abundant as carbon, is not resolved). The major contribution to the width of the peaks is the variation in particle energy at the top of D0. The most likely pulse height for a given charge, however, corresponds to minimum ionizing β (the minimum dE/dx in Equation 2.2 which occurs at $\beta \approx 0.95$ or E/M $\approx$ 2 GeV amu^{-1}) and is therefore proportional to detector thickness. The unnormalized PMT output of detector Dn due to a minimum ionizing particle of a given charge which creates an amount of light per unit distance l is $q_n = g_n \varepsilon_n t_n l$, where g_n = gain of PMT n, ε_n = fraction of light created which is transported to the PMT face and converted to photoelectrons, and t_n = thickness of detector Dn. The normalization constants c_n are chosen so that $\dfrac{c_n q_n}{g_n \varepsilon_n t_n}$ is the same for all detectors; they are tabulated in Table 2.2. For those detectors for which we have three independent determinations of c_n corresponding to the boron, carbon, and oxygen peaks, the c_n's agree to better than $\pm$ 0.01. Given our method of determining the absolute light to energy relationship (§3.3), this error contributes to errors in mass only in second order, and is therefore negligibly small.

Chapter 3

Mass Analysis and Resolution

Up to this point we have been concerned primarily with the various corrections which must be made to the raw data to put it in a form suitable for analyzing masses. In this chapter we deal with a more fundamental problem, namely the relationship between the amount of energy deposited in CsI and the corresponding scintillation light, and the dependence of that relationship on particle properties such as charge, mass, velocity, and specific ionization. Having solved this problem we will be able to deduce the isotopic compositions of boron, carbon, and nitrogen as measured by our instrument at $5\,\mathrm{g\,cm^{-2}}$ atmospheric depth. Finally we discuss those factors which contribute to the mass resolution, and compare the expected mass resolution with the performance of the instrument.

3.1 Theory

We begin by considering in more detail the $\Delta E - E'$ technique on which our experiment is based. If $R(E,M,Z)$ is the range in CsI of a particle of total kinetic energy E, mass M, and nuclear charge Z, then after traversing a thickness t at angle ϑ in which the particle loses an energy ΔE, the residual range is $R(E',M,Z)$, where $E' = E - \Delta E$ (Figure 2.1). The range–energy function of a heavy ion is related to that of a proton (Equation 2.3) by $R(E,M,Z) = \frac{M}{Z^2} R_p(\frac{E}{M})$. We thus have

$$R_p(\frac{\Delta E + E'}{M}) - R_p(\frac{E'}{M}) = \frac{Z^2 t \sec \vartheta}{M} \tag{3.1}.$$

We show in Figure 3.1 this theoretical relationship between ΔE and

E' for various particles which stop in D7 of our instrument. We have taken $t = 12$ mm (the thickness of D6), and used the tabulation by Janni (1966) of the range-energy function for protons in CsI. ΔE in Equation 3.1 corresponds to the energy lost in D6, and E' corresponds to the remaining energy lost in D7. We have assumed $\vartheta = 0°$ (solid lines) and have plotted one "track" with $\vartheta = 30°$ (dashed line) to show the angular dependence. Because of the Z^2 scaling of dE/dx (Equation 2.2) we see from this figure that the separation between tracks of adjacent elements is much greater than that between isotopes of a single element. One can calculate from Equation 2.4, which is based on the power law approximation $R_p(\varepsilon) = k\varepsilon^a$, that

$$\frac{\partial \Delta E}{\partial M} \Big)_{E',Z} = \frac{a-1}{a+1} \frac{Z}{M} \frac{\partial \Delta E}{\partial Z} \Big)_{E',\frac{Z}{M}}.$$

With $a \approx 1.66$ for CsI (Wiedenbeck 1978) and $M = 2Z$ this yields

$$\frac{\partial \Delta E}{\partial M} \Big)_{E',Z} = 0.12 \frac{\partial \Delta E}{\partial Z} \Big)_{E',\frac{Z}{M}}.$$

An exact calculation shows that the separation in ΔE between ^{12}C and ^{13}C at $E' = 1$ GeV is 6.4% of the separation between ^{10}B and ^{14}N at the same E'. Thus a change in one mass unit is equivalent to a change of 0.128 charge units.

3.2 Charge Identification

We now describe the means by which we can identify in our data the charge of each particle which stops in D7. Figure 3.2a is a scatter plot of L_6 vs. L_7 for particles stopping in D7. We select particles that stop in D7 by requiring that neither D8 nor the anticoincidence detector be triggered, as well as requiring that the D7 pulse height trigger the high level discriminator. No corrections have been made to the data beyond

Figure 3.1

$\Delta E = E_6$ vs. $E' = E_7$ for boron, carbon, nitrogen, and oxygen isotopes stopping in detector D7 with an incident angle $0°$ (solid lines). Also shown is the "track" for ^{12}C at an incident angle of $30°$ (dashed line).
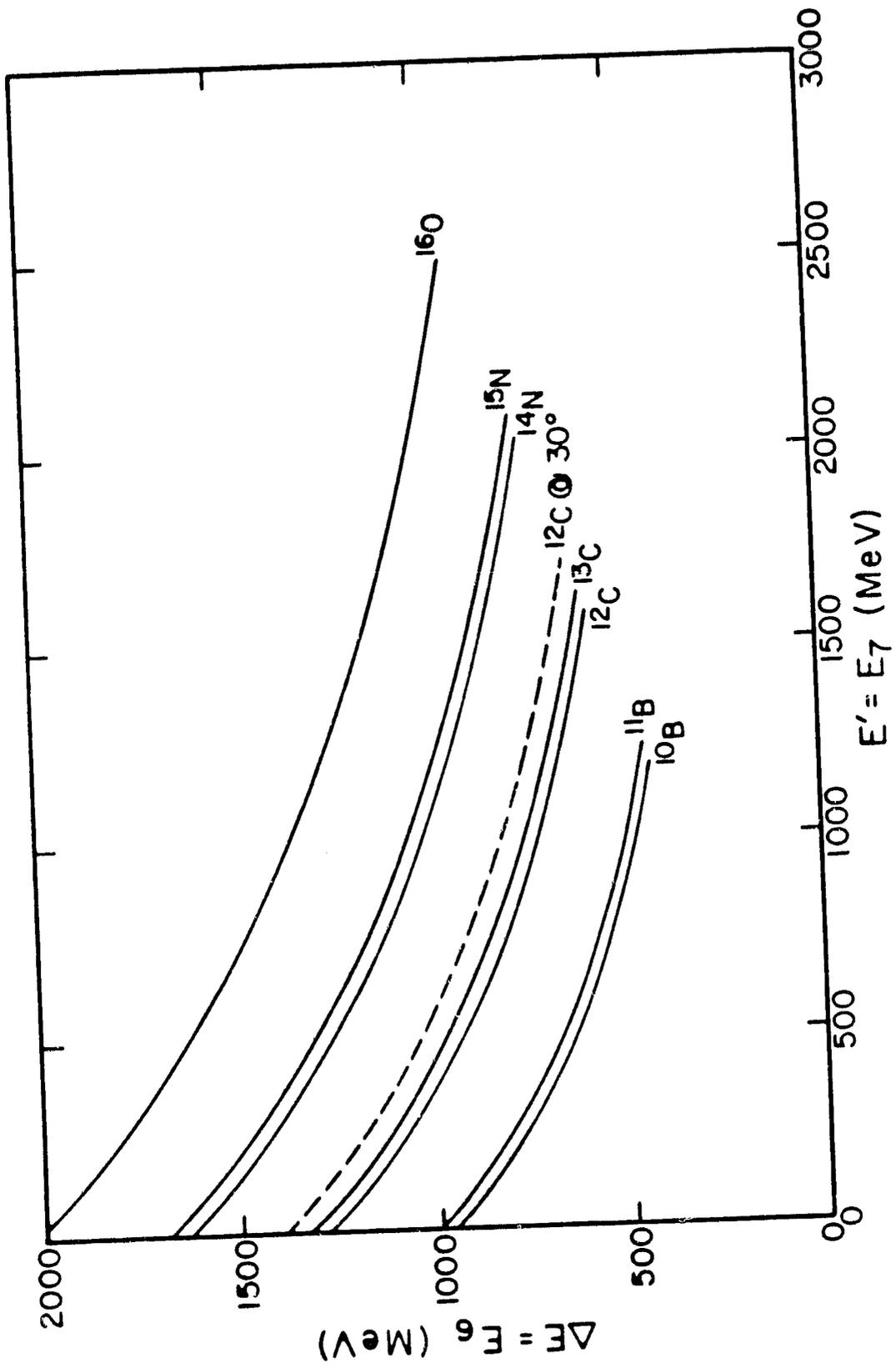
Figure 3.2

L_6 vs. L_7 for particles stopping in detector D7.

a) Raw data (except for PHA calibrations, and inter-detector normalizations).

b) Light collection maps, PMT gain shifts, $\sec \vartheta$ correction.
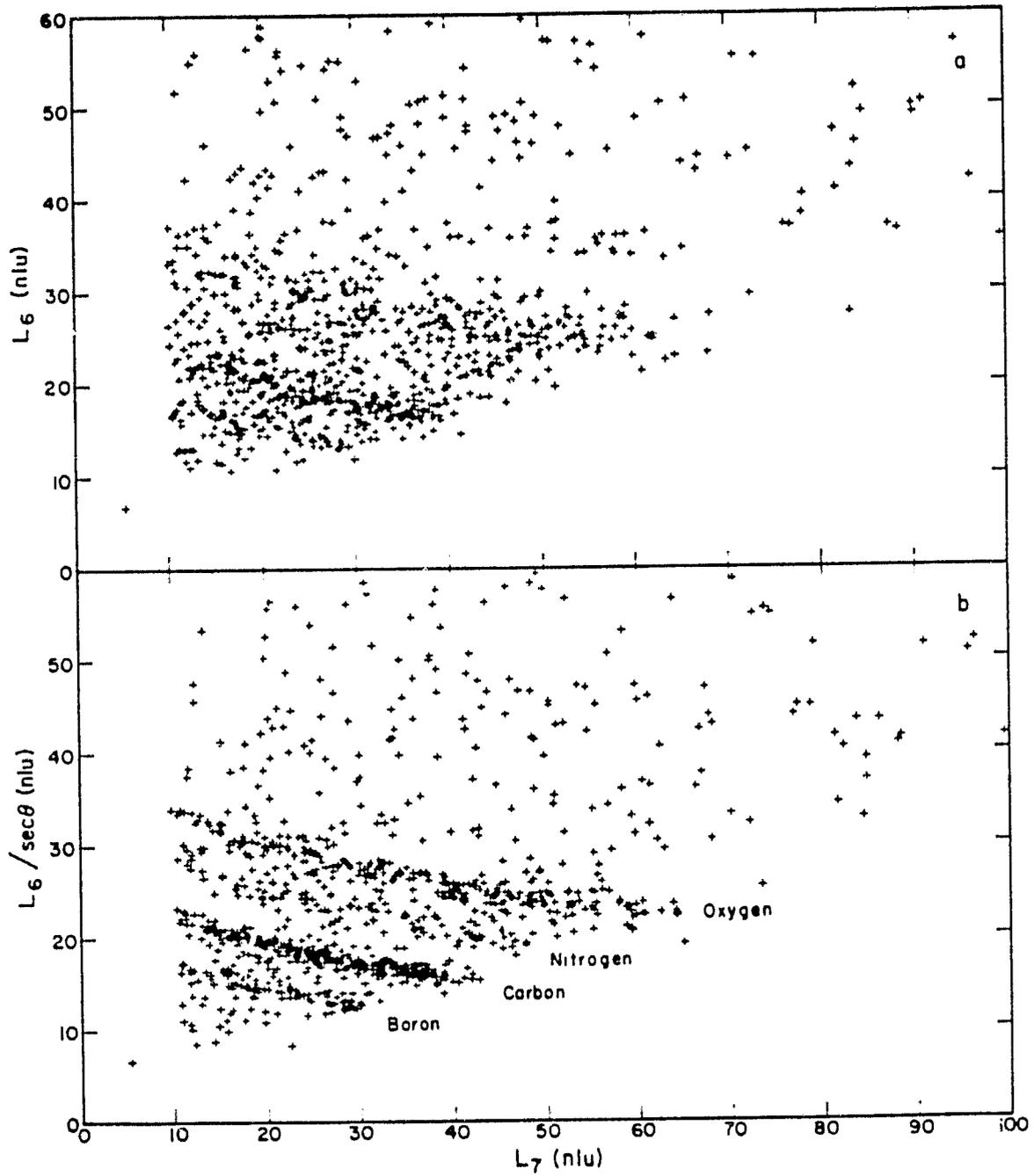
the inter-detector normalizations and PHA calibrations discussed in Chapter 2. Even at this stage one can see poorly resolved boron, carbon, and oxygen element tracks. The data in Figure 3.2b have been corrected according to the Bevalac and residual light collection maps on the basis of their trajectories, and corrected for PMT gain changes on the basis of the appropriate PMT temperatures. In addition, a first order pathlength correction has been made to L_6 by normalizing it to vertical incidence, that is, dividing L_6 by $\sec\vartheta$. This correction ignores higher order effects due to the fact that the particle is slowing down as it traverses D6 so that its specific ionization is increasing. It is, however, sufficient for charge resolution. One can see in Figure 3.2b clear element tracks corresponding to boron, carbon, nitrogen, and oxygen.

We have assigned a charge to each event in Figure 3.2b by empirically determining a family of curves which parametrize the tracks:

$$\ln Z = A \ln\frac{\Delta L}{\sec\vartheta} + B \ln L' + C ,$$

where A, B, and C are independent of Z. The form is suggested by Equation 2.4 with $M = 2Z$ and $\Delta E \ll E'$. In addition to assigning a charge to each event based on its location in the $\dfrac{L_6}{\sec\vartheta} - L_7$ plane, we can plot $\dfrac{L_4}{\sec\vartheta}$ vs. $L_6 + L_7$, $\dfrac{L_3}{\sec\vartheta}$ vs. $L_4 + L_6 + L_7$, and so on (we have not included L_5 because for nitrogen and oxygen the signal out of D5 is between gain ranges of its PHA). For each of these plots we have also empirically determined a family of curves which parametrize the tracks, so that we have six independent charge assignments Z_i, $5 \neq i = 0, 1, \ldots 6$, for each event. We are thus able to eliminate events which undergo a charge-changing

nuclear interaction in the CsI. In Figure 3.3 we show the quantity $\frac{\chi_Z}{Z_{ave}}$ plotted against Z_{ave}, where $Z_{ave} = \sum w_i Z_i$ and $\chi_Z^2 = \sum w_i (Z_i - Z_{ave})^2$ (the weights w_i are determined from the variances of the fits to the tracks, and have been normalized so that $\sum w_i = 1$). There is a clear depletion of non-integral Z_{ave} events as well as a general improvement in charge resolution for small $\frac{\chi_Z}{Z_{ave}}$. That the means of the four charge groups do not all occur at exactly integral values of Z_{ave} is due to the approximations inherent in the choice of the form used for the functional dependence of Z on ΔL and L' (in particular the approximation that A, B, and C are independent of Z).

We show in Figure 3.4a the subset of events in Figure 3.2b for which $4.5 < Z_{ave} < 8.5$ and $\frac{\chi_Z}{Z_{ave}} < 3.5\%$, together with the nominal tracks for $Z = 5,6,7,8$. Figures 3.4b–f consist of the same events as in Figure 3.4a, and show $\frac{L_i}{\sec\vartheta}$ vs. $\sum_{5 \ge j > i} L_j$, for $i = 0,1,...4$. Charge histograms corresponding to Figures 3.2a, 3.2b, and 3.4a are shown in Figures 3.5a–c. Based on the total inelastic cross section for particles in CsI we expect that 20–25% of the events with $5 \le Z \le 8$ will undergo a charge–changing nuclear interaction in the CsI before stopping in D7. This is consistent with the attenuation in events from Figure 3.5b to Figure 3.5c.

From Figure 3.5c we also see that the typical charge resolution is $\sigma_Z \approx 0.17$ charge units. From our earlier discussion this is equivalent to a mass resolution of only 1.3 mass units. Although we have

Figure 3.3

$\frac{\chi_Z}{Z_{ave}}$ vs. Z_{ave}. The boxed regions define a selection criterion for mass

analysis (§3.4, Table 3.1).
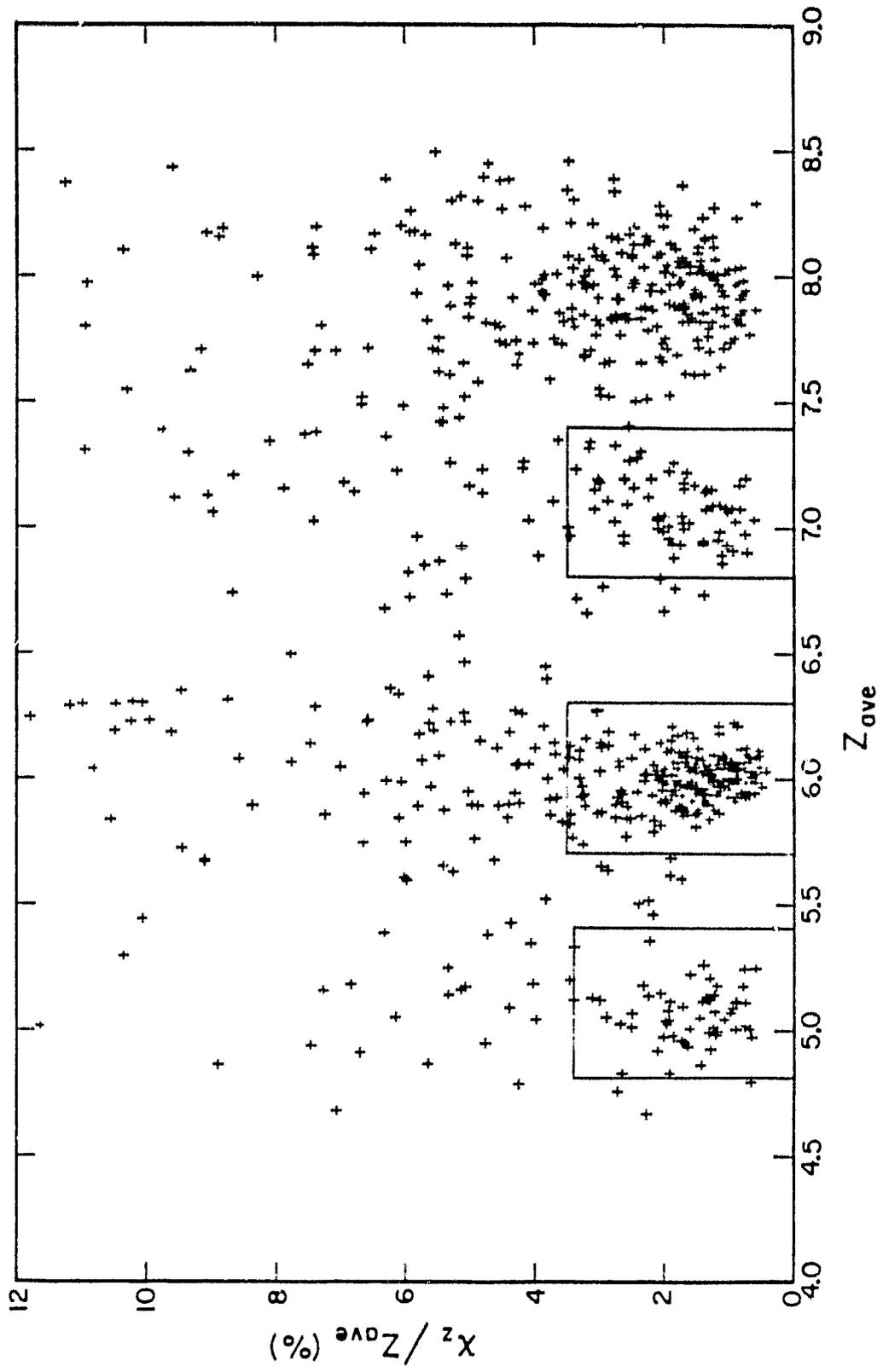
Figure 3.4

$\dfrac{L_i}{\sec\vartheta}$ vs. $\displaystyle\sum_{5\neq j>i} L_j$ for $4.5 < Z_{ave} < 8.5$ and $\dfrac{\chi_Z}{Z_{ave}} < 3.5\%$. Also plotted are the

nominal integral charge tracks. All L's are in nlu.

a) i=6.

b) i=4.

c) i=3.

d) i=2.

e) i=1.

f) i=0.
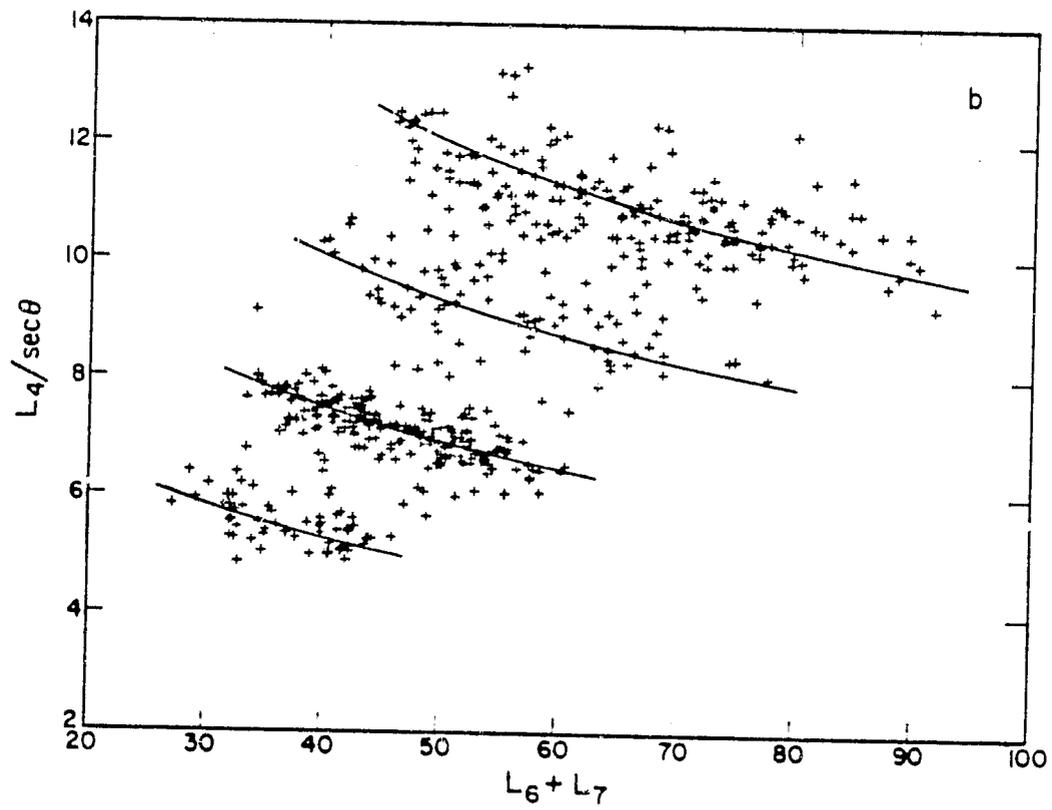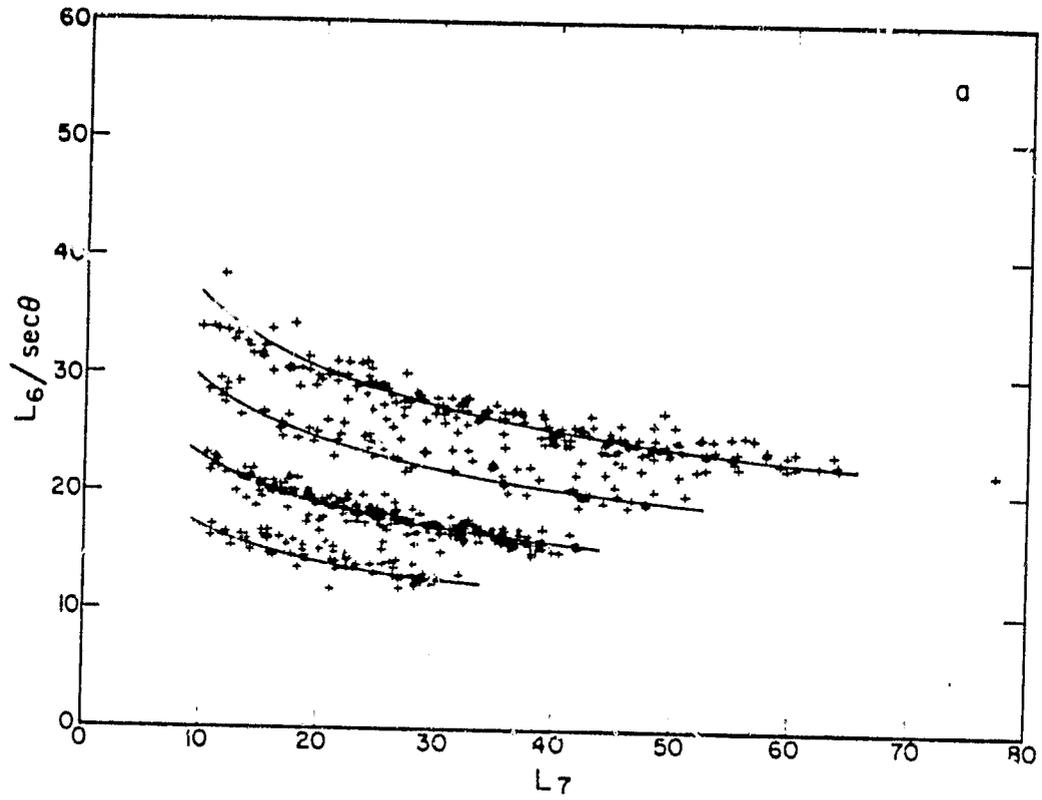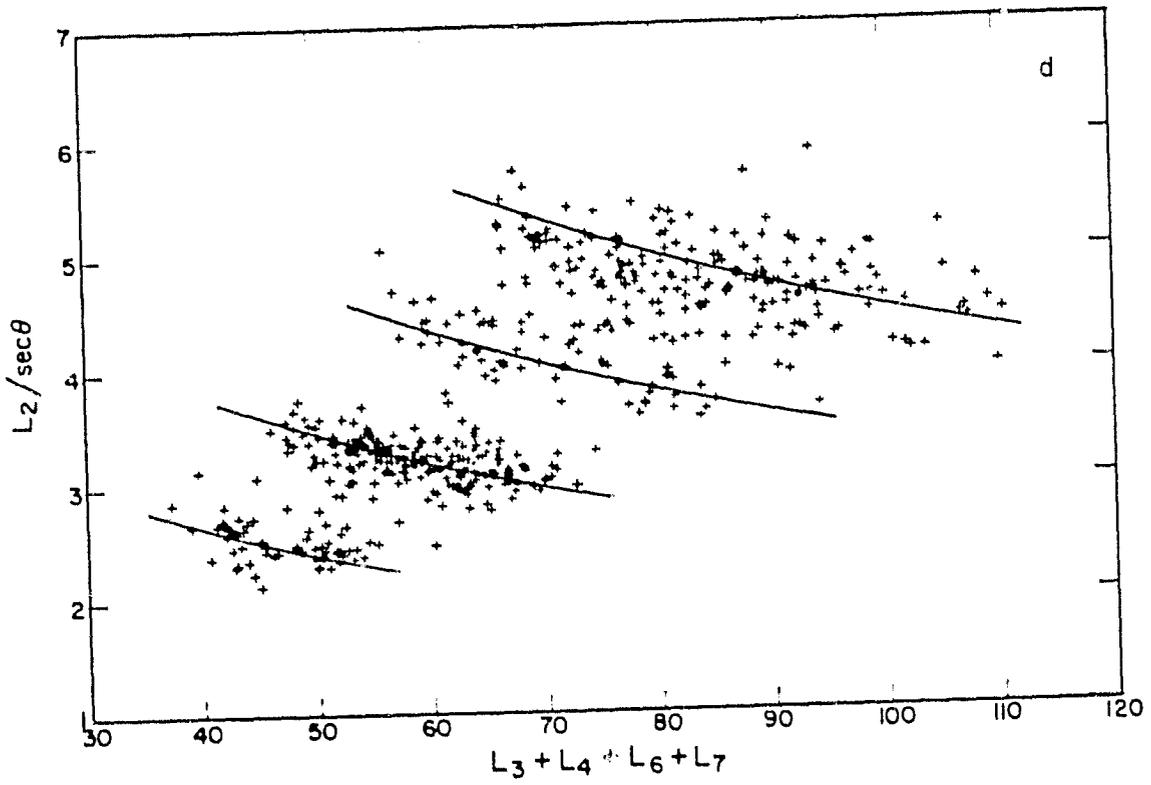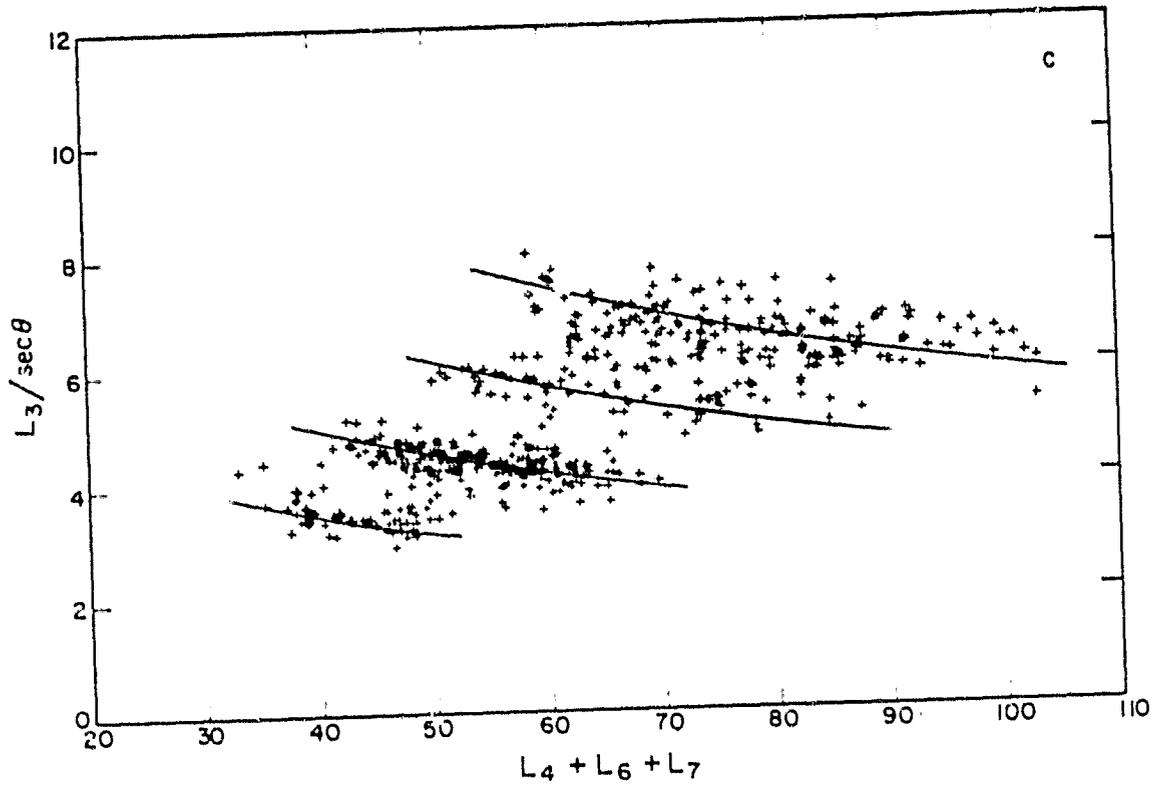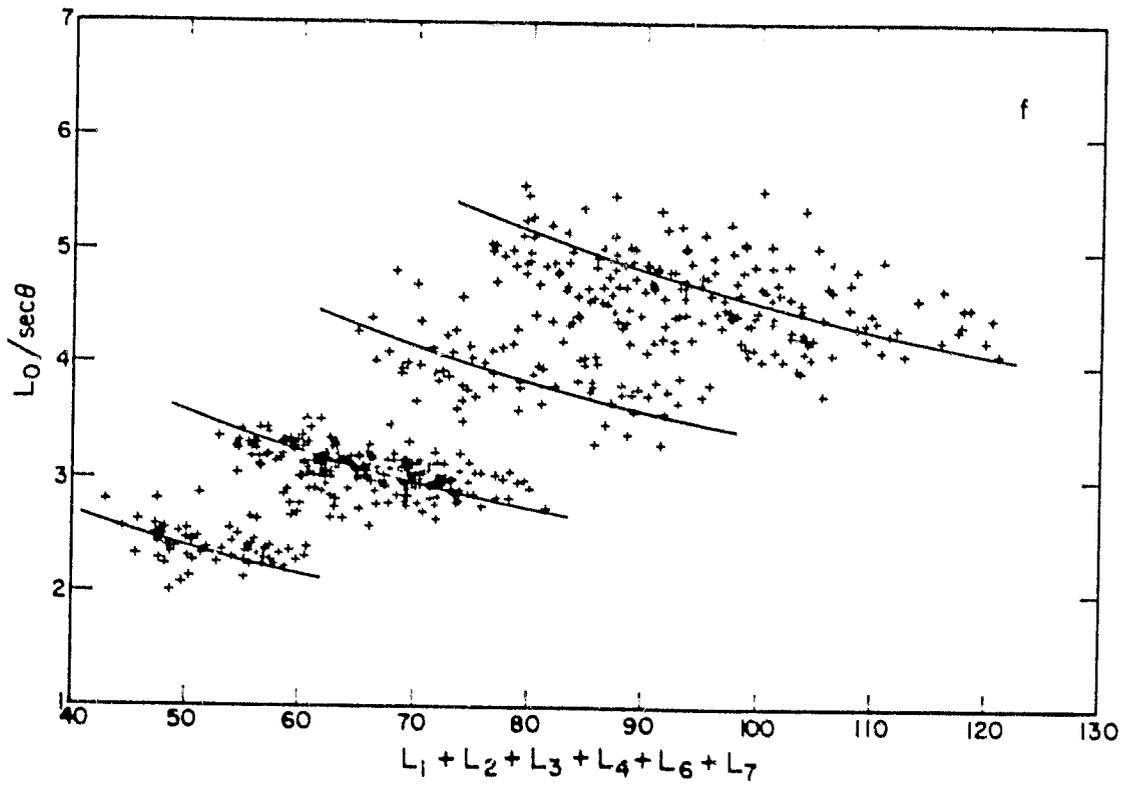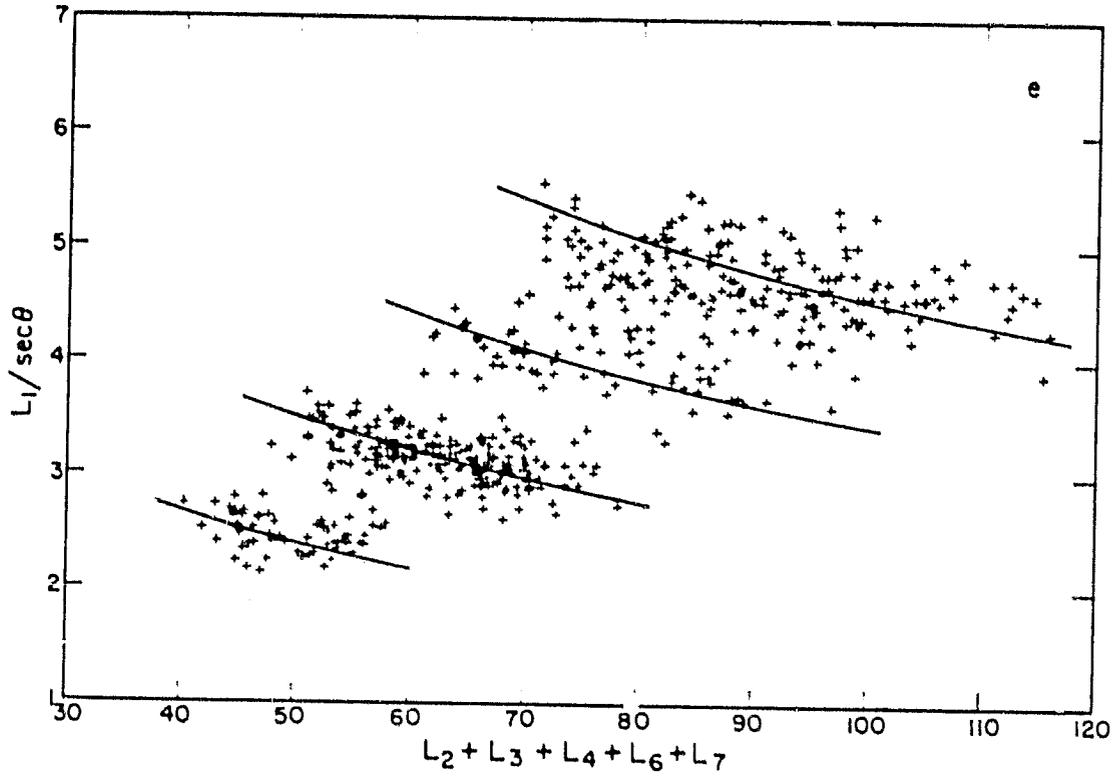
Figure 3.5

Charge histograms (Z_6) for particles stopping in detector D7.

a) PHA calibrations and inter-detector normalizations only; corresponds to Figure 3.2a.

b) Corrections for spatial variations in detector response and PMT temperature, in addition to above. A first-order correction for pathlength has been made by dividing L_6 by $\sec \vartheta$; corresponds to Figure 3.2b.

c) Same as b), except require that $4.5 < Z_{ave} < 8.5$, and $\dfrac{\chi_Z}{Z_{ave}} < 3.5\%$. The attenuation in the "peaks" (defined to be the four charge bins for a given element with the most counts), from b) to c) is $26 \pm 2\%$; for the "valleys" it is $45 \pm 3\%$; the total attenuation is $31 \pm 2\%$.
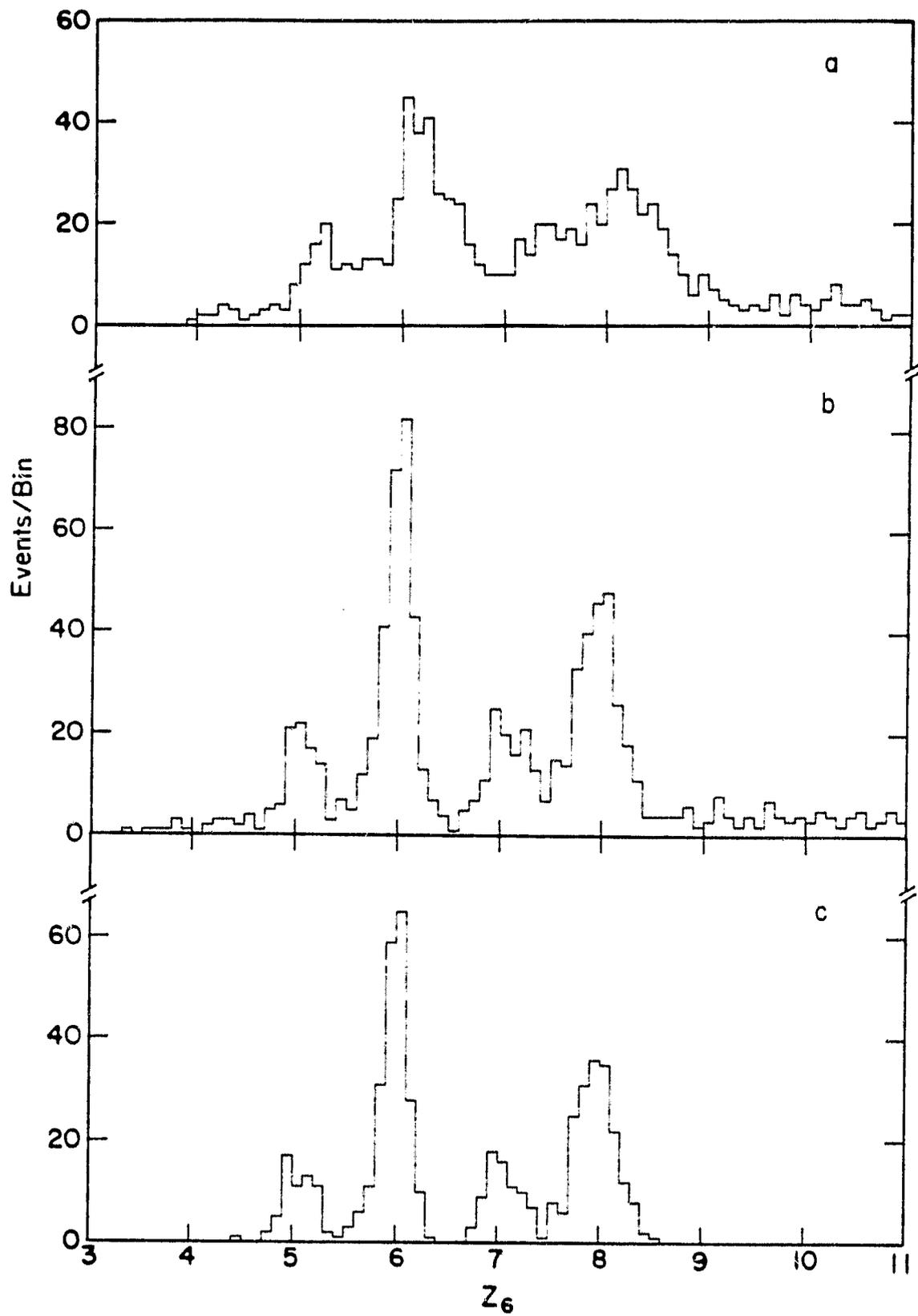
demonstrated that we can identify the charge of each particle on an event-by-event basis, our analysis must be more sophisticated if we hope to resolve isotopes of a single element. We note here that we have not at this point made any selection of events on the basis of the quality of trajectory data because our $\sec \vartheta$ correction is sufficiently naive that to do so would not improve the charge resolution significantly.

3.3 Scintillator Saturation

The ideal situation would be one in which our detectors were perfectly linear, that is, the scintillation light would be directly proportional to the energy deposited. Then a single constant would suffice to correct our measured signal to an energy, and we could simply use Equation 3.1 to calculate the mass for each event. The well known phenomenon of scintillator saturation (Birks 1964) means, of course, that this is not the case. From Figure 3.1 one can calculate that, at $E' = 1\,\text{GeV}$, ΔE for oxygen is a factor of 2.8 greater than that for boron. On the other hand, in Figure 3.4a at $L_7 = 30$ nlu, L_8 for oxygen is only a factor of 2.2 above that for boron. This is already a first order measurement of heavy ion saturation in CsI.

To deduce the light-energy relationship for CsI we do not assume that such a relationship is necessarily the same for different elements because a particle with a given charge and total kinetic energy has a "Bragg curve" (dE/dx vs. penetration depth) very different from that of a particle with the same energy but a different charge, and we expect that the differential scintillation efficiency dL/dE will depend mainly on dE/dx. We thus confine ourselves to a single element at a time, and use

the carbon data to illustrate our procedure. Since we expect that carbon will consist primarily of ^{12}C we *assign* to each event with $Z = 6$ a mass $M = 12$ amu. Our goal is some functional relationship $\frac{E}{L} = \alpha(L)$, where L (in "nlu"; see §2.2.5) is the total light out of a scintillator in which a particle of total kinetic energy E (in MeV) deposits all of its energy. Our zeroth order (false) assumption is that $\alpha(L) = $ constant $= \alpha_0$ (perfect linearity). Then Equation 3.1 becomes

$$R_p\left[\frac{\alpha_0(\Delta L + L')}{M}\right] - R_p\left[\frac{\alpha_0 L'}{M}\right] = \frac{Z^2 t \sec \vartheta}{M} \qquad (3.2).$$

Having set $M = 12$ amu, all quantities in Equation 3.2 are known except α_0. For each event, then, we calculate the value of α_0 required to satisfy the equation. We then scatter plot α_0 vs. L' and $\Delta L + L'$ (Figure 3.6a) and see that our assumption of constant α is false (as expected). However, we can use the scatter plot to define a function $\delta\alpha(L_1, L_2) = \overline{\alpha}(L_1) - \overline{\alpha}(L_2)$ by fitting a straight line $\overline{\alpha}$ to the α_0 vs. L' portion of the plot. The function $\delta\alpha$ tells us how different E/L is for $L_1 = L' + \Delta L$ and $L_2 = L'$.

For our next iteration we no longer assume, then, that α is constant, and Equation 3.2 becomes

$$\Gamma_p\left[\frac{[\alpha(L') + \delta\alpha(\Delta L + L', L')](\Delta L + L')}{M}\right] - R_p\left[\frac{\alpha(L')L'}{M}\right] = \frac{Z^2 t \sec \vartheta}{M} \qquad (3.3).$$

Again, every quantity in Equation 3.3 is known for each event (we derived $\delta\alpha$ from our first iteration) except α, so we again calculate α event by event and scatter plot this vs. L'. We continue iterating in this fashion until the $\delta\alpha$ function we put in is consistent with the $\overline{\alpha}$ function we get out, in which case $\overline{\alpha}(L)$ is E/L for ^{12}C. In Figure 3.6b we show a scatter plot of $\alpha(L')$ and $\alpha(\Delta L + L')$ vs. L' and $\Delta L + L'$ as deduced from the last iteration. In addition we show the straight line fit $\overline{\alpha}(L)$ deduced from the

Figure 3.6

Determination of $\alpha(L) = \dfrac{E}{L}$ for carbon. Crosses correspond to $L' = \underline{L_7}$,

circles to $\Delta L + L' = L_5 + L_6 + L_7$.

a)First iteration (assumes α = constant).

b)Convergence.

The selection criteria are $5.7 < Z_{avc} < 6.3$, $\sec \vartheta < 1.2$, and $\chi_{x,y} < 5\,mm$.
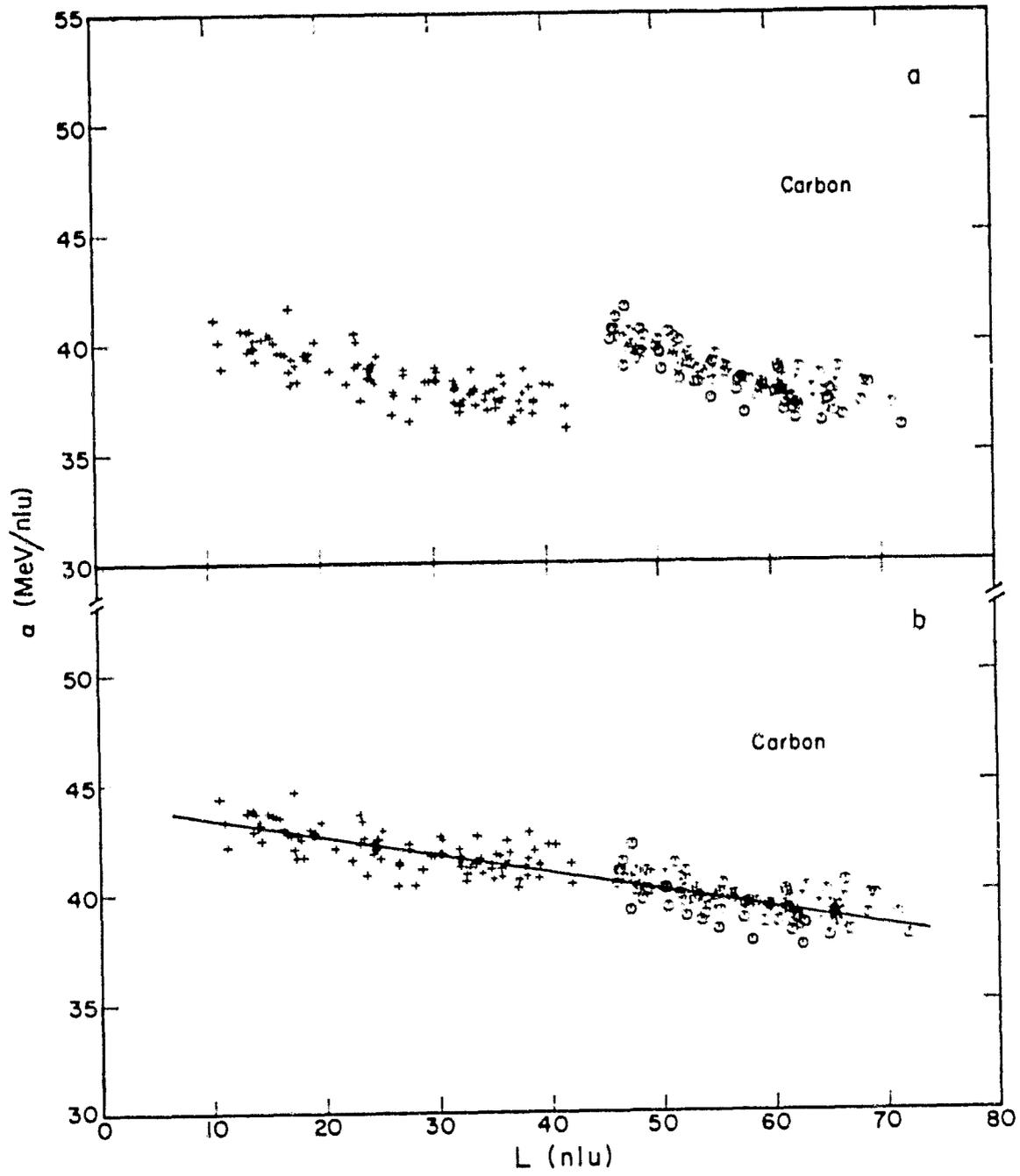
previous iteration from which came $\delta\alpha$ used in the last iteration. The agreement is good, indicating that the procedure has converged.

For boron and nitrogen the procedure for determining the E/L function is identical, except that, since these elements are expected to consist of substantial quantities of more than one isotope, we assign to each event of the given element the same *average* mass arbitrarily. Since we expect boron to consist of ^{10}B and ^{11}B, we assign 10.5 amu to each event with $Z = 5$. Similarly, nitrogen consists of ^{14}N and ^{15}N, so we assign 14.5 amu to each event with $Z = $. : will take into account this arbitrary assignment of average mas. n.ed in determing the E/L function by letting the offset of the mass scale be a free parameter later on. We show in Figures 3.7a,b the convergence of the iterations for these elements.

We have found that there is a small but non-negligible dependence of α on angle ϑ, and have taken this into consideration by adding another term to the form used for $\overline{\alpha}$. Specifically, we have used the form $\overline{\alpha}(L,\vartheta) = AL + B + C \sec\vartheta$, and find that $C > 0$. As $\sec\vartheta$ varies from 1 to 1.2, $\overline{\alpha}$ varies by typically 3%. Several candidates have been identified which might explain this dependence, including i) systematic overestimate of the nsec mm^{-1} delay in the MWPC delay lines (§2.2.1), ii) thin dead layer in the ΔE-detector, iii) errors in inter-detector normalizations (§2.2.5), and iv) systematic error due to the assumption that $\dfrac{E}{L}$ is related linearly to L (see below), none of which is in itself sufficient to explain the effect, although all have the right sign.

In Figure 3.8 we show the relationship between dL/dE as deduced

Figure 3.7

Determination of $\alpha(L) = \dfrac{E}{L}$ for a) boron and b) nitrogen. For both elements, L' (crosses) = L_7. Circles correspond to $\Delta L + L'$. For boron, $\Delta L = L_5 + L_6$, for nitrogen, $\Delta L = L_6$. For boron we require $4.8 < Z_{ave} < 5.4$, for nitrogen $6.8 < Z_{ave} < 7.4$. For both elements only events with $\sec \vartheta < 1.2$ and $\chi_{x,y} < 5\,mm$ are used.
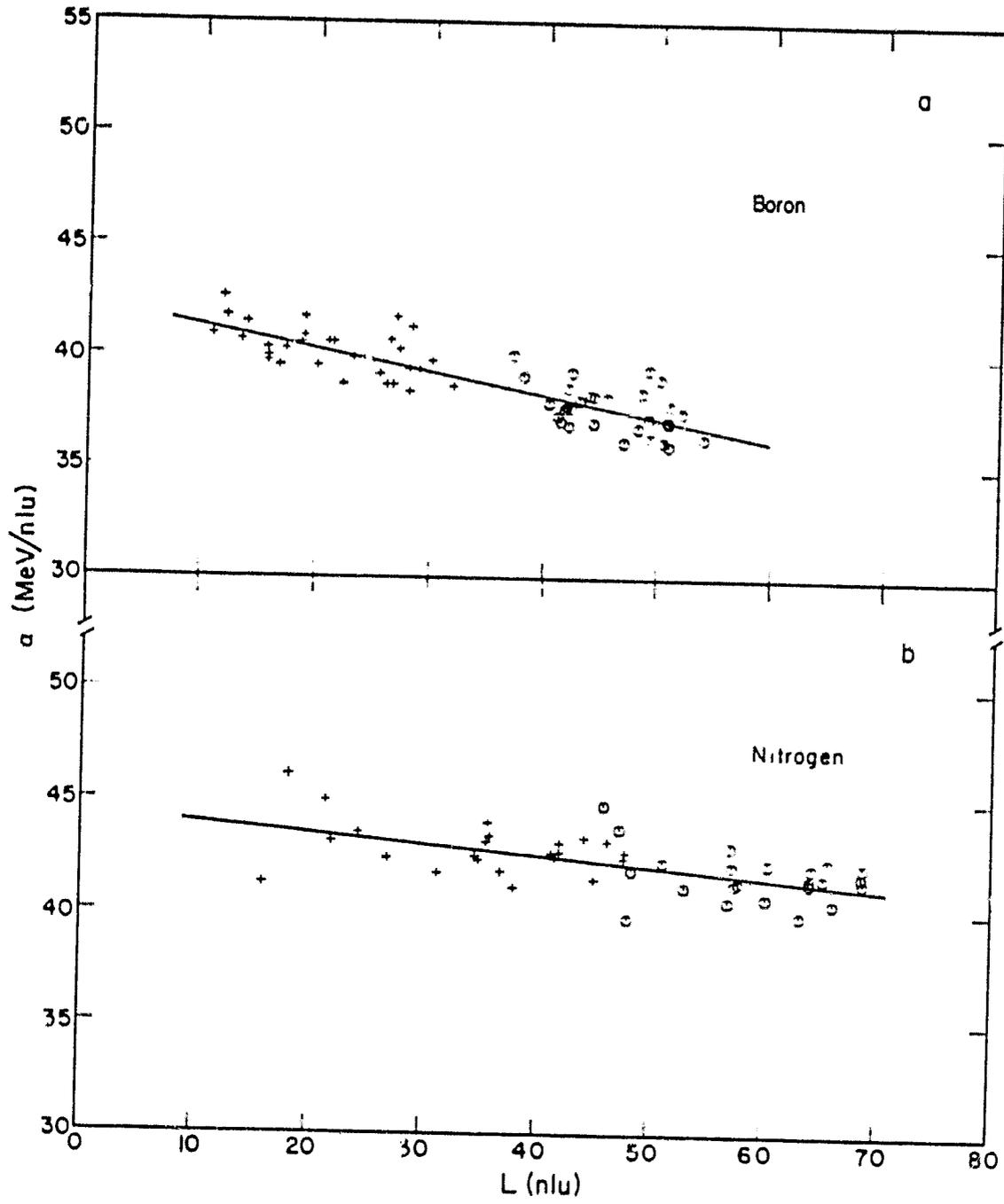
from our E/L functions and the specific ionization dE/dx for boron, carbon, and nitrogen, using

$$\frac{dL}{dE} = (\frac{dE}{dL})^{-1} = \frac{1}{\frac{d}{dL}(L\frac{E}{L})} = \frac{1}{2AL + B + C \sec \vartheta} \quad .$$

The curves have been normalized to dL/dE for minimum ionizing carbon (Figure 2.7). Given that the size of the error bars (which depend on the statistical errors in A, B, and C) are greater than or of the order of the separation between charges, our data are consistent with dL/dE depending only on dE/dx, independent of charge and detailed structure of the distribution in energy transfer to electrons in the ionization energy loss process.

The shapes of the curves in Figure 3.8 are a consequence of the assumption that $\frac{E}{L}$ is related linearly to L, and should not be interpreted too literally [other investigations (see Birks 1964 for a summary) suggest that $\frac{dL}{dE}$ might be linear in $\ln \frac{dE}{dx}$]. To estimate the magnitude of the error we make in mass due to this assumption we have performed an analytical calculation which assumes i) $\frac{dL}{dE} = a + b \ln \frac{dE}{dx}$ (specifically, a straight line on Figure 3.8 which connects the endpoints of the carbon curve) and ii) the power law approximation $R_p(\varepsilon) = k \varepsilon^a$. With these assumptions, we calculate ΔL and L' pairs, for a given nuclide, as a function of the range R_7 in D7. These pairs are then analyzed, just as was the flight data, to derive a straight-line $\frac{E}{L}$ vs. L relationship [because of assumption i), $\frac{E}{L}$ vs. L is in fact nonlinear]. We then use the derived linear relationship to convert the L's into E's, and finally

Figure 3.6

Differential scintillation efficiency dL/dE vs. specific ionization dE/dx for boron, carbon, and nitrogen. The dL/dE axis has been normalized to minimum ionizing carbon (Figure 2.7), where dE/dx = 20.3 MeV mm^{-1}.
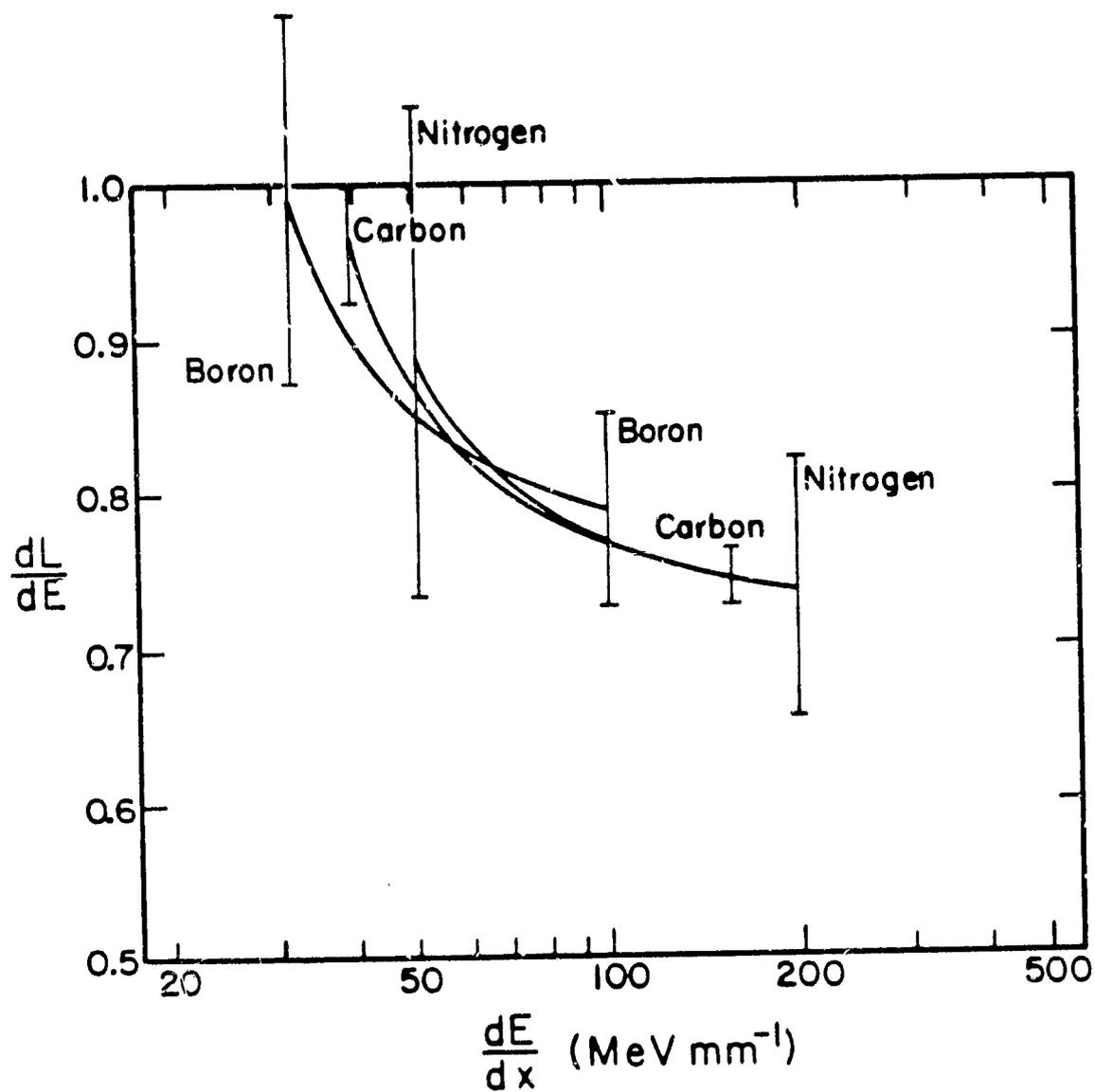
calculate masses using Equation 2.4. We find that the resulting rms variation in mass, for $2\,mm \lesssim R_7 \lesssim 17\,mm$ and $1 \lesssim sec\vartheta \lesssim 1.2$, is $0.05\,amu$ for ^{10}B, $0.07\,amu$ for ^{12}C, and $0.11\,amu$ for ^{14}N.

Given an E/L function for an element, how might we expect it to differ for different isotopes of that element? A reasonable assumption is that dL/dE depends only on dE/dx, since two particles with the same charge and specific ionization (and therefore the same velocity) give rise to identical electron energy transfer spectra. Since the velocity is equivalent to kinetic energy per unit mass, we have

$$\frac{dL}{dE}(E,M,Z) = f_Z\left(\frac{E}{M}\right),$$

so that

$$L(E,M,Z) = \int_0^E dE \frac{dL}{dE} = M \int_0^{E/M} d\varepsilon \, f_Z(\varepsilon)$$

upon change of variable $\varepsilon = E/M$. For another isotope of mass M' we have

$$L(E,M',Z) = M' \int_0^{E/M'} d\varepsilon \, f_Z(\varepsilon), \text{ so that}$$

$$L(E,\vartheta,M',Z) = \frac{M'}{M} L\left(E \frac{M}{M'},\vartheta,M,Z\right) \qquad (3.4)$$

where we now explicitly include the ϑ-dependence discussed earlier. Thus once we have our E/L function for the average mass of an element we can use Equation 3.4 to tell us what it is for particular isotopes.

3.4 Mass Analysis

We can now calculate masses on an event by event basis. The procedure is to calculate M such

$$R_p\left[\frac{E(L,\vartheta,M,Z)}{M}\right] - R_p\left[\frac{E(L',\vartheta,M,Z)}{M}\right] = \frac{Z^2\, t\, sec\, \vartheta}{M} \qquad (3.5).$$

[we use $E(L,\vartheta,M,Z)$ here to denote the total kinetic energy E of a particle of mass M and charge Z at incident angle ϑ which creates a total amount

of light L as it comes to rest in a scintillator], using our E/L function and the scaling implied by Equation 3.4 to calc̲ ̲ ̲ ̲ ̲ E(L,ϑ,M,Z) given a measured L and ϑ. The problem with this approach is that it uses unphysical nonintegral masses in the conversion from light to energy. Of course we have no a priori knowledge of the mass to tell us which is the correct M to use in the conversion. Since our ultimate goal is to obtain relative abundances of the various is̲ opes, we can incorporate this lack of knowledge directly into our maximum likelihood analysis of the mass distribution, which we now describe.

Suppose a given element consists of two isotopes, fraction f_1 of mass m_1 and fraction $1-f_1$ of mass m_2. We assume our resolution function for a single isotope is a gaussian with variance σ^2. For each event we calculate, according to Equation 3.5, two masses, M_1 assuming m_1 in the L to E conversion and M_2 assuming m_2 in the L to E conversion. The probability that a mass distribution characterized by σ^2 and f_1 results in the measurement M_1 and M_2 is then

$$p(M_1,M_2) = \frac{1}{\sqrt{2}\,\pi\,\sigma} \left[f_1 \exp\left[-\frac{(M_1-m_1)^2}{2\sigma^2} \right] + (1-f_1)\exp\left[-\frac{(M_2-m_2)^2}{2\sigma^2} \right] \right].$$

A maximum likelihood analysis consists of forming the likelihood function $L(f_1) = \prod_j p_j$, where p_j is the probability of the jth event. The maximum likelihood estimate of f_1 is that which maximizes $L(f_1)$. The extension to more than two isotopes is straightforward.

We have used this technique to calculate maximum likelihood estimates of the abundances $^{10}B/B$, $^{13}C/C$, and $^{15}N/N$. Because the gain of our mass scale is fixed by the mass scaling of the light to energy function, we have not allowed m_1-m_2 to vary in the analysis, but to take

into account our arbitrary assignment of average mass in determining the E/L functions, we take the offset of our mass scale to be a free parameter. In addition we allow σ to vary, so that the likelihood function depends on f_1, m_1, and σ, with fixed m_1-m_2. For carbon we expect roughly 1% of the events to be ^{11}C due to nuclear interactions in the atmosphere above our instrument (§4.2), so that for this element we have allowed the quantity $\dfrac{^{11}C}{C}$ to vary between 0 and 2%.

For boron and carbon we have used the sum of L_5 and L_6 as the ΔE measurement and L_7 as the E' measurement. For these elements we have also separately calculated masses using i) D6 as the ΔE detector and D7 as the E' detector and ii) D5 as the ΔE detector and the sum of D6 and D7 as the E' detector, allowing us to reject events if these masses are inconsistent. Because we do not have L_5 for nitrogen, we have only the mass i) in that case.

We have made scatter plots of $M_{^{11}B}$ (the notation indicates the mass calculated using Equation 3.5 assuming the subscripted isotope in the L to E conversion), $M_{^{12}C}$, and $M_{^{15}N}$ versus such quantities as $\sec\vartheta$, L_5, L_6, and L_7 to be sure that our mass distributions are not biased with respect to these quantities. In addition, we have plotted mass versus χ_x and χ_y to see whether our resolution can be improved by rejecting events with large values of these parameters which characterize the quality of trajectory data (§2.2.1, Appendix A).

We show in Figures 3.9a–d scatter plots of $\sec\vartheta$, ΔM [denoting the difference between the masses i) and ii) above], χ_x, and χ_y versus $M_{^{12}C}$, and similar plots for $M_{^{11}B}$ and $M_{^{15}N}$ in Figures 3.10a–d and 3.11a–d,

respectively. Because we have reasonable statistics for carbon, our selection criteria for all elements are to a large degree based on the carbon data. The cuts at $\sec\vartheta = 1.2$, $\Delta M = \pm 0.8\,$amu, and $\chi_x = 4\,$mm all occur at or near values where there is a discontinuity in the distribution of the quantity. There are two cuts for χ_y, depending on whether three or four y-MWPC measurements were used in determining the y-trajectory (no events appear with $\chi_y > 3\,$mm when four y-measurements were used because such events were re-analyzed after discarding one of the four; see Appendix A). For boron we have excluded events for which $\chi_y > 2\,$mm when only three y-measurements were used because two of the three events so excluded (Figure 3.10d) have $M_{11_B} < 10\,$amu, and the exclusion significantly improves the error in the $\frac{^{10}B}{B}$ determination. The slightly smaller value of the $\frac{\chi_z}{Z_{ave}}$ cut for boron eliminates a single event with an anomalously low mass. The Z_{ave} cuts are all of width 0.6 charge units and are centered approximately on the mean Z_{ave} for the particular element (Figure 3.3). From Figure 3.11b we see that most of the nitrogen events with an anomalously low or high mass are correlated with small L_γ, a region where the $\frac{E}{L}$ function is poorly known (Figure 3.7b). We have thus excluded nitrogen events for which $L_\gamma < 20$.

In Table 3.1 we summarize the selection criteria, parameters used and range of variation, and results of our maximum likelihood analyses, and in Figure 3.12 show mass histograms based on those results. Each histogram has two mass scales associated with it corresponding to which isotope is assumed in the conversion from light to energy. (We can do

Figure 3.9

Carbon selection. Scatter plots of a) $\sec\vartheta$, b) ΔM, c) χ_x, and d) χ_y vs. M_{12C}. Circles in d) indicate events for which all four y's were used in determining the y-trajectory; crosses indicate that only three y's were used. The selection criteria are indicated by the hatched lines.
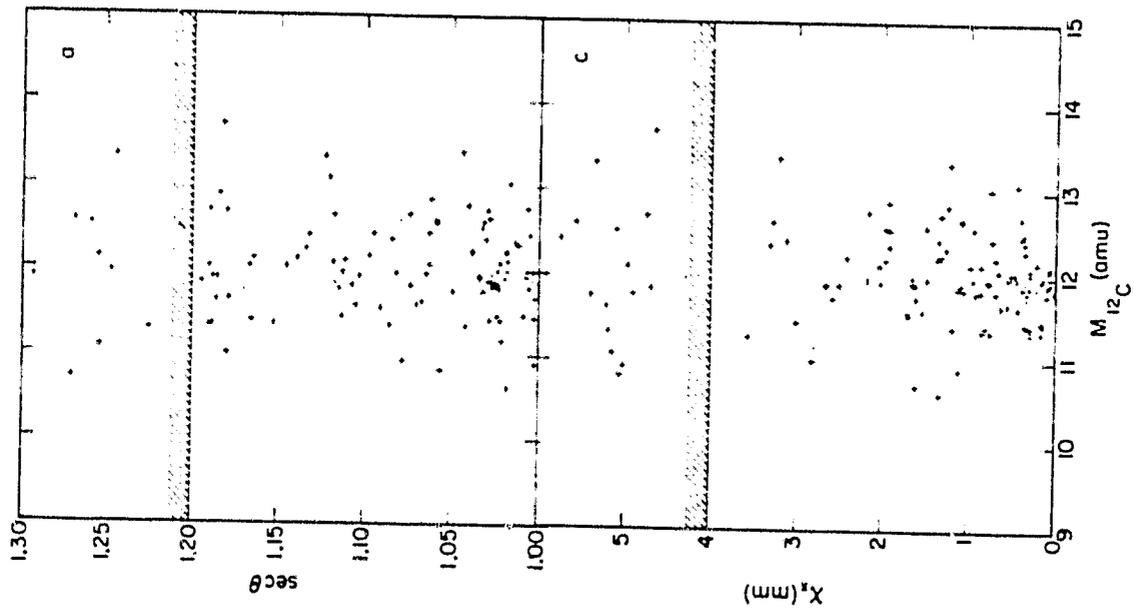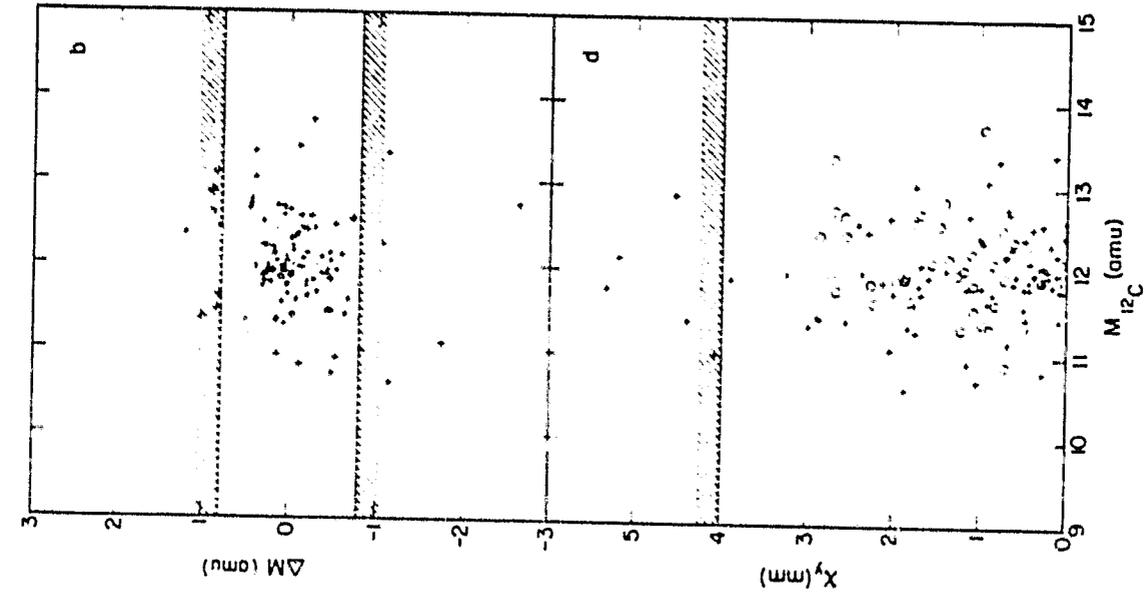
Figure 3.10

Boron selection. Scatter plots of a) $\sec\vartheta$, b) ΔM, c) $\dot{\lambda}_x$, and d) χ_y vs. M_{11_B}. Circles in d) indicate events for which all four y's were used in determining the y-trajectory; crosses indicate that only three y's were used. The selection criteria are indicated by the hatched lines. In d), the hatched line applies only to the crosses.
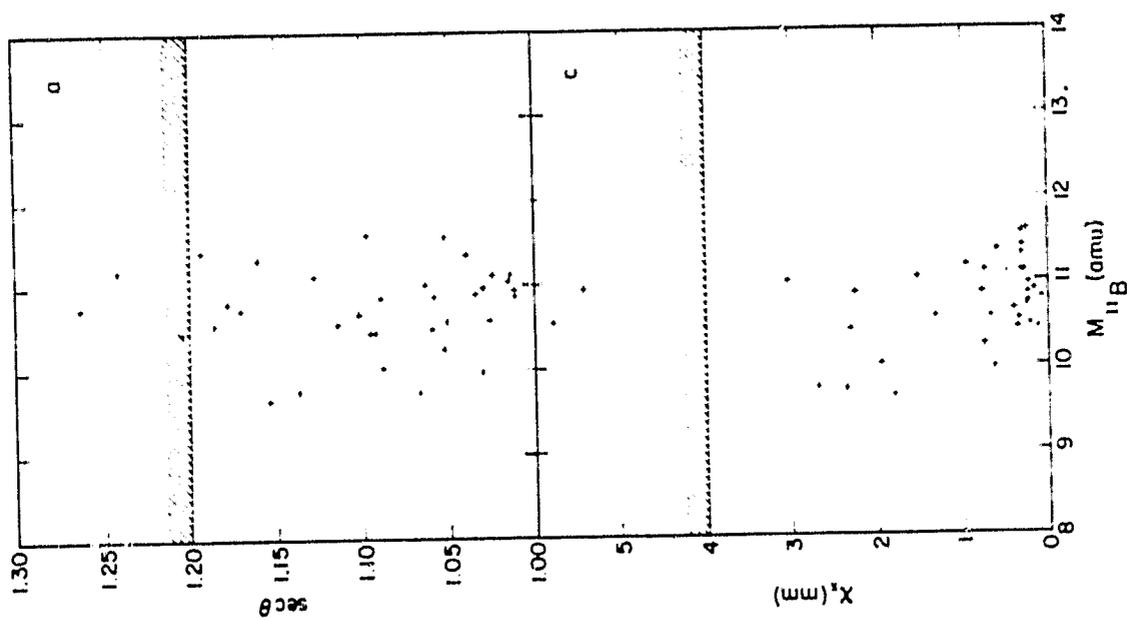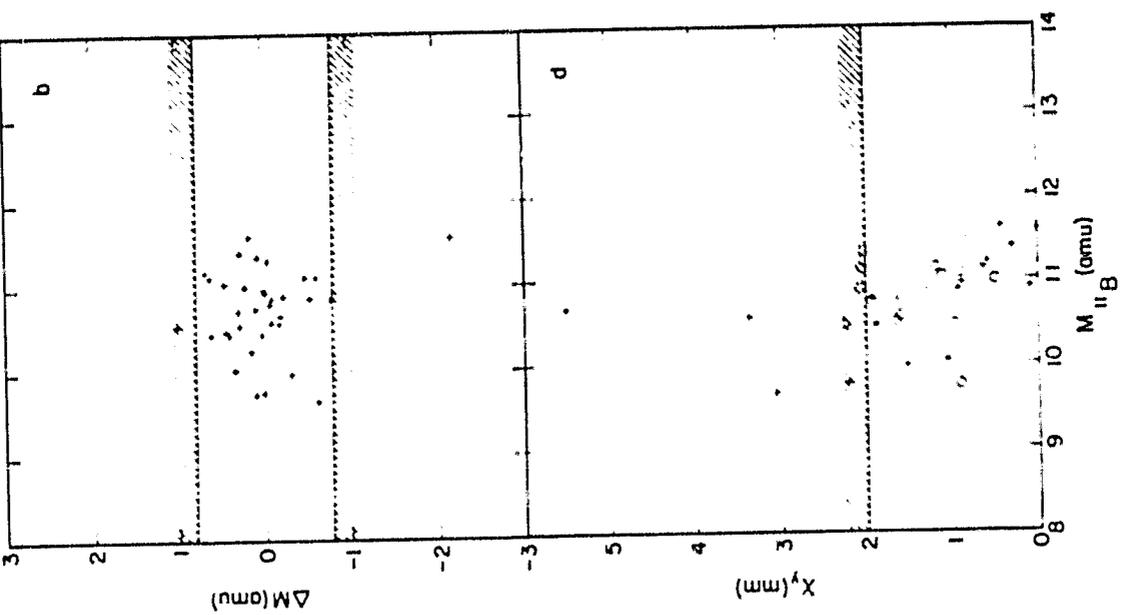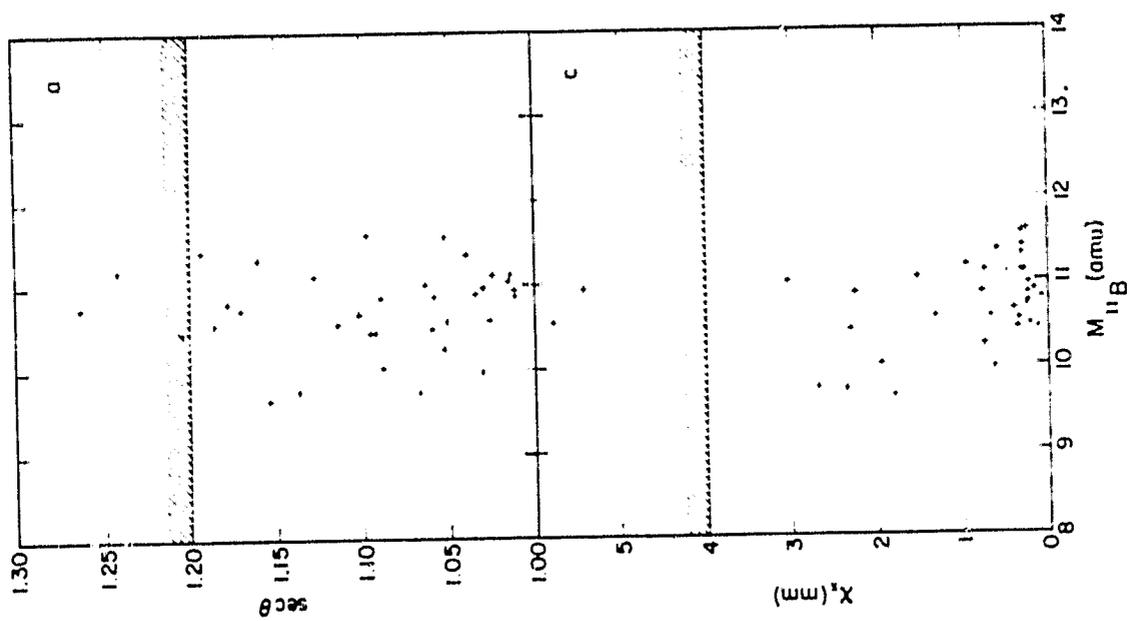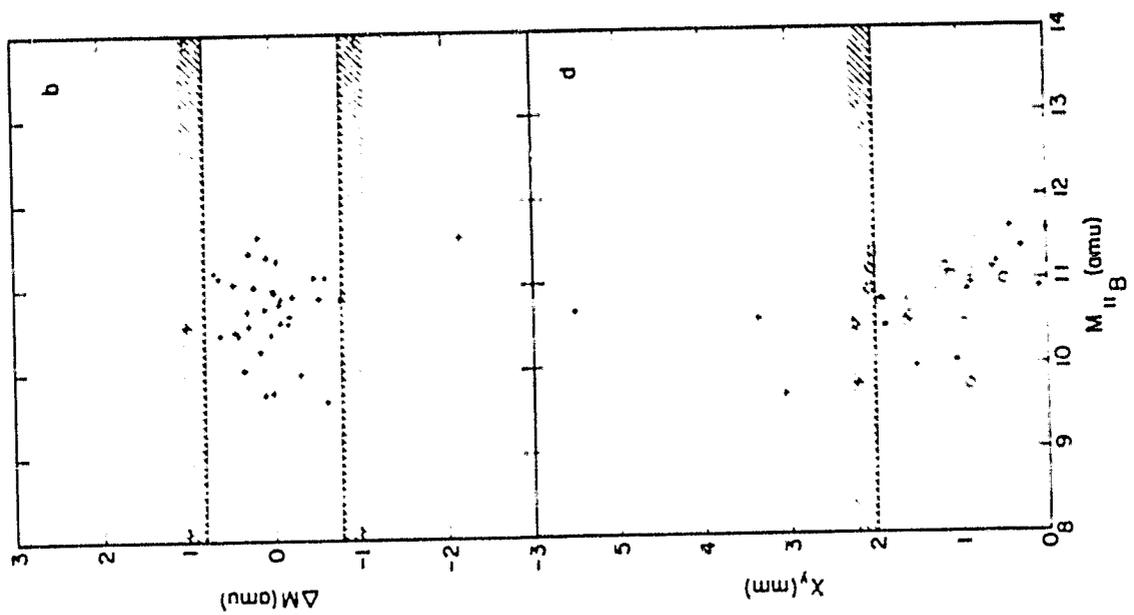
Figure 3.11

Nitrogen selection. Scatter plots of a) secϑ, b)L_7, c) χ_x, and d) χ_y, vs. M_{15_N}. Circles in d) indicate events for which all four y's were used in determining the y-trajectory; crosses indicate that only three y's were used. The selection criteria are indicated by the hatched lines.
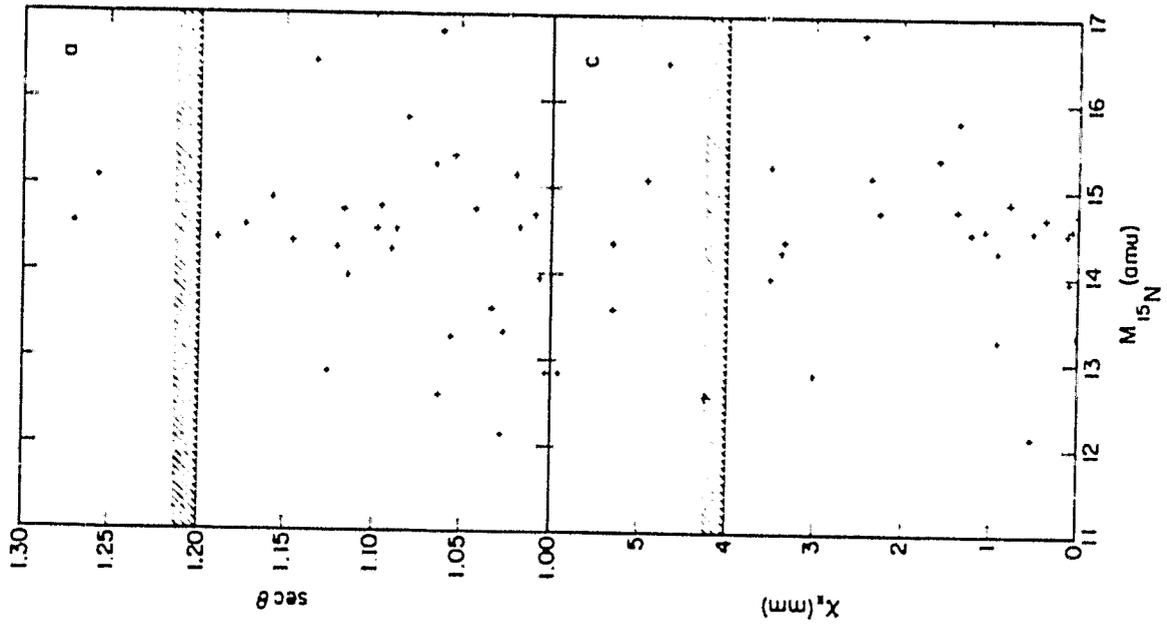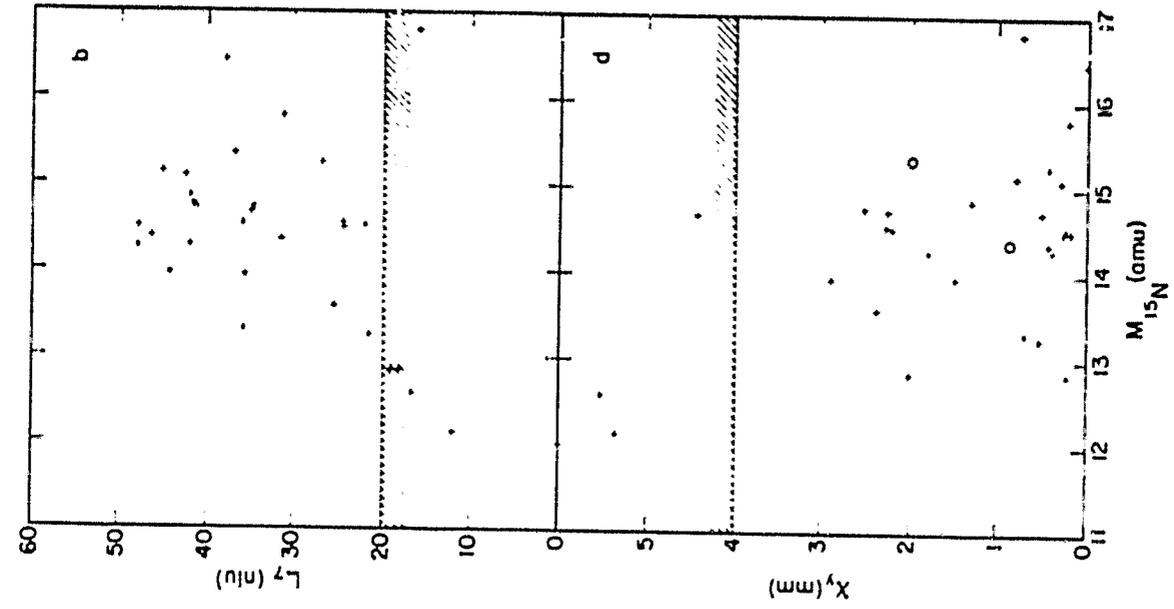
Table 3.1 Maximum Likelihood Analyses

	Events	Selection(1)	Variation of Parameters	Best Value(2)	Isotopic Abundance(3)
Boron	28	$\chi_Z/Z_{ave} < 3.4\%$ $4.8 \leq Z_{ave} \leq 5.4$ $\sec\vartheta < 1.2$ $\|\Delta M\| < 0.8$ pmu $\chi_x < 4$ mm $\chi_y < 3$ (2) mm	$0.26 \leq \sigma \leq 0.38$ pmu $9.85 \leq m_1 \leq 10.05$ pmu (nominal $m_1 = 9.94$ pmu)	$\sigma = 0.32 \pm 0.06$ pmu $m_1 = 9.94 \pm 0.08$ pmu	$^{10}B/B = 0.36^{+0.18}_{-0.12}$
Carbon	79	$\chi_Z/Z_{ave} < 3.5\%$ $5.7 \leq Z_{ave} \leq 6.3$ $\sec\vartheta < 1.2$ $\|\Delta M\| < 0.8$ pmu $\chi_x < 4$ mm $\chi_y < 3$ (4) mm	$0.30 \leq \sigma \leq 0.42$ pmu $11.75 \leq m_1 \leq 12.05$ pmu (nominal $m_1 = 11.91$ pmu)	$\sigma = 0.37 \pm 0.04$ pmu $m_1 = 11.89 \pm 0.05$ pmu	$^{13}C/C = 0.06^{+0.12}_{-0.01}$
Nitrogen	19	$\chi_Z/Z_{ave} < 3.5\%$ $6.8 \leq Z_{ave} \leq 7.4$ $\sec\vartheta < 1.2$ $L_\eta > 20$ nlu $\chi_x < 4$ mm $\chi_y < 3$ (4) mm	$0.40 \leq \sigma \leq 0.80$ pmu fix $m_1 = 13.89$ pmu (nominal value)	$\sigma = 0.50 \pm 0.10$ pmu	$^{15}N/N = 0.42^{+0.19}_{-0.17}$

Notes:

(1) Values of χ_y in parentheses correspond to the selection criteria used when only three Y-MWPC's are used in determining the y-trajectory.

(2) Errors calculated by taking the second derivative of the likelihood function at its maximum (Mathews and Walker 1970).

(3) Errors calculated by integration of the likelihood function; they correspond to the 68.3% confidence interval and include uncertainties in m_1 and σ.

Figure 3.12

Mass histograms for a)carbon, b)boron, and c)nitrogen. The different scales for the horizontal axes are labeled according to the assumed mass in the L to E conversion, as explained in the text.
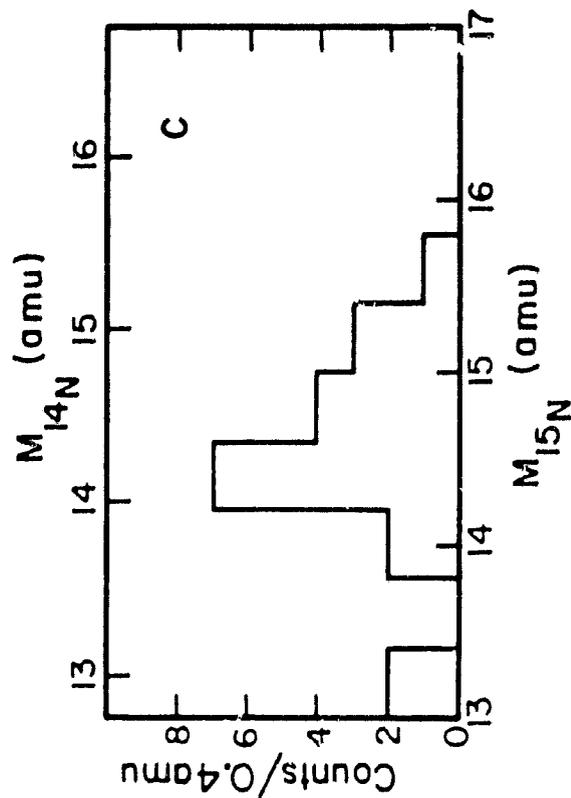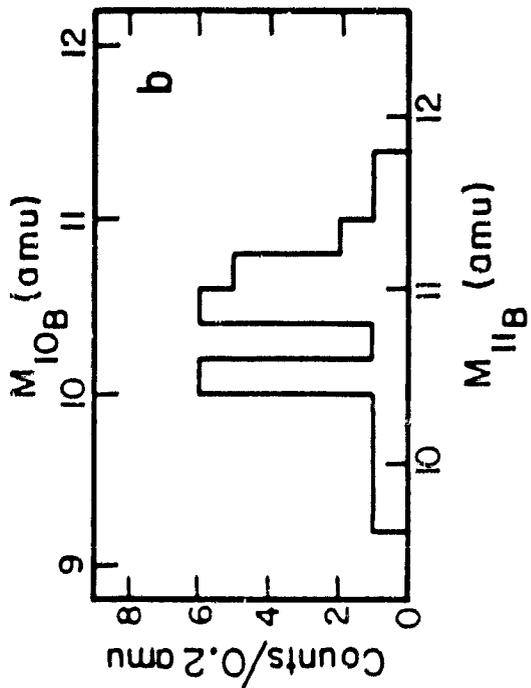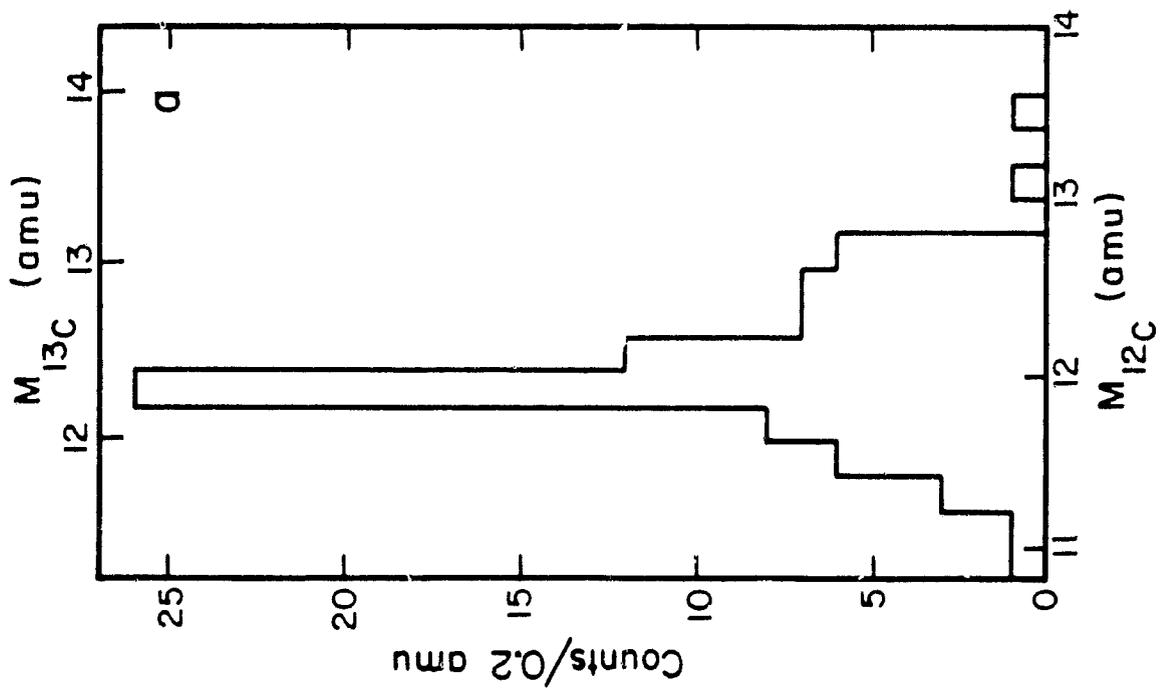
this because the difference between M_{10_B} and M_{11_B}, for example, is constant to within $\pm \sim 0.1$ amu.) The statistics and resolution for nitrogen are insufficient for the maximum likelihood method to deduce the offset of the mass scale, so we have not allowed m_1 to vary for that element. We thus rely on the fact that both theoretical calculations and measurements by other investigators (§4.3) indicate that our assignment of 14.5 amu as the mean mass in the determination of the nitrogen E/L function is correct. The masses for carbon in Figure 3.12 have been adjusted by only 0.02 pmu according to the maximum likelihood estimate of m_1; for boron there is no adjustment because the maximum likelihood estimate of m_1 is equal to the actual mass of ^{10}B, namely 9.94 pmu.

From Figure 3.12 we see that, although the statistics are limited, the mass resolution at boron is sufficient to validate our assumption of how the E/L function scales for different isotopes of the same element because the two peaks occur at the right mass values. That is, the lower mass peak occurs at 10 amu on the ^{10}B mass scale and the higher mass peak occurs at 11 amu on the ^{11}B mass scale. We also see in this figure that our mass resolution, and consequently the precision with which we can determine isotopic abundances, is degraded considerably as we go from boron to nitrogen.

3.5 Mass Resolution

The factors which contribute to the mass resolution in our instrument can be divided into two categories. The first consists of those processes which place a fundamental limit on the $\Delta E - E'$ technique

of resolving isotopes in that they cannot be reduced by increasing the precision of our measurements. Multiple Coulomb scattering (mcs) and statistical fluctuations in the ionization energy loss process ("Landau fluctuations") comprise this category. The second category consists of uncertainties in our measurements of particle trajectory and scintillation light. Decreasing these measurement errors will increase our mass resolution.

To evaluate the contribution of the various factors to the mass resolution we have used a Monte-Carlo technique which simulates multiple Coulomb scattering, Landau fluctuations, measurement of particle trajectory, spatial variations in light collection, and other miscellaneous effects. Events are generated with whichever of these processes we wish to include, and then analyzed for mass according to Equation 3.1. From the widths of the resulting mass distributions we determine the particular contribution to the mass resolution. We have taken D5+D6 as the ΔE-detector for boron and carbon, and D6 as the ΔE-detector for nitrogen (as in the analysis of flight data). For all elements we have taken D7 as the E'-detector. The event selection in the simulation is essentially identical to that used in the analysis of the flight data. The results are given in Table 3.2. A discussion of individual processes together with illustrative calculations based on Equation 2.4 follows.

In traversing a finite thickness of matter a charged particle undergoes many small deflections as it interacts with electrons in the matter. This multiple Coulomb scattering (Rossi 1952, Bischel 1972, Jackson 1975) means that a particle impinging on a detector at incident

Table 3.2 Contributions to Mass Resolution

Contributor	^{10}B	^{12}C	^{14}N
Multiple Coulomb Scattering	0.13 amu	0.14	0.18
Landau Fluctuations	0.08	0.09	0.12
Measured $\sec\vartheta$	0.02 (0.23)†	0.02 (0.28)	0.02 (0.34)
Light Collection	0.05 (0.18)	0.06 (0.21)	0.08 (0.27)
Photoelectron Statistics	0.05	0.06	0.07
Calibration Statistics	0.09	0.09	0.14
Monte Carlo Total	0.20 (0.32)	0.21 (0.38)	0.28 (0.46)
E/L Linear in L	0.05	0.07	0.11
No D7 Residual Map	0.16	0.19	0.28
Total	0.28 (0.36)	0.29 (0.42)	0.41 (0.55)
Achieved‡	0.32 ± 0.06	0.37 ± 0.04	0.50 ± 0.10

†Values in parentheses were calculated assuming a degraded resolution in MWPC X1 of $\sigma = 30$ mm (Appendix A).

‡From Table 3.1.

angle ϑ will generally emerge at some slightly different angle ϑ'. The mean square angle of scattering is given by (Bischel 1972)

$$\sigma_\vartheta^2 = <(\vartheta'-\vartheta)^2> = 1.78\times10^{-7}\,\mathrm{rad}^2\,\mathrm{cm}^2\,\mathrm{g}^{-1}\frac{Z^2\,Z_m(Z_m+1)\rho\,x\,B}{M^2\,A_m(\gamma\,\beta^2)^2} \qquad (3.6)$$

where

> Z = atomic number of particle,
> M = mass of particle (pmu),
> β = particle velocity (in units of the speed of light),
> $\gamma = (1-\beta^2)^{-0.5}$,
> Z_m, A_m = mean atomic number, weight of detector material,
> ρ = density of material (4.51 g cm^{-3} for CsI),
> x = thickness of material (cm),
> B = weak function of $Z_m, Z, \beta, \rho\,x$.

For particles and energies of interest in our experiment B is independent of β and is given by $B_{CsI} = 2.5\log_{10}(\rho\,x\,\mathrm{cm}^2\mathrm{g}^{-1}) + 12.4$. Equation 3.6 applies if the thickness of the material is such that the particle velocity does not change significantly in traversing the material, generally not the case in our experiment. We have derived (Appendix B) a formula based on Equation 3.6 which includes the fact that β is not constant; for $\rho\,x \approx 10\,\mathrm{g\,cm}^{-2}$ this represents about a 50% increase over Equation 3.6, because the term $\gamma^2\beta^4$ in the denominator decreases as the particle slows down in the material. Scattering by an amount σ_ϑ in the CsI above the ΔE-detector results in a pathlength uncertainty in that detector of

$\dfrac{\sigma_{\sec\vartheta}}{\sec\vartheta} = \dfrac{\tan\vartheta\,\sigma_\vartheta}{\sqrt{2}}$, whereas scattering by an amount σ_ϑ in the ΔE-detector results in a pathlength uncertainty of $\dfrac{\sigma_{\sec\vartheta}}{\sec\vartheta} = \dfrac{\tan\vartheta\,\sigma_\vartheta}{\sqrt{6}}$.

From Equation 2.4 we have

$$\frac{\sigma_{M,\sec\vartheta}}{M} = \frac{1}{M}\frac{\partial M}{\partial\sec\vartheta}\Big)_{E',\Delta E}\;\sigma_{\sec\vartheta} = \frac{1}{a-1}\frac{\sigma_{\sec\vartheta}}{\sec\vartheta}.$$

Typical rms scattering angles are $\sigma_\vartheta\approx 25\,\mathrm{mrad}$ in D0–D4, and $\sigma_\vartheta\approx 30\,\mathrm{mrad}$ in D5–D6, giving $\sigma_{M,mcs}\approx 0.14\,\mathrm{amu}$ for M=12 amu and $\vartheta=20°$,

consistent with the Monte–Carlo calculation. [Because D6 (and not D5+D6) was used as the ΔE–detector for nitrogen, entries in Table 3.1 for nitrogen are generally higher than those for boron or carbon.]

The second fundamental limit to our mass resolution is the statistical nature of the ionization energy loss process. These Landau fluctuations mean that a beam of monoenergetic particles of a given charge and mass incident on a thin detector will emerge with a distribution of energies, that is, they do not all lose the same amount of energy in the material. For particles and energies of interest in our experiment the distribution in energy deposited ΔE is a gaussian with variance (Jackson 1975)

$$\sigma^2_{\Delta E} = (0.396 \text{ MeV})^2 \text{cm}^2\text{g}^{-1} \, Z^2 \, \frac{Z_m}{A_m} \, \rho \, x \, \gamma^2 (1 - \frac{\beta^2}{2}) \, D^2 \tag{3.7}$$

where all quantities are defined as in Equation 3.6 except the "deceleration factor" D which takes into account the slowing down of the particle if x is sufficiently thick so that ΔE is not small compared to the particle's total energy. We have used a form for D derived by Wiedenbeck (1973) which ranges from unity at x/R=0 (R is the total range of the particle) to 2 at x/R=0.9. Landau fluctuations have the effect of moving events which are on a nominal isotope track (such as in Figure 3.1) off that track along a line of constant ΔE+E'. Equation 2.4 gives

$$\sigma_{M,Landau} = \frac{\partial M}{\partial \Delta E}\Big)_{E,\sec\theta} \, \sigma_{\Delta E} = \frac{a}{a-1} \, \frac{M}{E} \, \frac{(1-\frac{x}{R})^{1-\frac{1}{a}}}{\frac{x}{R}} \, \sigma_{\Delta E}.$$

A 200 MeV amu^{-1} ^{12}C nucleus incident on D5 has a range in CsI of 34.5 mm. With D5+D6 as the ΔE–detector x/R$\approx$0.58 for which D$\approx$1.2. From Equation 3.7 we calculate $\sigma_{\Delta E}=6.7$ MeV so that $\sigma_{M,Landau}\approx 0.10$ amu,

again in agreement with the Monte-Carlo calculation.

Errors associated with the finite precision with which we measure particle trajectory cause an uncertainty in the particle's i) angle of incidence, which in turn results in an additional (beyond multiple Coulomb scattering) uncertainty in the pathlength in the ΔE detector, and ii) absolute position at a scintillator, resulting in an uncertainty in the correction of scintillator output due to spatial variations in light collection. Contribution i) depends only on the spatial resolution of individual MWPC's, and for our geometry is given by $\frac{\sigma_{\sec\vartheta}}{\sec\vartheta} = 0.0016\,\text{mm}^{-1}\sin 2\vartheta\ \sigma_{MWPC}$ (Wiedenbeck 1978). For $\sigma_{MWPC} = 1\,\text{mm}$, $\vartheta = 20°$, and $M = 12\,\text{amu}$ we have

$$\sigma_{M,\sec\vartheta} = \frac{M}{a-1}\frac{\sigma_{\sec\vartheta}}{\sec\vartheta} \approx 0.02\,\text{amu}.$$

Contribution ii) depends additionally on the magnitude of the spatial gradients of the light collection variations (Table 2.1):

$$\sigma_{M,\Delta E} = \frac{\partial M}{\partial\Delta E}\Big)_{E',\sec\vartheta}\ \sigma_{\Delta E}$$

$$= M\frac{a}{a-1}\ \frac{1-(1-\frac{x}{R})^{\frac{1}{a}}}{\frac{x}{R}}\ \frac{\sigma_{\Delta E}}{\Delta E} \tag{3.8}.$$

With D5+D6 as the ΔE-detector, $0.15\%\,\text{mm}^{-1}$ gradients, $1\,\text{mm}$ MWPC resolution, $M = 12\,\text{amu}$, and $x/R=0.6$ we have $\sigma_{M,gradients} \approx 0.03\,\text{amu}$.

In our Monte-Carlo analysis we have evaluated these contributions to the mass resolution due to errors in trajectory measurement with two different assumptions of MWPC resolution. One, we assume all MWPC's measure particle position accurate to the nominal $\pm 1\,\text{mm}$ (the result is consistent with the rough calculation above). Two, we assume the

resolution of X1 is degraded, because of knock-on electrons, to ±30 mm, with all other MWPC's at the nominal value. The choice of 30 mm is somewhat arbitrary, as we do not know precisely what the effect of knock-on electrons will be on MWPC resolution for various particles and energies, but 30 mm is suggested based on our analyses of the y-trajectories (Appendix A). We choose X1 as the "bad" coordinate since events are not analyzed if X3 and X4 are inconsistent (X3 and X4 are separated in the vertical dimension by only 4.5 cm whereas we have no x-measurement at the top of our instrument other than X1). In Table 3.2 we have put in parentheses those contributions to mass resolution which have been evaluated assuming "bad" X1. We see the very significant effect that degradation of MWPC resolution in a single counter has on mass resolution.

There are a variety of other measurement errors which contribute to mass resolution that we have included in our Monte-Carlo simulation, which have been described in detail by Wiedenbeck (1978). They include photoelectron (pe) statistics, electronic noise, and uncertainties in in-flight calibrations. The error in ΔE due to photoelectron statistics is $\frac{\sigma_{\Delta E}}{\Delta E} = \frac{1}{\sqrt{150\,\mathrm{Mev}^{-1}\,\Delta E}}$. A typical ΔE in D5+D6 for ^{12}C is ~ 1 GeV. With $x/R \approx 0.6$, Equation 3.8 gives $\sigma_{pe} \approx 0.06$ amu. To estimate the error in mass due to the finite statistics for calibrations we quadrature the 0.15%, 0.25%, and 0.4% uncertainties from the Bevalac spatial response map, flight residual map, and PMT temperature correction, respectively (Chapter 2), to get $\approx 0.5\%$ uncertainty in both E_5 and E_6. With $\Delta E = E_5 + E_6$ and $E_6 \approx 2E_5$, we have $\frac{\sigma_{\Delta E}}{\Delta E})_{statistics} \approx 0.37\%$. Equation 3.8

then gives, for x/R=0.6, $\sigma_{M,statistics} \approx 0.08$ amu. Each of these rough calculations is consistent with the more precise Monte-Carlo results.

Three other effects which contribute to the mass resolution have not been included in the Monte-Carlo simulation; their magnitude has been evaluated instead by separate calculations and added in quadrature to the Monte-Carlo results to give the total expected mass resolution. The first of these is the possible error due to the assumption that E/L is linear in L. Its magnitude was estimated in §3.3 to be 0.05, 0.07, and 0.11 amu for boron, carbon, and nitrogen, respectively. Second is the error we make in treating scintillator thickness variations as a correction to ΔL independent of x/R (§2.2.3). If $\frac{\delta t}{t}$ is the percent correction which should have been made to t, but instead was made to ΔE, then the mass we calculate is in error by

$$\delta M = [\Delta E \frac{\partial M}{\partial \Delta E} - t\frac{\partial M}{\partial t}] \frac{\delta t}{t} \quad ,$$

$$\approx \frac{M}{a-1} \frac{\delta t}{t} [a\frac{1-(1-\frac{x}{R})^{\frac{1}{a}}}{\frac{x}{R}} - 1].$$

It is because the term in brackets varies with x/R that our treatment of thickness variations is not precise. That term, however, has an rms variation of only ~ 0.11 for $0.4 \leq \frac{x}{R} \leq 0.9$. From Table 2.1 $\frac{\delta t}{t}$ is $\approx$ 0.6% for nitrogen, and slightly smaller for boron and carbon (assuming thickness variations in D5 and D6 are uncorrelated). Thus our thickness error is < 0.01 amu, and is therefore negligible. Finally, if the assumption that there is no spatial variation in the output of detector D7 beyond that measured at the Bevalac (§2.2.3) is false, then part of the residual spatial

variation assigned to the output of detectors D5 and D6 should in fact have been assigned to D7. The error in mass which results has two components whose effects add [this is because the calibration function $f_6(\sec\vartheta, D_7)$ for penetrating oxygen has $\dfrac{\partial f_6}{\partial D_7} \approx 1$, whereas the mass tracks (Figure 3.1) have $\dfrac{\partial E_6}{\partial E_7} < 0$]. The uncorrected mass for a· event at a particular position is

$$M = M_0 + r\,s\,E'\frac{\partial M}{\partial E'} - (1-r)\,s\,\sqrt{0.55}\,\Delta E\frac{\partial M}{\partial \Delta E} \quad .$$

where $M_0 =$ actual mass of particle, $r =$ fraction of the measured residual variation due to D7, and $s =$ magnitude (%) of the residual variation (1.9% rms, Table 2.1). The factor under the square root comes from the assumption that $E_6 \approx 2E_5$ and uncorrelated variations in signals D_5 and D_6 (this factor is unity for nitrogen where D_5 is not used). The (false) correction we apply is $\sqrt{0.55}\,s\,\Delta E \dfrac{\partial M}{\partial \Delta E}$ so that the error is

$$\delta M = r\,s\left(E'\frac{\partial M}{\partial E'} + \sqrt{0.55}\,\Delta E\frac{\partial M}{\partial \Delta E}\right)$$

$$\approx \frac{a\,M\,r\,s}{(a-1)\frac{x}{R}}\left[\left(1-\frac{x}{R}\right)^{\frac{1}{a}} - 1 + \frac{x}{R} + \sqrt{0.55}\left[1 - \left(1-\frac{x}{R}\right)^{\frac{1}{a}}\right]\right].$$

We estimate r from Table 2.1 by assuming that the magnitude of the residual variation is proportional to that of the Bevalac variation, so that $\dfrac{1-r}{r} = \dfrac{5.7}{4.2}$, or $r \approx 0.42$. For boron and carbon we thus have (averaged over $0.55 \leq \frac{x}{R} \leq 0.90$) $\delta M \approx 0.16$ and 0.19 amu, respectively. For nitrogen, $\delta M \approx 0.28$ amu ($\sqrt{0.55} \to 1$, so that δM is independent of x/R).

From Table 3.2 we see that the achieved mass resolution for all elements is bracketed by the calculation in which we assume nominal

MWPC X1 resolution and that in which we assume degraded MWPC X1 resolution. From the table it is also evident that there is a fundamental limitation to mass resolution because of multiple Coulomb scattering and Landau fluctuations of 0.15 tc 0.22 amu which would dominate the total mass resolution if the MWPC resolution were the nominal ± 1 mm and there were no uncertainties in residual spatial variation. Improved MWPC resolution would obviously be desirable for all charges, as would an independent calibration of possible residual spatial variations in detector D7. Other improvements in mass resolution could be obtained by using a detector material with a smaller Z_m than CsI to decrease the Coulomb scattering (Equation 3.6, although this could adversely affect other features; for example, there would be more nuclear interactions in the detectors), and improved statistics for in-flight calibrations.

Chapter 4

Interpretations of Measurements

Having measured the isotopic compositions of boron, carbon, and nitrogen, we next interpret the measurements in light of those processes—nucleosynthesis, galactic propagation, and solar modulation—by which they are determined. Before doing this, however, we must correct the measurements for the contamination introduced by the $5\,\mathrm{g\,cm^{-2}}$ of atmosphere under which our experiment flew, as well as possible contamination due to the presence of the $\sim 10\ \mathrm{g\,cm^{-2}}$ of CsI (D0–D4) above our mass measurements at D5 (or D6 for nitrogen).

4.1 Detector Interactions

Our charge-consistency requirement (§3.2) eliminates most nuclear interactions in the CsI itself. It is possible, however, that neutron stripping reactions take place in the CsI above D5, altering the isotopic composition of a given element from its value at the top of the instrument. Based on the work of Lindstrom et al. (1975) we estimate that about 4% of the total inelastic cross section for a given particle in some medium can be ascribed to single neutron stripping. For the total inelastic cross section of a particle of mass number A_i in a medium of mass number A we use

$$\sigma_1 = 52.28\,\mathrm{mb}\ [A^{\frac{1}{3}} + A_i^{\frac{1}{3}} - b\ ]^2 \qquad (4.1)$$

where the overlap parameter is $b = 1.189\,\exp[-0.05446\,\min(A,A_i)]$ [Hagen et al. 1977; note, however, that b in this reference is given incorrectly as one minus the correct b used here (Ormes 1981)]. With $A \approx 130$ for CsI we thus calculate, for example, that $< 0.5\%$ of ^{15}N will be

transformed into ^{14}N in $10\,g\,cm^{-2}$. We have therefore made no correction to the measured isotopic compositions for this effect

Because elemental abundances at the top of the instrument will be required for the atmospheric correction, we first use Figure 3.5c as a measure of the elemental abundances of particles which have undergone no charge-changing nuclear interaction before stopping in D7. The abundance at the top of the instrument for a given species is larger by a factor $\exp(0.96\,n\,\sigma_i x)$, where $n=$ number density of nuclei in CsI and $x=$ mean total thickness of CsI traversed for particles which stop in D7 $\approx 52\,mm$ (the factor 0.96 is included assuming 4% of σ_i is due to neutron stripping). We list in Table 4.1 the measured elemental abundances from Figure 3.5c, the correction factors $\exp(0.96\,n\,\sigma_i x)$, and the corrected elemental abundances at the top of the instrument. The fourth column gives the elemental abundances corrected for atmospheric secondaries and energy interval differences (see following section), normalized to carbon. A comparison with another recent balloon measurement in the fifth column (Lund et $al.$ 1975) shows good agreement.

4.2 Atmospheric Correction

Based on independent measurements by our own pressure-transducers and those of the launch support group, the mean atmospheric depth at which the instrument flew was $4.7 \pm 0.2\,g\,cm^{-2}$; the rms temporal variation in depth over the period during which data were taken was $\sim 0.6\,g\,cm^{-2}$. Because the atmospheric correction to our measurements turns out to be quite small, temporal variations in depth

Table 4.1 Elemental Abundances

	Observed	Detector Interactions	Top of Instrument	†Top of Atmosphere	Lund et al (1975)
Boron	82 ± 8	1.27	79 ± 10	31 ± 4	32 ± 3
Carbon	214 ± 15	1.28	274 ± 19	100	100
Nitrogen	75 ± 9	1.30	98 ± 11	33 ± 4	28 ± 2
Oxygen	185 ± 14	1.32	243 ± 18	82 ± 8	90 ± 3

†Corrected for atmospheric secondaries and different energy intervals (§4.2), normalized to carbon.

as well as the uncertainty in the mean depth have been neglected, and we have simply treated the atmosphere as a 5 g cm^{-2} thick slab (includes a mean secant of 1.07) through which all particles must travel before encountering the instrument.

The abundances at a given atmospheric depth and energy per nucleon interval differ from those at the top of the atmosphere because of nuclear fragmentation and ionization energy loss. If $f_i(x, \varepsilon_{i1}, \varepsilon_{i2})$ is the flux at depth x (g cm^{-2}) of species i [atomic number Z_i, mass M_i (pmu)] with energy per nucleon (MeV pmu^{-1}) between ε_{i1} and ε_{i2}, then the flux at depth $x + \delta x$ is

$$f_i(x+\delta x, \varepsilon_{i1}, \varepsilon_{i2}) = \exp(-n\sigma_i \delta x) f_i(x, \varepsilon'_{i1}, \varepsilon'_{i2})$$
$$+ \sum_{k>i} [1 - \exp(-n\sigma_{ik}\delta x)] \, f_k(x, \varepsilon_{ik1}, \varepsilon_{ik2}) \tag{4.2}$$

where $n =$ number of target (atmospheric) nuclei per gram of atmosphere, $\sigma_i =$ total inelastic cross section of species i in the atmosphere (Equation 4.1), and $\sigma_{ik} =$ partial cross section for species k to produce species i in the atmosphere. We have made the approximation that δx is sufficiently small that one can neglect tertiary and higher order fragmentations. The energy intervals are related by

$$R_{air}(\varepsilon'_{i1}) = R_{air}(\varepsilon_{i1}) + \frac{Z_i^2}{M_i} \delta x, \quad \text{and} \quad R_{air}(\varepsilon_{ik1}) = R_{air}(\varepsilon_{i1}) + \left(\frac{Z_i^2}{M_i} + \frac{Z_k^2}{M_k}\right)\frac{\delta x}{2} \quad \text{with}$$

similar equations relating ε'_{i2} and ε_{ik2} to ε_{i2}. $R_{air}(\varepsilon)$ is the range in air (g cm^{-2}) of a proton of kinetic energy ε. We have assumed that fragmentations of species k occur at $x + \frac{\delta x}{2}$.

We have developed a computer program based on Equation 4.2 which takes, as input, abundances and energy spectra of nuclear species

at the top of the atmosphere and propagates these abundances in $1\,\mathrm{g\,cm^{-2}}$ steps into the atmosphere. For the partial cross sections σ_{lk} we have used the semi-empirical proton-nucleus cross sections and scaling nucleus-nucleus cross sections of Silberberg and Taso (1973a, 1973b, 1977a, 1977b, 1977c). (The energy dependences of the nucleus-nucleus cross sections are not well known; we have used the asymptotic high energy values which are applicable down to at least $600\,\mathrm{MeV\,pmu^{-1}}$.) We have used the tabulation by Barkas and Berger (1964) for the function R_{air}. As input to the program we have used the satellite measurements of Garcia-Munoz and Simpson (1979) for the elemental abundances of species with $Z > 8$, and the calculation by Wiedenbeck (1978) for the corresponding isotopic abundances. We have assumed that all species have the same energy spectra which we take to be that measured by Garcia-Munoz et al. (1977b) corrected to the level of solar modulation appropriate to August 1978 (Appendix C; specifically, we have assumed that $df/d\varepsilon = k\,\varepsilon^a$ with $a = 0.57$ for $\varepsilon < 220\,\mathrm{MeV\,pmu^{-1}}$ and $a = -0.46$ for $\varepsilon > 220\,\mathrm{MeV\,pmu^{-1}}$). We have adjusted the elemental abundances of B, C, N, and O and the isotopic abundances of B, C, and N (we have assumed that our observed O is all $^{16}\mathrm{O}$) at the top of the atmosphere until the abundances at $5\,\mathrm{g\,cm^{-2}}$ are consistent with our measured elemental abundances (third column, Table 4.1) and isotopic composition (Table 3.1).

We show in Table 4.2 the fraction of the abundance of a given nuclide at $5\,\mathrm{g\,cm^{-2}}$ atmospheric depth due to the various contributing species at the top of the atmosphere. For example, 87.6% of $^{10}\mathrm{B}$ at $5\,\mathrm{g\,cm^{-2}}$ comes from $^{10}\mathrm{B}$ at the top of the atmosphere which undergo no

Table 4.2 Contributions to the Observed Abundances (Percent)

Observed Nuclide	Source Nuclide							
	^{10}B	^{11}B	^{12}C	^{13}C	^{14}N	^{15}N	^{16}O	$Z > 8$
^{10}B	87.5	1.8	5.4	0.2	1.1	0.4	2.5	1.4
^{11}B		90.4	4.9	0.2	0.5	0.5	2.2	1.3
^{12}C			98.0	0.1	0.3	0.1	1.2	0.3
^{13}C				86.3	1.3	1.8	7.7	3.0
^{14}N					93.7	0.8	4.6	0.9
^{15}N						91.3	7.4	1.3

nuclear interaction, 1.6% of ^{10}B results from ^{11}B nuclei which are stripped of a single neutron in 5 g cm^{-2} of atmosphere, and so on. That no more than 15% of the observed abundance of any of the nuclides in Table 4.2 is due to fragmentation of heavier species suggests that our assumptions about the isotopic composition of species with $Z \gtrsim 8$ and the energy spectra of all species are relatively unimportant in making the atmospheric correction.

We summarize in Table 4.3 the results of the atmospheric correction. The first column indicates the energy interval at the top of the instrument over which HEIST is sensitive to the given nuclide. The lower limit corresponds to the requirement that $L_7 > 11$ nlu (see Figure 3.2b), the upper limit results from the restriction that the vertical projection of the range in detector D7 must be less than the thickness of D7 (17 mm). The second column, from Table 3.1, gives the measured isotopic abundances. The third column indicates the amount by which an abundance at the top of the instrument must be increased to obtain its abundance at the top of the atmosphere. The fourth column gives the energy interval at the top of the atmosphere, and finally, in the fifth column, we tabulate the isotopic abundances corrected for both atmospheric interactions and the fact that the energy per nucleon intervals for isotopes of a given element are of slightly different width. The overlap of the energy intervals is such that the fractional isotopic abundances vary by only ~ 0.01 as the assumed form of the spectrum varies from $\varepsilon^{-0.5}$ to $\varepsilon^{+0.5}$; in Table 4.3 we have simply assumed that the number of events is proportional to the width of the energy window, that is, a flat energy spectrum.

Table 4.3 Measured and Corrected Abundances

	Top of Instrument		Atmospheric(3) Correction	Top of Atmosphere	
	ϵ Interval(1) (MeV/pmu)	Isotopic(2) Composition		ϵ Interval(1) (MeV/pmu)	Isotopic(4) Composition
Boron		$^{10}\text{B/B} = 0.38^{+0.18}_{-0.18}$			$^{10}\text{B/B} = 0.33^{+0.17}_{-0.17}$
^{10}B	218.4–254.3		1.03	284.4–300.0	
^{11}B	205.8–238.7		1.08	248.9–281.8	
Carbon		$^{13}\text{C/C} = 0.08^{+0.13}_{-0.03}$			$^{13}\text{C/C} = 0.08^{+0.13}_{-0.03}$
^{12}C	240.5–283.1		1.18	292.7–334.8	
^{13}C	229.2–269.7		1.05	278.7–318.3	
Nitrogen		$^{15}\text{N/N} = 0.42^{+0.19}_{-0.17}$			$^{15}\text{N/N} = 0.42^{+0.19}_{-0.17}$
^{14}N	261.8–310.4		1.15	319.8–367.1	
^{15}N	251.1–297.9		1.12	306.5–352.0	

Notes:
(1) 80% of the particles lie within the given range.
(2) From Table 3.1.
(3) Factor by which abundance at top of instrument of the given nuclide must be multiplied to obtain its abundance at top of atmosphere.
(4) Corrected for different ϵ intervals, assumes flat spectrum.

4.3 Comparisons with Other Measurements

We show in Figure 4.1 our corrected results for the isotopic compositions of boron, carbon, and nitrogen, together with those of other investigators. Tabulated in Table 4.4 are the mass resolutions achieved by this work and others. Our mass resolution at boron is the best of those tabulated. At carbon and nitrogen our resolution is comparable to or better than others', except for the exceptionally high resolution achieved by Wiedenbeck et al. (19). Our relatively large uncertainties in the determination of fractional isotopic abundances are due almost entirely to limited statistics. Because of the excellent agreement between predicted and achieved resolution (Table 3.2), we feel confident that systematic effects have been properly identified and accounted for.

Also shown in Figure 4.1 are smooth curves which represent the predictions of a model whose characteristics we now describe.

4.4 Theory

The cosmic ray abundances observed at earth differ from those at the cosmic ray source for two reasons. One, the particles traverse, on the average, ~5-6 g cm^{-2} of interstellar matter before being observed in the solar system, and are thus subject to nuclear fragmentation and ionization energy loss. Thus observations of the elements Li, Be, and B, which are bypassed in the normal processes of nucleosynthesis and are presumed to be absent at the cosmic ray source, are explainable entirely in terms of the spallation of heavier species. Second, as the cosmic rays

Figure 4.1

Comparisons of measurements. ○: this work. □: Garcia–Munoz *et al.* 1977a, Guzig 1980. ✕: Wiedenbeck *et al.* 1979. △: Hagen *et al.* 1977. ▽: Buffington *et al.* 1978. ◇: Webber and Kish 1979, Webber *et al.* 1979. The dashed curves correspond to a galactic propagation model with no solar modulation. The solid curves correspond to a level of modulation $\Phi = 300$ MeV amu^{-1} for particles with $M/Z = 2$.
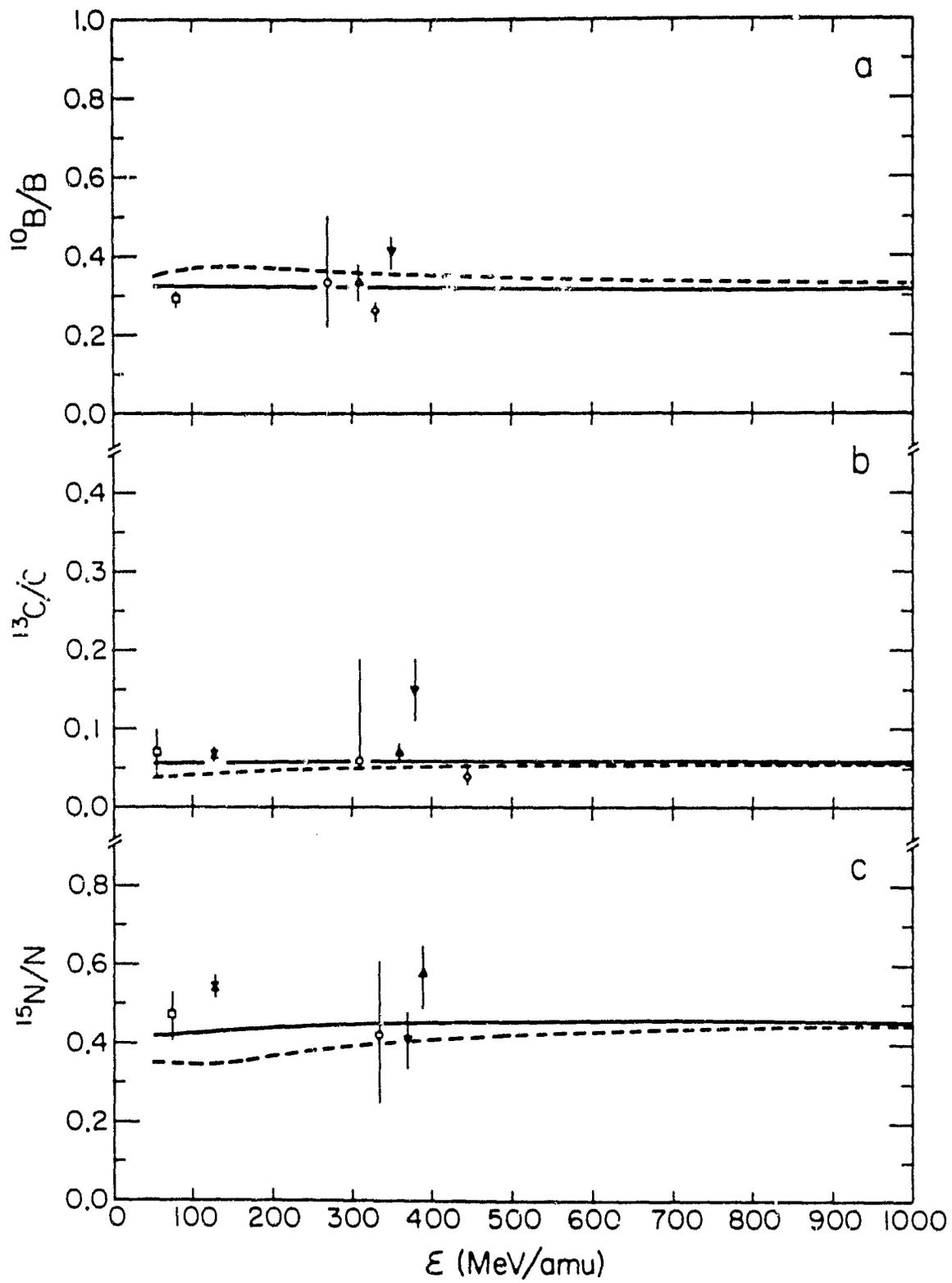
Table 4.4 Comparisons of Mass Resolutions

	Boron	Carbon	Nitrogen
This work	0.32 amu	0.37	0.50
GSFC (1)	0.50	0.58	0.68
UC Berkeley (2)		0.17	~0.20
U. Chicago (3)	~0.4	0.38	0.44
UNH (4)	0.35	0.29	0.32
UC Berkeley (5)	~0.4	~0.5	~0.5

Notes:
(1)Hagen *et al.* 1977.
(2)Wiedenbeck *et al.* 1979.
(3)Garcia-Munoz *et al.* 1977a, Guzig 1980.
(4)Webber and Kish 1979, Webber *et al.* 1979.
(5)Buffington *et al.* 1978.

enter the solar cavity, they suffer energy loss as they interact with the small-scale irregularities of the interplanetary magnetic field which is carrried radially outward from the sun by the expanding solar wind. One must therefore account for the rigidity-dependent effects of this process before interpretation of observed abundances is possible.

4.4.1 Galactic Propagation

If $n_i(\vec{x},t,\varepsilon)d\varepsilon$ is the number density of particles of type i at position $\vec{x}$ and time t with energy per nucleon between ε and $\varepsilon+d\varepsilon$, then the continuity equation which describes cosmic ray transport in the galaxy is (e.g. Reames 1974)

$$\frac{\partial n_i}{\partial t} = \nabla\cdot(\kappa_i\nabla n_i) + \frac{\partial}{\partial\varepsilon}\big[\big(\frac{d\varepsilon}{dt}\big)_i n_i\big] - \frac{n_i}{\tau_i} + q_i + \sum_{j>i}\frac{n_j}{\tau_{ij}} \tag{4.3}.$$

The first term on the right is the divergence of a diffusion current $\kappa_i\nabla n_i$, which is due to spatial gradients in n_i; κ_i is the diffusion coefficient. The next term is a "divergence" in energy-space, and accounts for changes in n_i due to ionization energy loss. We lump into the term $-n_i/\tau_i$ all "catastrophic" losses, such as nuclear destruction and escape from a confinement volume; the mean time for such a loss is τ_i. Finally, there are two source terms, the production q_i of particles at the cosmic ray source, and the contribution from heavier species j which fragment with mean time τ_{ij} into species i.

The usual approximations which go into simplifying Equation 4.3 are i) steady-state equilibrium ($\partial n_i/\partial t = 0$), and ii) homogeneous distributions of the n_i ($\nabla n_i = 0$). It is convenient to consider pathlengths Λ (g cm^{-2}) rather than times τ [related by $\Lambda = \rho\beta c\tau$ with ρ = density (g cm^{-3}) of interstellar gas], and fluxes J rather than densities n

$(J = n\beta c/4\pi)$. Equation 4.3 becomes

$$\frac{J_i}{\Lambda_i} = \frac{Z_i^2}{M_i}\frac{d}{d\varepsilon}[S(\varepsilon)\,J_i] + Q_i + \sum_{j>i}\frac{J_j}{\Lambda_{ij}} \tag{4.4}$$

where J_i = flux of species i in local interstellar space, Z_i, M_i = charge, mass of species i, Λ_i = mean free path for catastrophic losses of species i, Λ_{ij} = mean free path for species j to fragment into species i, and $S(\varepsilon)$ = specific ionization (MeV cm^2 g^{-1}) of a proton of energy ε in interstellar space. Q_i is proportional to the source production of species i per gram of interstellar matter. The solution to Equation 4.4 requires the specification of boundary conditions. In the currently popular "Leaky Box" model (Cowsik et al. 1967), the galaxy is envisioned as a confinement volume whose boundaries are encountered many times by the cosmic rays before they escape, implying an exponential distribution of pathlengths with mean Λ_e. The solution to Equation 4.4 is then (Reames 1974, Meneguzzi et al. 1971)

$$J_i(\varepsilon) = \int_0^\infty dx \frac{S(\varepsilon')}{S(\varepsilon)}\exp-\left(\frac{x}{\Lambda_i}\right)\left[Q_i(\varepsilon') + \sum_{j>i}\frac{J_j(\varepsilon')}{\Lambda_{ij}(\varepsilon')}\right] \tag{4.5}$$

where ε' is related to ε through the integration variable x, $\int_\varepsilon^{\varepsilon'}\frac{d\varepsilon}{S(\varepsilon)} = \frac{Z_i^2 x}{M_i}$.

The mean free path for losses is related to Λ_e through $\frac{1}{\Lambda_i} = \frac{1}{\Lambda_e} + \frac{1}{\Lambda_{id}}$ where Λ_{id} is the mean free path for nuclear destruction of species i. Equation 4.4 thus allows, for a given set of source abundances and energy spectra [embodied in the $Q_i(\varepsilon)$], the propagation of those abundances and spectra to give the fluxes J_i in local interstellar space, assuming that the Λ_{ij} (which are related to the cross sections σ_{ij}) are known.

4.4.2 Solar Modulation

Fluxes in local interstellar space differ from those observed at the orbit of earth because of the influence of the expanding solar wind to which is tied an interplanetary magnetic field. The effects of convection and diffusion are embodied in a spherically symmetric Fokker–Planck equation (Fisk 1974)

$$\frac{1}{r^2}\frac{\partial}{\partial r}\left[r^2\left(V_{sw}n-\kappa\frac{\partial n}{\partial r}\right)\right] = \frac{1}{3r^2}\frac{\partial}{\partial r}\left(r^2V_{sw}\right)\frac{\partial}{\partial T}\left(\alpha T n\right) \tag{4.6}$$

where $n(r)$ = number density of particles per unit kinetic energy interval at distance r from the sun, V_{sw} = solar wind velocity $\approx 400\,\mathrm{km\,sec^{-1}}$, κ = diffusion coefficient, T = kinetic energy, and $\alpha = (T+2E_0)/(T+E_0)$, with E_0 being the rest energy of the species of interest. The solution of Equation 4.6 predicts, for a given local interstellar spectrum and diffusion coefficient, the modulated spectrum at $r = 1\,\mathrm{AU}$. It is convenient to characterize the level of modulation by a parameter Φ, which represents the mean change in energy per nucleon from outside the solar cavity to 1 AU (Gleeson and Axford 1968): $\Phi \approx \frac{\alpha T}{3M}\int_{1\,AU}^{R}dr\frac{V_{sw}}{\kappa}$, where $R \approx 50\,\mathrm{AU}$ is the distance beyond which solar modulation is negligible. The diffusion coefficient κ is typically taken to be proportional to velocity times a function of the particle's magnetic rigidity, $P = \gamma\beta E_0/eZ$ (Fisk 1974, Lezniak and Webber 1971). A particularly simple form is $\kappa \propto \beta P$, in which case Φ is independent of energy and proportional to the particle's charge to mass ratio. For the period 1974–1976, Garcia–Munoz et al. (1977a) show that $\Phi \approx 220\,\mathrm{MeV\,amu^{-1}}$. Wiedenbeck and Greiner (1980) take $\Phi = 325\,\mathrm{MeV\,amu^{-1}}$ for the period August 1978 through August 1979 to account for an increase in solar activity. As our

measurements were made in August 1978, we estimate $\Phi \approx 300\,\text{MeV am}_{...}^{-1}$.

It should be emphasized that Φ represents the *average* energy loss, and does not apply to individual particles. Urch and Gleeson (1973) have calculated the distributions of energies outside the solar cavity from which came particles with some fixed energy at 1 AU. We show in Table 4.5, based on their work, the energy intervals in interstellar space corresponding to the FWHM of the distribution, for our own measurements as well as the satellite measurements by the University of Chicago group ($\square$ in Figure 4.1, Garcia–Munoz *et al.* 1977a, Guzig 1980), and the UC Berkeley group (X in Figure 4.1, Wiedenbeck *et al.* 1979).

4.4.3 Model Calculations and Discussion

The models of galactic propagation and solar modulation described above have been used to predict the observed isotopic abundances of B, C, and N at 1 AU. (We are indebted to M. Wiedenbeck for supplying the computer–generated results of the calculation which we quote here. See Wiedenbeck and Greiner 1980, and references therein, for a further discussion of the model used.) The elemental composition of the source is taken to be that calculated by Silberberg *et al.* (1976). The isotopic composition is assumed to be that of the solar system (Cameron 1973), except in the case of the element Ne, for which recent measurements (Greiner *et al.* 1979, Mewaldt *et al.* 1980) indicate an abundance of ^{22}Ne enhanced over the solar system value. A source spectrum of the form $(\varepsilon + 400\,\text{MeV amu}^{-1})^{-2.6}$ (Garcia–Munoz *et al.* 1977a) is used, and partial cross sections are those of Silberberg and

Table 4.5 Energy Intervals in Interstellar Space

	Φ	Boron		Carbon		Nitrogen	
		ε_{1AU}	ε_{IS}	ε_{1AU}	ε_{IS}	ε_{1AU}	ε_{IS}
U. Chicago(1)	220	80	195–405	55	170–380	75	190–406
UC Berkeley(2)	325			130	325–585	130	325–585
This work	300	270	445–895	310	485–735	340	515–785

Notes:
(1)Garcia–Munoz et al. 1977a, Guzig 1980.
(2)Wiedenbeck and Greiner 1980, Wiedenbeck et al. 1979. Φ is the level of modulation appropriate to each measurement. ε_{1AU} gives All energies in MeV am.1^-1. Φ is the level of modulation appropriate to each measurement. ε_{1AU} gives the energy at which observations at 1 AU are made, and ε_{IS} gives the corresponding interval in interstellar space

Tsao (1973a, 1973b, 1977a, 1977b). The interstellar gas is presumed to contain one He atom for every ten H atoms; the H density is taken to be 0.3 cm^{-3}. The mean escape pathlength is taken to be $\Lambda_e = 5.5\,\mathrm{g\,cm^{-2}}$ (Ormes and Freier 1978).

We show in Figure 4.1 (together with the experimental points) the results of the calculation. The solid curves correspond to a level of solar modulation $\Phi = 300\,\mathrm{MeV\,amu^{-1}}$, the dashed curves correspond to no modulation (local interstellar space). Some qualitative features are readily apparent. The very slight energy dependence in each of the unmodulated curves is almost completely washed out by solar modulation, the first-order effect of which is to increase the fractional abundance of the heavier isotope at 1 AU. This is due to the fact that Φ is slightly larger for the lighter isotope, and local interstellar abundances decrease with energy. Second, quite apart from the predictions of the model, the data are consistent with a constant fractional isotopic abundance, independent of energy, for each of the elements. (Disagreements between individual measurements, which are apparently statistically significant, might in fact be due simply to an underestimate of the errors.)

Ideally one would like to use plots such as this to place constraints on certain parameters of the model, although it is clear from the size of our error bars that stringent limits would not likely result from our measurements alone. Instead we discuss, in the context of the data as a whole, the degree to which interpretations of these data are limited, both because of measurement errors and model inadequacies.

Because the predictions of the model depend critically on the cross sections used in calculating the secondary component of the observed flux (the term $\sum_{j>i} \frac{J_j}{\Lambda_{ij}}$ in Equation 4.5), we show in Figure 4.2 the semi-empirical values of the most important cross sections as a function of energy. [By a cross section such as σ ($^{16}O+p\to{}^{15}N$) we really mean the sum of the cross sections σ ($^{16}O+p\to{}^{15}N$) and σ ($^{16}O+p\to{}^{15}O$), because ^{15}O β^+ decays almost immediately to ^{15}N.] Also shown are the energy intervals in interstellar space (Table 4.5) appropriate to the satellite measurements by the University of Chicago group (Garcia-Munoz et al. 1977a, Guzig 1980), the UC Berkeley group (Wiedenbeck et al. 1979), and this work. The onset of a significant energy dependence to the cross sections below ~ 400 MeV amu^{-1} means that solar modulation effects become more significant for the low energy measurements (as is seen in the shape of the dashed curves in Figure 4.1). More important, most of these cross sections have not been measured at low energies, and the form of their energy dependence can only be inferred from other measured cross sections, the nuclear physics of which is expected to be similar (we shall quantify this somewhat in the discussion of nitrogen below). With these limitations in mind, then, we discuss what one can conclude from the measurements.

Because boron is produced entirely by the breakup of heavier species in the interstellar medium, the locations of the curves in Figure 4.1a are, to first order, dependent only on the ratio of the relevant cross sections for producing ^{10}B and ^{11}B. For both species, oxygen and carbon are the major contributors, accounting for more than half of the observed boron. That ^{11}B dominates is due in part to

Figure 4.2

Semi—empirical cross sections (Silberberg and Tsao 1973a, 1973b, 1977a, 1977b).

a) Cross sections for ^{16}O on protons to produce the indicated products.

b) Cross sections for ^{12}C on protons to produce the indicated products.

If the interaction can proceed by way of an intermediate short—lived radioactive nuclide which decays to the indicated product, the corresponding cross section is included. The horizontal bands correspond to the energy intervals in local interstellar space appropriate to measurements by the University of Chicago group (Garcia—Munoz *et al.* 1977a, Guzig 1980), the UC Berkeley group (Wiedenbeck *et al.* 1979), and this work.
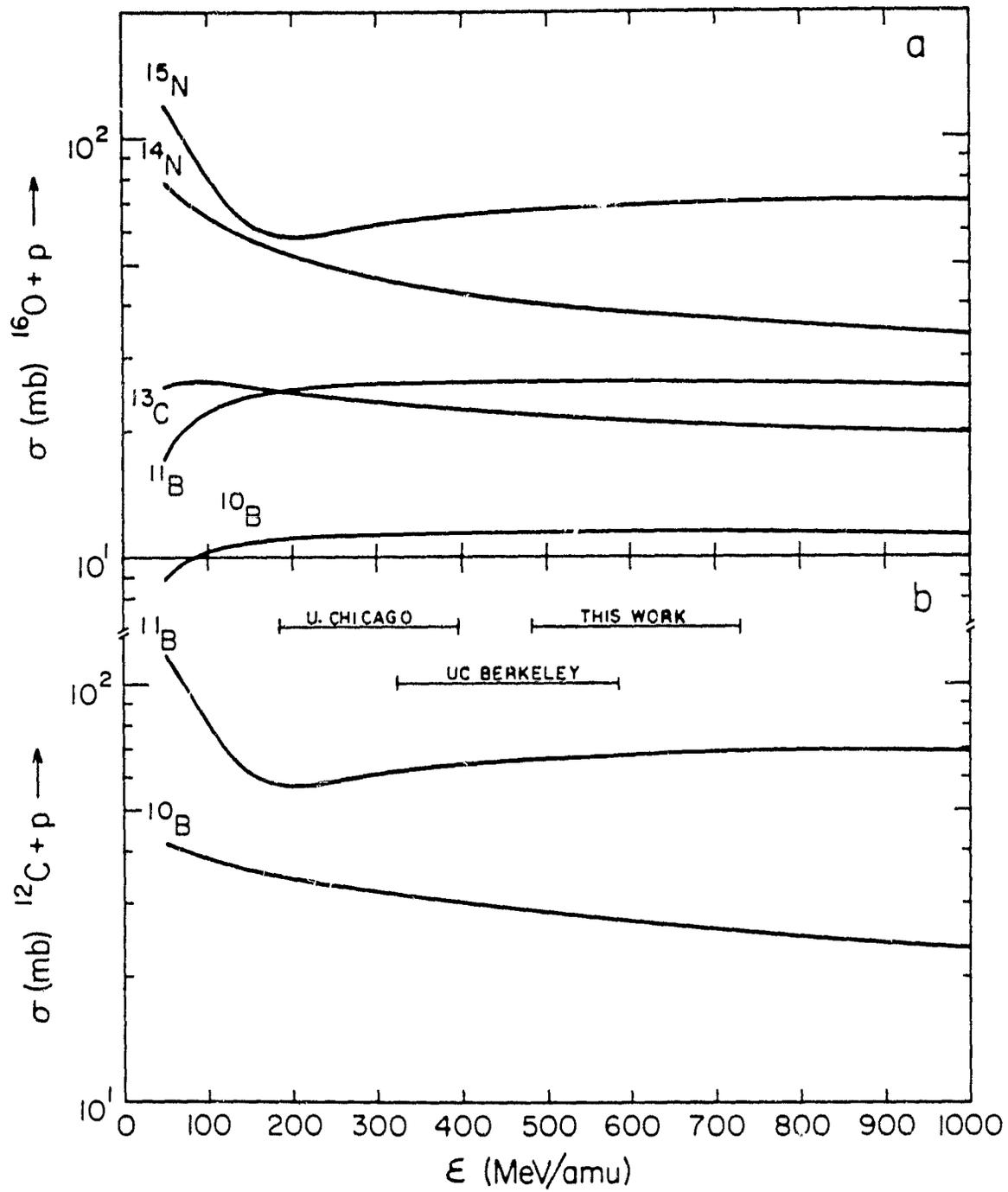
the contribution from the reaction $^{12}C(p,np)^{11}C$; ^{11}C subsequently β^+ decays to ^{11}B. We take Figure 4.1a as an indication that the ratios of the cross sections for producing ^{10}B and ^{11}B are adequately described by the semi-empirical formulae, and show little energy dependence, at least above ~400 MeV amu^{-1}.

Turning next to carbon (Figure 4.1b), we see that a solar-like composition ($^{13}C/C = 0.011$) for the cosmic ray source is consistent with the measurements. If our model of galactic propagation is substantially correct, a precise determination of the ^{13}C source abundance is obscured by the large (> 80%) secondary contribution to the observed flux. The measurements do rule out a hot (T> 10^8 °K) equilibrium CNO bi-cycle as a major contributor to the carbon abundances, as pointed out by Guzig (1980), as in that case one would expect a ratio $^{13}C/C$ approaching 0.2.

The nitrogen measurements (Figure 4.1c) are the most indicative of some disagreement with the predictions of the model, at least at satellite energies. In order to avoid requiring a source ratio of $^{15}N/N$ which is significantly greater than the solar system value of 0.0036, Guzig (1980) has used an alternate set of cross sections for the reactions $^{16}O+p \to ^{15}N$ and $^{16}O+p \to ^{14}N$, which are scaled from measured cross sections of $^{12}C+p \to ^{11}B$ and $^{12}C+p \to ^{10}B$. Using this alternate set as an indication of the sensitivity of the model predictions to uncertainties in cross sections, we find that the unmodulated value of $^{15}N/N$ (dashed curve, Figure 4.1c) increases by ~18%, 10%, and 4%, at interstellar energies (Table 4.5) appropriate to the measurements by the U. Chicago group, the UC Berkeley group, and this work, respectively. This implies

an increase in the predicted modulated value of $^{15}N/N$ by ~ 0.07, 0.04, and 0.02. At satellite energies, then, the predictions of the model are uncertain at the same level as uncertainties in the measurements, even if one considers cross section errors alone. Finally, we find that a weighted average of the difference between measured and predicted $^{15}N/N$ for these three measurements is 0.06 ± 0.04, where the error includes both cross section uncertainties and measurement uncertainties, the former as given above. We note that modest increases in solar modulation, and, to a lesser extent in the value of Λ_e, would further close the gap between predicted and measured values of $^{15}N/N$, especially at low energies. We conclude that the source abundance of ^{15}N is marginally consistent with the solar system value.

In conclusion we point out that, although at present there is no evidence that the isotopic compositions of boron, carbon, and nitrogen at the cosmic ray source differ substantially from those of the solar system, other recent measurements (e.g. Mewaldt *et al.* 1980) have indicated enhancements in the neutron rich isotopes of neon and magnesium. Improvements in statistics, especially at balloon energies, and in parameters of the model, most notably the low energy cross sections, may eventually show that ^{13}C and ^{15}N are similarly enhanced. Emphasis in the future might well be placed on high energy, high resolution, and long duration balloon measurements.

Chapter 5

Summary

We have described a balloon–borne instrument capable of measuring masses of individual cosmic ray nuclei using position–sensitive multiwire proportional counters for measurement of particle trajectory, and CsI scintillators for measurement of particle energy, and have discussed the calibrations of that instrument using both data from an accelerator and the balloon flight itself.

The saturation properties of CsI have been studied in the context of analyzing the data for mass; it is found that the differential scintillation efficiency of CsI decreases, for boron, carbon, and nitrogen nuclei, by $\sim 15\%$ as the specific ionization of a particle increases from ~ 50 to $200\,\mathrm{MeV\,mm^{-1}}$. A maximum likelihood technique has been used to analyze the mass distributions of boron, carbon, and nitrogen. The achieved rms mass resolution varies from $\sim 0.3\,\mathrm{amu}$ at boron to $\sim 0.5\,\mathrm{amu}$ at nitrogen, consistent with a detailed theoretical evaluation of the factors which contribute.

The measurements have been corrected for nuclear interactions which occur in the CsI detector material, as well as for the contamination introduced by the $\sim 5\,\mathrm{g\,cm^{-2}}$ of residual atmosphere. We obtain $^{10}B/B = 0.33^{+0.17}_{-0.11}$, $^{13}C/C = 0.06^{+0.13}_{-0.01}$, and $^{15}N/N = 0.42^{+0.19}_{-0.17}$ (the errors being primarily statistical), at energies of ~ 280, 300, and $330\,\mathrm{MeV\,amu^{-1}}$, respectively. The results are in agreement with other measurements, both at lower ($\sim 100\,\mathrm{MeV\,amu^{-1}}$) and similar energies.

We have described a model of galactic propagation and solar

modulation with which we predict the abundances observed near earth, given a solar-like isotopic composition at the cosmic ray source. We find no evidence for source abundances which differ substantially from those of the solar system.

Appendix A
MWPC Background

We show in Figures A.1a–c the distribution in y position as measured by MWPC Y2 for penetrating events selected according to signal D_7. For fast particles the output of detector D7 is proportional to Z^2 (Equation 2.2) so that the three figures correspond approximately to different charge regions. Although the number of events within each sector agrees with the results of a trajectory simulation, the obviously anomalous tendency for the distributions to peak at sector centers is present to about the same degree in all MWPC's, and it is clear that the peaking becomes more pronounced for higher Z particles.

The use of sectors and delay line readout in our MWPC's [see Wiedenbeck (1978) for a comprehensive description] means that a given counter is unable to infer a two–particle event, and that the counter will respond to such an event by recording i) the sector of the particle with the larger ionization and ii) position within that sector represented by an average of the positions of the two particles within their respective sectors. This suggests that the peaking of the Y2 distribution toward sector centers is associated with two–particle events. In particular, because the feature is more pronounced for higher Z particles, we hypothesize that knock–on electrons produced in either the 0.69 g cm^{-2} aluminum shell which encloses our experiment, or the counter gas itself, are above threshold an appreciable fraction of the time.

Because we have four (three) independent measurements of the y (x) position we can calculate χ_x and χ_y (§2.2.1, Figure 2.3) according to

Figure A.1

Histogram of y position as measured by MWPC Y2 for penetrating events. A crude charge selection has been made based on signal D_7.
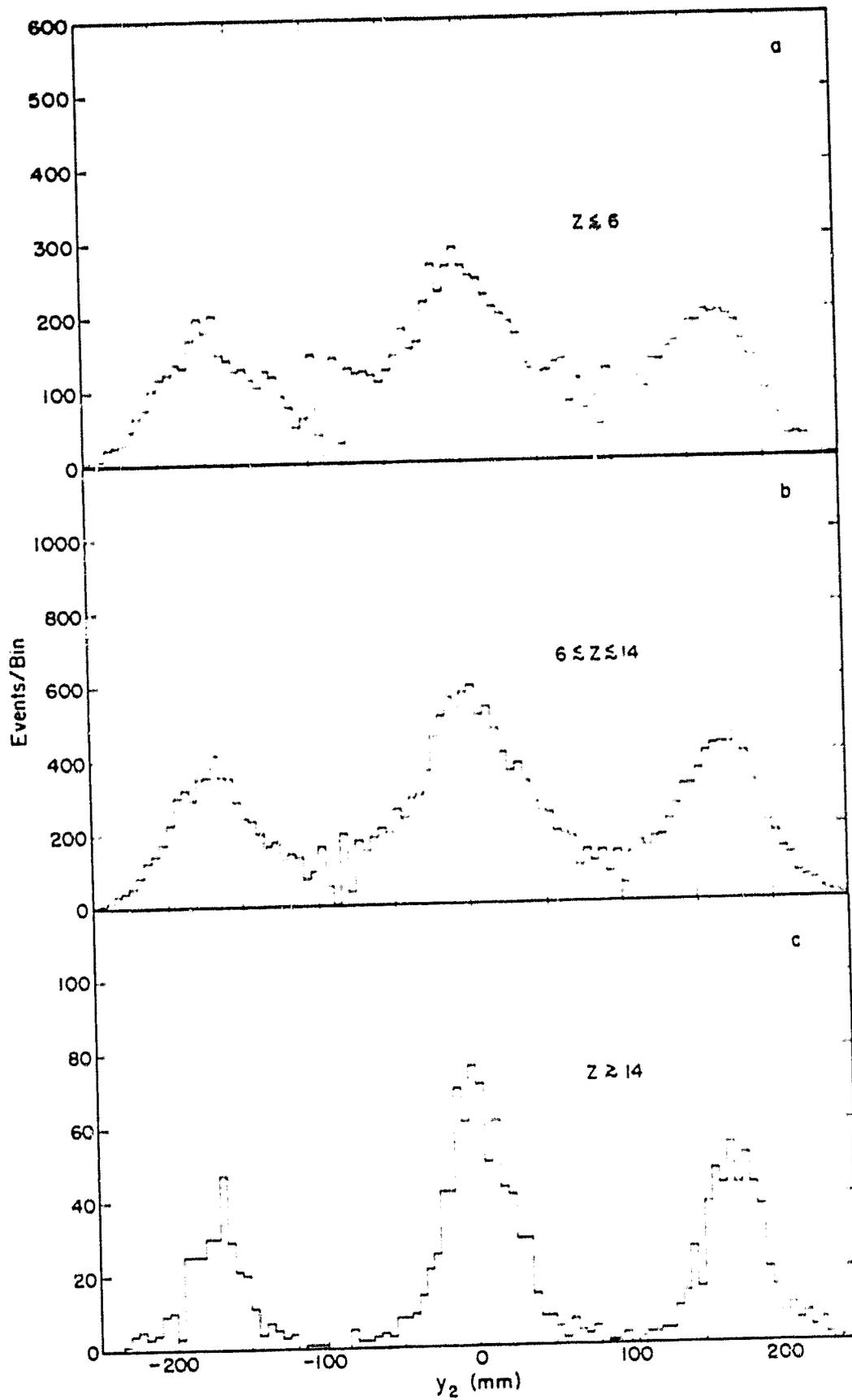
the straight-line fits to the x and y trajectories. Large χ values indicate knock-on electron contamination, small values indicate high quality trajectory determination. Events for which $\chi_y > 3\,mm$ have been re-analyzed under the assumption that one of the four y measurements is significantly worse than the other three and is therefore not used. Because of the relative geometry of X1, X3, and X4 (Figure 2.2c), χ_x is essentially an indication of the extent to which X3 and X4 are consistent, and is not useful in determining whether or not X1 is "bad". We are therefore unable to eliminate events for which X1 is contaminated by knock-ons.

To determine what the degraded X1 resolution of such events might be, we have used the y trajectory data. We show in Figure A.2 a histogram of the quantity $<y_3> - y_3$, that is, the deviation of the measured y_3 from that calculated according to the results of the straight-line fit to the y trajectory (only events for which Y1,2,4 were not contaminated are used in the fit; Y3 is always used). The central peak corresponds to "good" Y3 events, but there is a broad background with FWHM $\approx 100\,mm$, or $\sigma \approx 40$ mm. Similar analyses of $<y_i> - y_i$ for i=1,2,4 indicate that the resolution of a coordinate contaminated by knock-on electrons is $\sigma \approx 20-40\,mm$.

Figure A.2

MWPC background as shown by a histogram of the quantity $<y_3> - y_3$. The vertical scale is logarithmic.
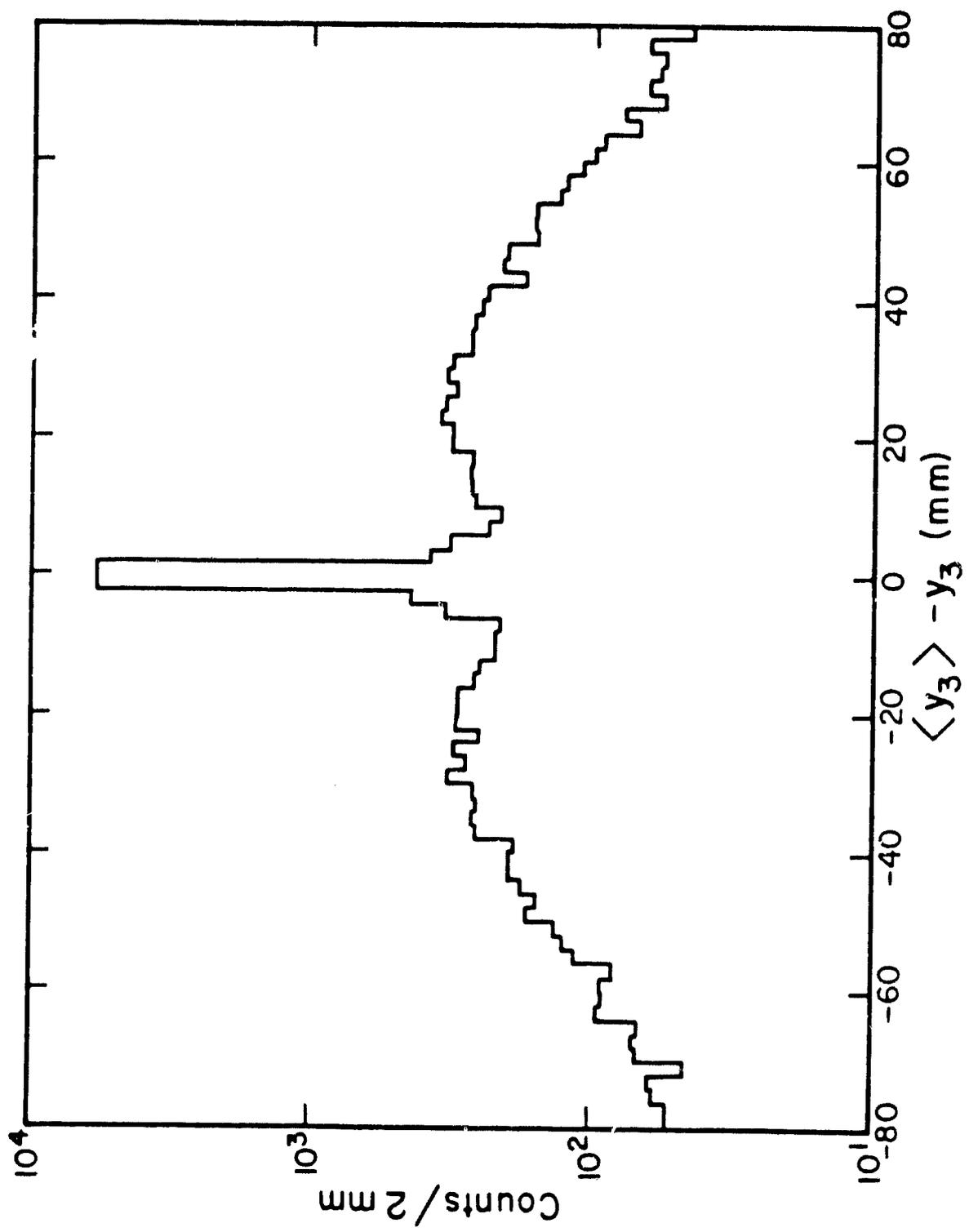
Appendix B

Multiple Coulomb Scattering in Thick Detectors

To derive a form for the mean square multiple Coulomb scattering angle when the detector thickness x is large enough so that the particle velocity changes significantly in traversing it, we begin with Equation 3.6 in differential form:

$$d\sigma_\vartheta^2 = k \frac{Z^2 \, dx}{M^2 (\gamma \beta^2)^2} \, ,$$

where k is independent of velocity. With $dx = \dfrac{dE}{dE/dx}$ and the fact that scatterings in successive layers dx are independent processes so that the variances can be integrated, we have

$$\sigma_\vartheta^2 = \int_{E'}^{E} dE \, \frac{kZ^2}{M^2 \gamma^2 \beta^4 \dfrac{dE}{dx}} \, ,$$

where E is the initial energy and E' the final energy. Since $\dfrac{dE}{dx} (\beta, Z) \approx$ constant $\dfrac{Z^2}{\beta^2}$, the quantity $\dfrac{\beta^2 \dfrac{dE}{dx}}{Z^2}$ is to a good approximation independent of both β and Z, so we treat it as the constant $\beta^2 \dfrac{dE}{dx} (\beta, 1)$. In addition, the particle momentum $p = \gamma \beta M m_p c$ is related to the energy by $(pc)^2 = E^2 + 2 M m_p c^2 E$ (m_p is the proton rest mass). Thus

$$\sigma_\vartheta^2 = \frac{k (m_p c^2)^2}{\beta^2 \dfrac{dE}{dx} (\beta, 1)} \int_{E'}^{E} dE \, (E^2 + 2 M m_p c^2 E)^{-1} \, ,$$

which integrates to

$$\sigma_\vartheta^2 = \frac{k \, m_p c^2}{2 M \beta^2 \dfrac{dE}{dx} (\beta, 1)} \, \ln \left[\frac{2E}{(1+\gamma) E'} + \frac{\gamma - 1}{\gamma + 1} \right] \, ,$$

since $E = (\gamma - 1) M m_p c^2$.

118

Appendix C

Energy Spectra Used in the Atmospheric Correction

Measurements by the Chicago group of the cosmic ray differential energy spectra (Garcia-Munoz *et al.* 1977b) indicate that the relative elemental abundances are, to a good approximation, independent of energy, at least over the energy interval 200–700 MeV amu^{-1}. We have approximated their measurement of the oxygen spectrum by

$$J(\varepsilon) \approx k\left(\frac{\varepsilon}{\varepsilon_0}\right)^a \tag{C.1},$$

where $\varepsilon_0 = 300$ MeV amu^{-1}, and $a = 0.35$ for $\varepsilon < \varepsilon_0$, $a = -0.77$ for $\varepsilon > \varepsilon_0$. Because the level of solar modulation appropriate to their measurements was less than that for the HEIST flight (§4.4.2), we have performed the following calculation which predicts the spectrum for 1978.

The first-order effect of the expanding solar wind on the cosmic rays is to reduce the value of their energy per nucleon outside the solar cavity to that at 1 AU by an amount Φ. If $J_{IS}(\varepsilon)$ is the differential energy flux outside the solar cavity in local interstellar space, then the flux at 1 AU ("force-field" approximation, Fisk 1974) is $J_{1\,AU}(\varepsilon) = s(\Phi,\varepsilon)\, J_{IS}(\varepsilon+\Phi)$,

where $s(\Phi,\varepsilon) = \dfrac{(\varepsilon+M_p)^2 - M_p^2}{(\varepsilon+\Phi+M_p)^2 - M_p^2}$. Here $M_p = 938$ MeV is the proton rest energy. If we assume that the local interstellar flux does not change with time, then we can relate the fluxes at 1 AU, $_1J_{1\,AU}$ and $_2J_{1\,AU}$, characterized by the levels of modulation Φ_1 and Φ_2, respectively, by

$$_1J_{1\,AU}(\varepsilon) = \frac{s(\Phi_1,\varepsilon)}{s(\Phi_2,\varepsilon+\Phi_1-\Phi_2)}\ _2J_{1\,AU}(\varepsilon+\Phi_1-\Phi_2) .$$

With $_2J_{1\,AU}$ equal to the measurement by Chicago given above,

$\Phi_2 \approx 220$ MeV amu^{-1}, and $\Phi_1 \approx 300$ MeV amu^{-1}, we find that $_1J_{1AU}$ can be approximated by a form similar to Equation C.1, except that $\varepsilon_0 = 220$ MeV amu^{-1}, and $a = 0.57$ for $\varepsilon < \varepsilon_0$, $a = -0.46$ for $\varepsilon > \varepsilon_0$. This, then, is the form we use in making the atmospheric correction.

References

Barkas, W. H., and M. J. Berger, NASA SP–3013 (1964).

Bevington, P. R., *Data Reduction and Error Analysis for the Physical Sciences*, (New York: McGraw–Hill), Chap. 10 (1969).

Birks, J. B., *The Theory and Practice of Scintillation Counting*, (New York: MacMillan) (1964).

Bischel, H., in *AIP Handbook*, ed. Gray, (New York: McGraw–Hill), 8–142 (1972).

Buffington, Andrew, Charles D. Orth, and Terry S. Mast, *Ap. J.*, **226**, 355 (1978).

Cameron, A. G. W., *Space Sci. Rev.*, **15**, 121 (1973).

Casse', M., and P. Goret, *Ap. J.*, **221**, 703 (1978).

Coswik, R., Yash Pal, S. N. Tandon, and R. P. Verma, *Phys. Rev.*, **158**, 1238 (1967).

Fisk, L. A., in *High Energy Particles and Quanta in Astrophysics*, eds. McDonald and Fichtel, (Cambridge: MIT Press), Chap. IV (1974).

Garcia–Munoz, M., G. M. Mason, and J. A. Simpson, *Proc. 15th Internat. Cosmic Ray Conf.* (Plovdiv), **1**, 301 (1977a).

Garcia–Munoz, M., G. M. Mason, J. A. Simpson, and J. P. Wefel, *Proc. 15th Internat. Cosmic Ray Conf.* (Plovdiv), **1**, 220 (1977b).

Garcia–Munoz, M., and J. A. Simpson, *Proc. 16th Internat. Cosmic Ray Conf.* (Kyoto), **1**, 270 (1979).

Gleeson, L. J., and W. I. Axford, *Ap. J.*, **154**, 1011 (1968).

Greiner, D. E., M. E. Wiedenbeck, F. S. Bieser, H. J. Crawford, H. H. Heckman, and P. J. Lindstrom, *Proc. 16th Internat. Cosmic Ray Conf.* (Kyoto), **1**, 418 (1979).

Guzig, T. Gregory, PhD. Thesis, University of Chicago (1980).

Hagen, F. A., A. J. Fisher, and J. F. Ormes, *Ap. J.*, **212**, 262 (1977).

Jackson, J. D., *Classical Electrodynamics*, 2nd edition, (New York: Wiley), Chap. 13 (1975).

Janni, J. F., Air Force Weapons Laboratory Technical Report AFWL–TR–65–150 (1966).

Lezniak, J. A., and W. R. Webber, *J. Geophys. Res.*, **76**, 1605 (1971).

Lezniak, J. A., and W. R. Webber, *Ap. J.*, **223**, 676 (1978).

Lindstrom, P. J., D. E. Greiner, H. H. Heckman, B. Cork, and F. S. Bieser, Lawrence Berkeley Laboratory Report LBL–3650 (1975).

Lund, L., I. L. Rasmussen, B. Peters, and N. J. Westergaard, *Proc. 14th Internat. Cosmic Ray Conf.* (Munich), **1**, 257 (1975).

Mathews, J., and R. L. Walker, *Mathematical Methods of Physics*, 2nd edition, (New York: Benjamin), Chap. 14 (1970).

Meneguzzi, M., J. Audouze, and H. Reeves, *Astr. Ap.*, **15**, 337 (1971).

Mewaldt, R. A., J. D. Spalding, E. C. Stone, and R. E. Vogt, *Ap. J. (Letters)*, **235**, L95 (1980).

Ormes, J. F., and P. Freier, *Ap. J.*, **222**, 471 (1978).

Ormes, J. F., personal communication (1981).

Reames, D. V., in *High Energy Particles and Quanta in Astrophysics*, eds. McDonald and Fichtel, (Cambridge: MIT Press), Chap. II (1974).

Rossi, B., *High–Energy Particles*, (Englewood Cliffs: Prentice–Hall), Chap. 2 (1952).

Silberberg, R., and C. H. Tsao, *Ap. J. Supp.*, **25**, 315 (1973a).

Silberberg, R., and C. H. Tsao, *Ap. J. Supp.*, **25**, 335 (1973b).

Silberberg, R., C. H. Tsao, and M. M. Shapiro, in *Spallation Nuclear Reactions and Their Applications*, eds. Shen and Merker, (Dodrecht: Reidel), 49 (1976).

Silberberg, R., and C. H. Tsao, *Ap. J. Supp.*, **35**, 129 (1977a).

Silberberg, R., and C. H. Tsao, *Proc. 15th Internat. Cosmic Ray Conf.* (Plovdiv), **2**, 84 (1977b).

Silberberg, R., and C. H. Tsao, *Proc. 15th Internat. Cosmic Ray Conf.* (Plovdiv), **2**, 89 (1977c).

Stone, E. C., *Proc. 13th Internat. Cosmic Ray Conf.* (Denver), **5**, 3615 (1973).

Truran, J. W., in *CNO Isotopes in Astrophysics*, ed. J. Audouze, (Dodrecht: Reidel), 145 (1977).

Urch, I. H., and L. J. Gleeson, *Ap. Space Sci.*, **20**, 177 (1973).

Wannier, P., *Ann. Rev. Astron. Astrophys.*, **18**, 399 (1980).

Webber, W. R., and J. Kish, *Proc. 16th Internat. Cosmic Ray Conf.* (Kyoto), **1**, 389 (1979).

Webber, W. R., J. Kish, and G. Simpson, *Proc. 16th Internat. Cosmic Ray Conf.* (Kyoto), **1**, 424 (1979).

Wiedenbeck, M. E., PhD. Thesis, California Institute of Technology (1978).

Wiedenbeck, M. E., unpublished notes (1973).

Wiedenbeck, M. E., D. E. Greiner, F. S. Bieser, H. J. Crawford, H. H. Heckman, and P. J. Lindstrom, *Proc. 16th Internat. Cosmic Ray Conf.* (Kyoto), **1**, 412 (1979).

Wiedenbeck, M. E., and D. E. Greiner, *Ap. J. (Letters)*, **239**, L139 (1980).